Politecnico di Milano

School of Industrial and Information Engineering
Master of Science in Materials Engineering
and Nanotechnology

Synthesis of ZnO-based nanostructured materials via Pulsed Laser Ablation in Liquid

Candidate
Francesco Bastianini
ID n. 800414

Supervisor
Prof. Carlo S. Casari
Co-Supervisor
Dr. Anna Facibeni

Academic Year 2014–2015

Acknowledgments

For the opportunity to realize this exciting thesis project I am very grateful to Professor Carlo Casari. I thank him for all the things that he taught me, for his useful ideas in the development of this work and for his helpfulness. I would like to thank Dr Anna Facibeni because she followed me step by step and had passionate of this thesis. A particular acknowledgement goes to Dr Valeria Russo for teaching me how to use and interpret the Raman Spectroscopy.

I would like to state my gratitude to all the fantastic people that I met in Micro and Nanostructured Materials Lab, who have made these months very enjoyable. In particular I thank Matteo Gerosa to make me feel like I was at home, Antonio who was able to fix every technical questions, David with his pleasantness, Francesco and all PhD students for being side-by-side with me and always having a solution for all my very frequent problems.

I also thank the Professors Roberto Piazza and Stefano Buzzaccaro of the Dipartimento di Chimica, Materiali e Ingegneria Chimica Giulia Natta for giving me the support in Dynamic Light Scattering analyses, and the Professor Alessandra Polissi of the Dipartimento di Biotecnologie e Bioscienze, Università degli Studi Milano-Bicocca for the possibility of performing antibacterial analyses.

Contents

Abstract

The ablation of solid targets immersed in liquid via pulsed lasers is a technique which, due to its peculiarity, is becoming even more important to obtain nanostructures in simple, economical and chemically clean approach. This innovative technique is halfway within the top-down and bottom-up methodologies, as well as within the chemical and physical processes of synthesis of nanoparticles. The current field where one thinks that the technique could develop mainly is the ablation of oxides and of semiconductors, and in particular of doped materials, in order to take advantage of its benefits respect to other techniques of synthesis. We have identified this opportunity of development, and we built the required instrumentation to perform the ablation of target of Aluminium doped Zinc Oxide, a very promising material in the field of the photovoltaic cells of new generation. Achieved this first purpose, we made every effort to optimize the physical quantities in the running to obtain a high rate of ablation and very concentrated solutions of nanoparticles in suspension. From these lasts we succeeded in growing films of various thickness; therefore with only one technique was possible obtaining a huge variety of nanostructured materials: nanospheres, nanorods, thin films and other more complex structures which are going to be shown during the dissertation. Furthermore we dealt with a systematic analysis of the main factors which participate in the process of ablation, correlating them with the properties of the synthesised nanostructures, from various points of view: from the dimensions to the morphology, from the composition to the vibrational properties. Finally were taken in account many potential fields of application, and someone of these was also subject of investigation during this thesis project.

Sommario

L'ablazione di target solidi immersi in liquido tramite laser pulsati è una tecnica che, a causa delle sue peculiariatà, si sta sempre più affermando per ottenere nanostrutture in maniera semplice, economica e chimicamente pulita. Questa tecnica innovativa si pone a metà strada tra le metodologie top-down e bottom-up, nonché tra i processi chimici e fisici di sintesi di nanoparticelle. L'attuale ambito in cui si pensa che la tecnica si possa sviluppare maggiormente è l'ablazione di ossidi e di semiconduttori, ed in particolare di materiali drogati, allo scopo di sfruttarne i benefici rispetto ad altre tecniche di sintesi. Noi abbiamo individuato questa opportunità di sviluppo, ed abbiamo costruito la strumentazione necessaria per effettuare l'ablazione di target di ossido di zinco drogato con alluminio, un materiale molto promettente nel campo delle celle fotovoltaiche di nuova generazione. Conseguito questo primo obiettivo, ci siamo impegnati ad ottimizzare le grandezze fisiche in gioco per ottenere un'elevata velocità di ablazione e soluzioni molto concentrate di nanoparticelle in sospensione. Da queste ultime siamo riusciti a far crescere film di vario spessore; pertanto con una sola tecnica è stato possibile ricavare una grande varietà di materiali nanostrutturati: nanosfere, nanobacchette, film sottili ed altre strutture più complesse che saranno mostrate nel corso della trattazione. Inoltre ci siamo spinti in una sistematica analisi dei principali fattori che intervengono nel processo di ablazione, correlandoli con le proprietà delle nanostrutture sintetizzate, sotto vari punti di vista: dalle dimensioni alla morfologia, dalla composizione alle proprietà vibrazionali. Infine sono stati presi in considerazione molti potenziali campi di applicazione ed alcuni di questi sono stati anche oggetto di studio durante questo progetto di tesi.

Introduction

Zinc Oxide is a II-VI group semiconductor with a wide direct bandgap; it is a multifunctional material for a variety of practical applications due to its excellent physical and chemical properties. Notably, ZnO low dimensional nanomaterials have attracted great interests because of their unique and fascinating optical, electrical, mechanical and piezoelectric properties, together with their wide use in fundamental scientific research and potential technical applications.

Doping ZnO provides a combination of low resistivity and high transparency, that makes it suitable for applications as Transparent Conductive Oxide (TCO), in substitution of other expensive and high environmental impacting oxides used nowadays. The two more promising doped Zinc Oxide materials which have been developed, are the Gallium-doped ZnO (GZO) and the Aluminium-doped ZnO (AZO).

Up to now, many methods, such as Chemical Vapour Deposition (CVD), chemical solution route, sputtering, Molecular Beam Epitaxy (MBE) and Pulsed Laser Deposition (PLD) have been proved to synthesize ZnO nanostructures. However each technique shows evident drawbacks: high temperature for CVD, by-products contamination in chemical techniques, expensive instrumentations to reach high vacuum level in MBE and PLD, *etc*..

Pulsed Laser Ablation of target in Liquid media (PLAL) has the potentialities for overcoming these limitations. It is a recently developed technique for synthesis of nanoparticles in suspension, and is becoming a popular and emerging area of research, due to its simplicity, cheapness and environmentally friendship. Practically every material can be ablated via

this technique, and also the liquid media where the target is immersed, can be largely varied. These are only two of many involved ablation quantities; varying them, a control of size, shape and properties of nanoparticles is feasible.

Even if the ablations are performed at ambient temperatures and pressures, in the contact point of the laser pulse with the target a plasma plume is formed at extremely high temperature and pressure. So they make possible the formation of nanostructures and phases that are not observable in standard conditions. This can explain the enormously rich variety of nanostructures obtainable with PLAL technique.

In this thesis project, we set ourselves the goal of applying PLAL technique to synthesize nanostructured AZO. In particular, we want to put in evidence the correlation of main physical quantities of ablation with the production rate and the properties of produced nanoparticles.

First of all, we have to build the experimental instrument for ablation in liquid. The realization will take in account the peculiarity of PLAL. Then we will proceed to effective ablation of AZO target in the liquid, that we choose to be distilled water. In this way a suspension of nanoparticles in water should be obtained.

We select the analyses to be performed in order to have a complete knowledge of our products. So we will estimate the concentration of nanoparticles in solution by the difference of masses of target before and after ablation. Then measurements of dimensions will be performed directly in liquid via the Dynamic Light Scattering method (DLS) and on deposited nanostructures via Atomic Force Microscope (AFM) and Scanning Electron Microscope (SEM). SEM analyses will be useful also to visualize the aggregation of structures in deposited films. In addition we will make the Raman Spectroscopy characterisation and Energy Dispersive X-ray analysis (EDX) of these films, with the purpose of discovering which species are effectively produced and obtaining information about their crystal structure. We will monitor also the stability of nanoparticles in suspension.

We identify a possible application of Zinc Oxide nanoparticles as antibacterial agent on textile materials; we will test them in order to verify if the PLAL is an advantageous technique to this purpose. Finally, other experiments will investigate another oxide, very important for its applica-

tion: the Titanium Dioxide TiO_2. In this way we can compare the different characteristics of the two oxides after ablation.

The dissertation of the thesis is organized in four chapters. Chapter 1 consists in an overview on materials, the Zinc Oxide and the Aluminium-doped Zinc Oxide. Here we will see the properties that make these materials so interesting, the possible techniques to synthesize various kinds of nanostructures, with main advantages and disadvantages for each method, and the fields of application which should more benefit from our synthesized nanostructures. Chapter 2 presents the technique of Pulsed Laser Ablation in Liquid, with a discussion of the up-to-now understood mechanism of ablation; in the same chapter also the influences of parameters on processes and a presentation of obtainable products are reported.

In the following chapter 3 we will describe carefully the realization of experimental apparatus, then we will explain the procedure and the criteria of choice of parameters, concluding with the description of techniques of analysis. All results will be reported in chapter 4. They are grouped to information type: morphology, composition and structure. Every correlation between physical quantities will be discussed and justified.

Chapter 1

Zinc Oxide based Materials

1.1 Main properties of Zinc Oxide

1.1.1 Crystal structure

The two most common structures for the group II-VI binary compound semiconductors are cubic Zinc-Blende and hexagonal wurtzite [1]. At ambient temperature and pressure, the thermodynamically stable phase for Zinc Oxide is hexagonal wurtzite. However in specific condition, Zinc Oxide can exhibit the other typical structure of II-VI compounds, the Zinc-Blende, and moreover other two structures: the Rocksalt and the cubic Caesium-Chloride. The basic characteristic involved in the stability of the structures are the pressure (both that of growth and actual one) and the interaction with close structures.

The Wurtzite structure takes its name from another zinc compound, the Zinc Sulphide. It derived from an expanded *hcp* anion (oxygen in this case) array in which the cations (zinc) occupy half of the tetrahedral holes [2]. So each atom is surrounded by four atoms of the other species in $(4,4)$ - coordination, like in the sp^3 covalent structures. Actually the ionicity of Zinc Oxide is considered borderline between covalent and ionic semiconductor: its bond has 62 % of ionic nature [3].

If the wurtzite structure is the stable phase at ambient pressure, the Rocksalt is stable at high pressure; the threshold is not certain, depending on technique involved in the growth of crystal. This structure is favoured

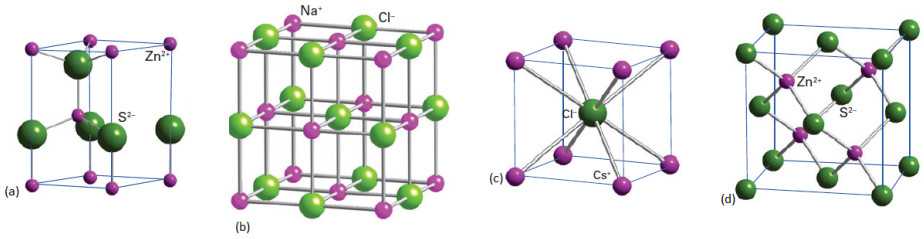

Figure 1.1: The structures which ZnO can show [2] (a) Wurtzite; (b) Rocksalt; (c) Caesium-Chloride (d) Zinc-Blende.

because at high pressure the interionic Coulomb interaction prevails over the covalent nature and the lattice rearranges in a more compact way. The coordination is $(6,6)$ and it is based on a *ccp* array of anions with cations in all octahedral holes. This transition happens at different pressures depending on technique and conditions, for example never in epitaxial growth, for other techniques in a range from $8,7$ GPa to 10 GPa but sometimes a complete transformation requires 15 GPa. During de-pressurization hysteresis is reported at $1.9 - 2.0$ GPa, or even a maintenance of rocksalt structure at room pressure.

Theoretical calculations agree with pressure of transition from wurtzite to rocksalt; moreover they predict an additional transition from rocksalt to even more compact cubic Caesium-Chloride structure. This consists in a cubic unit cell where each corner is occupied by an anion and each cubic hole is occupied by a cation. The coordination is $(8,8)$. The phases transition was predicted to happen between 256 GPa and 352 GPa, but they are still awaiting experimental observations.

Lastly, the Zinc-Blende is another reported structure of ZnO: it is a *ccp* anion arrangement where cations occupy half of tetrahedral holes, in $(4,4)$-coordination. It is metastable and can be stabilized only by heteroepitaxial growth on cubic structures. Moreover it could be possible stabilizing other crystal lattices over substrates with different structures.

1.1.2 Electronic and electrical properties

ZnO is an n-type semiconductor with a wide direct band gap of $Eg = 3,37\ eV$ at 300 K, and high exciton binding energy (60 meV) [4]. The width of the band gap is confirmed by several experimental measurements of band structure, for example Angle Resolved UV Photoelectron Spectroscopy (ARUPS) [5]. Core bands of ZnO come from $O2s$ orbital and $Zn3d$ orbitals, at $-10\ eV$ and $-9\ eV$ respectively. Upper filled bands range from $-5\ eV$ to $0\ eV$, mainly formed by $O2p$ levels. The first set of unfilled conduction band corresponds to $Zn4s$ orbital.

On the other hand, theoretical calculations for band structure failed to predict the actual band gap, until Local Density Approximation (LDA) implemented with Self-Interaction Corrections [6], a method very useful in bonds involving $3d$ electrons. Effectively, pure LDA method predicts a band gap of only $0,23\ eV$, meanwhile for LDA-SIC it is $3,77\ eV$, much closer to real one ($3,34\ eV$ in the same conditions). We can see the plots of band structures in Figure 1.2, that is valid for wurtzite crystal; similar calculations can be conducted for other structures displayable by ZnO [7].

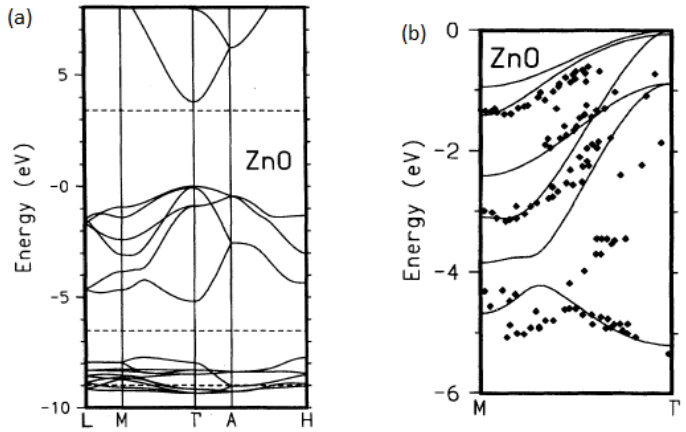

Figure 1.2: The band structure of ZnO along the path $LM\Gamma AH$ [6] (a), and the comparison with experimental band structure along the path $M\Gamma$ [5] (b).

The same paper reports the total Density Of States DOS, calculated with LDA. In Figure 1.3 the evolution with pressure is shown. When wurtzite

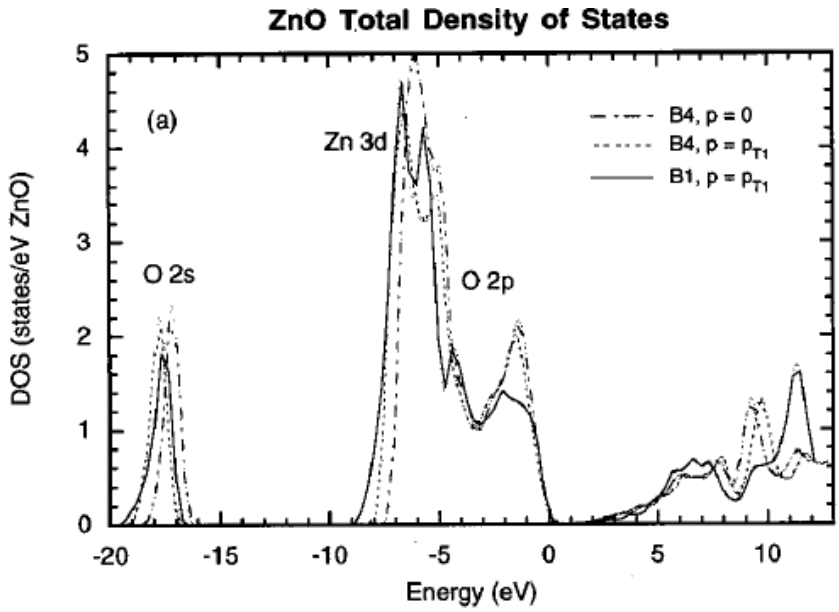

Figure 1.3: The calculated density of states for ZnO in wurtzite phase (B4) in vacuum and at transition pressure p_{T1}, and in rocksalt structure (B1) just above that pressure [7].

phase remains, minimal changes occur, i.e. the lowering of the upper valence band and its shift down in energy, or a splitting in $Zn3d$ states. More significant changes happen in rocksalt transition: net reduction of upper valence band peak and shrinkage of $Zn3d$ peak.

Applications in electronic and opto-electronic fields are becoming more and more important for ZnO due to its direct absorption and its large band gap. The advantages involved by latter feature are high breakdown voltages, ability to sustain large electric fields, lower noise generation and high-temperature and high-power operations. The major scattering mechanisms that generally govern the electron transport in III-V semiconductor are also valid for ZnO. They are:

- Defects or intentionally doped impurities which act as centres of altering potential and can affect motion of free carriers.
- The lattice vibrations which induce an electric field interacting with moving charges, through the polar LO-phonon scattering mechanism.

- Acoustic phonon scattering due to strain associated with acoustic phonons.
- Due to piezoelectricity (Subsection 1.1.4), there is a scattering due to electric field generated by possible strain.
- Two more sources of scattering are dislocations and grain boundaries. Dislocations act as acceptor centres for electrons, charging negatively themselves and reducing the mobility of near electrons.

In pure Zinc Oxide, the carrier concentration reaches $5,05 \cdot 10^{17}\ cm^{-3}$ and the electron mobility up to 440 $cm^2V^{-1}s^{-1}$. The reason for such high values for an un-doped large band gap semiconductor is its natural behaviour as n-type material, but the origin is controversial. Someone affirms that some defects are spontaneously generated, the most important are Zn-on-O antisite, Zn interstitial and O vacancy; for example oxygen vacancy can be formed by partial reduction of oxygen in lattice, originating in this way a couple of free electrons and an energy level near conduction band. Instead, Van de Walle found the nature of this conductivity in unintentional substitutional hydrogen impurities present in ZnO [8]. This hypothesis is supported by the fact that hydrogen is always present in all growth methods and can easily diffuse into ZnO in large amounts due to its enormous mobility.

1.1.3 Vibrational properties

As mentioned in Subsection 1.1.1, Zinc Oxide has hexagonal wurtzitic structure at ambient temperature and pressure, with 4 atoms in unit cell. So there are 12 phonon branches, 9 optical and 3 acoustic, classified according to the irreducible representation reported in Equation 1.1 [9].

$$\Gamma = 2A_1 + 2B_1 + 2E_1 + 2E_2 \tag{1.1}$$

Where:

- A_1 modes have one-fold degeneracy; one of these is acoustic and the other is optical, which is both Raman and IR active.
- B_1 modes have one-fold degeneracy, both optical but silent modes.

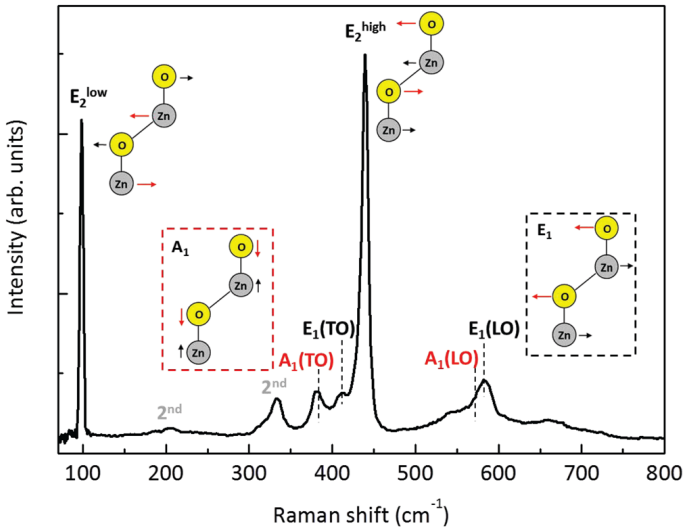

Figure 1.4: Raman spectrum of bulk ZnO with $\lambda = 532\ nm$. The red arrows specify the dominant ions displacements [9].

- E_1 modes have two-fold degeneracy: two are acoustic and other two are optical (Raman and IR active).
- E_2 modes have two-fold degeneracy, all Raman active only.

Focusing on Raman vibrational modes, we can conclude that there are 4 Raman active phonons. The peaks and the visual vibrations are highlighted in Figure 1.4. More than four peaks are detected, someone due to second order, other two due to splitting of A_1 and E_1. These two modes are associated with oxygen motion in a polar way, generating therefore a macroscopic electric field and two possible oscillations: longitudinal-optical (LO) and transversal-optical (TO).

Some modifications can occur in vibrational spectrum when ZnO is subjected to hydrostatic pressure, or when it is doped or when it is grown in thin film. In this last case, small differences appear mainly linked to LO band: it broadens, red-shifts and becomes relatively more intense, with a strong dependence on treatment condition. The behaviour and its motivation are now subjects of study.

From the characteristics of Raman spectra, much information about structure and real stoichiometry of ZnO can be deduced [9]:

- E_2^{low}, associated by the vibrations of heavy Zn sub-lattice, gives in-

formation about the local order in that sub-lattice: deviations from nominal frequency or widening of peak implicate a lower degree of local order. Instead a frequency much less than nominal one may mean residual stresses present in structure.

- E_2^{high}, generated by vibrations of oxygen sub-lattice, has the same tendencies of previous one in terms of residual stresses and of local order degree, in this case for oxygen sub-lattice.

- From the LO band ($A_1(LO)$ and $E_1(LO)$), in particular from its ratio in intensity with E_2^{high}, hints about oxygen stoichiometry and effects of doping could be achieved.

1.1.4 Other properties

ZnO is generally known for its optical transparency, very high in visible range up to UV radiation. Many mechanisms are involved in absorption and photoluminescence spectra [1]; free exciton and bound exciton are the most relevant ones. The wurtzitic *ZnO* conduction band is mainly derived from the *s*-like state, whereas its valence band from *p*-like state, which is split into three bands due to the influence of crystal-field and spin-orbit interactions. Free-exciton transition occurs from the conduction band to these three valence bands (or vice versa), and characteristic *ZnO* near-band-gap intrinsic absorption and emission spectrum are the direct consequence of that. Bound excitons are extrinsic transitions and are related to dopants or defects, which usually create discrete electronic states in the band gap, and therefore influence both optical absorption and emission processes. Effectively, as [10] reports for nanoparticulate *ZnO*, there is a bimodal photoluminescence spectrum, consisting of an excitonic ultraviolet emission peak and a visible peak due to an electron promotion-decay between conduction band, valence band and a state originating from surface defects.

The occupied and empty states of *ZnO* are in an ideal position to form bonds with some gaseous oxides, as Nitrogen Dioxide NO_2 (stronger bond) and Sulphur Dioxide SO_2 (weaker bond) [11]. This quality can be useful for applications, as we will see in Section 1.6, because *ZnO* acts as catalyst

during reduction of these molecules by alkanes. The reaction for adsorption in the case of NO_2 is [12]:

$$1/2\ O_2 + 2\ NO_{2,gas} + ZnO_{solid} \rightarrow Zn(NO_3)_{2,solid} \tag{1.2}$$

leading to formation of a chemical bond with surface. The reaction is promoted by O_{defect} naturally present in ZnO or created by NO_2 itself. This reaction is complete for $T > 250\ K$ and is valid up to 700 K, when NO_3^- decomposition happens and pure ZnO is left. The presence of adsorbed NO_2 and SO_2 can be revealed by X-ray Photoelectron Spectroscopy, by Thermo-Gravimetric Analysis and by Raman Spectroscopy. The Raman spectra for NO_2 and SO_2 is reported in Figure 1.5: in the case of NO_2 one can see the appearance of a new very strong peak around 1055 cm^{-1} and other smaller ones [10]. The main peak is attributed to *O-N-O* symmetric stretch.

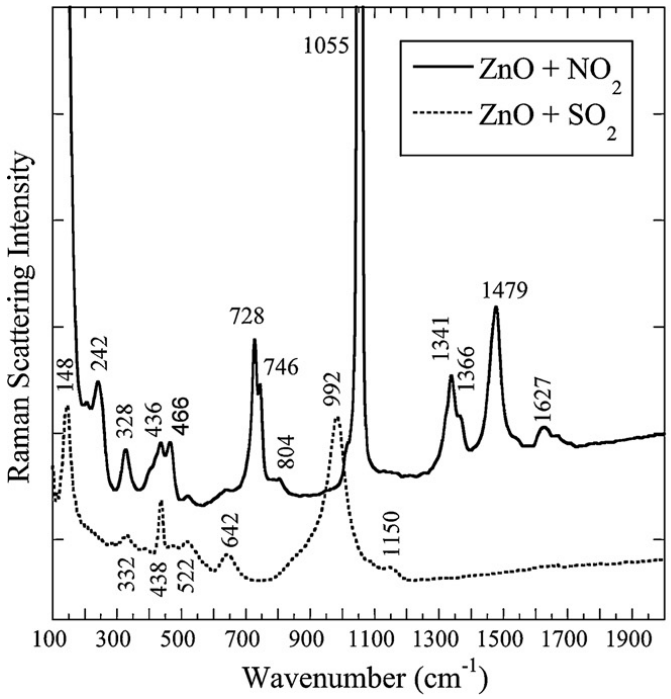

Figure 1.5: Raman spectra of hydrated ZnO nanospheres exposed to NO_2 or SO_2; the wavelength is 532 nm [10].

Zinc Oxide is also famous for exhibition of strong antibacterial activity in small amount, also in absence of light. This property is particularly highlighted in the form of nanoparticles. There is a general agreement with the motivation: the generation of hydrogen peroxide H_2O_2 from the surface of ZnO [13], which is harmful to the cells of living organisms and to bacteria [14].

Finally, another property of Zinc Oxide, very important for applications, is piezoelectricity [1]. In effect wurtzitic structure, a crystalline lattice without inversion symmetry, guarantees one of the highest piezoelectricity tensor in all semiconductors.

1.2 The huge variety of ZnO nanostructures

ZnO has probably the richest variety of different nanostructures [15]. Its range includes highly ordered nanowire arrays, nanorods, nanobelts, nanopencils, nanosprings, nanocombs, nanoboxes, nanorings, and so on. Many types of classification exist; for example a classification based on dimensionality [16]. In its simplest form, nanostructures are categorized into four basic classes, 0D (i.e., nanoclusters and nanoparticles), 1D (i.e., nanotubes and nanowires), 2D (i.e., nanoplates and layers), and 3D (i.e., nanotetrapods). When they are deposited on substrate, the methodology of deposition has a profound impact on morphology and can be engineered to assemble or fabricate novel structures. However, here we can only describe a small selection of these nanostructures, and we will focus on newest.

Nanopencils are hexagonal elongate structures, with extremities tighten in a small nanowire. The morphology indicates well-hexagonal faceted nanopencils with uniform sizes of 200 nm of diameter and pen tips on the top in a range of $20 - 30$ nm in diameter. A simple two-step catalyst-free method at high temperature was used for producing this nanopencils; the reactants were zinc powders and oxygen. These ZnO nanopencils could be interesting for the applications in field of emission microelectronic devices.

Nanowires were grown on nanorods, via a simple two-step vapour-reflected thermal evaporation process without catalyst at high temperature and pressure. The nanowires appear as an hexagonal arrays grown on top of hexagonal faceted nanorods along the (0001) direction. Nanorods have an average diameter of 400 nm, whereas the nanowires of $15 - 25$ nm.

The nanowire-type nanostructures are candidates as nanoconductors of electrons in nano-optoelectronic devices.

Conic nanotubes are single-crystals synthesized without catalyst in a thermal CVD furnace, where reaction of zinc powders and oxygen happens on Si substrate. The conic nanotubes exhibit straight and tapered morphologies with sharp open-ended tips. The diameter of the open tips is in the range $30 - 100\ nm$, whereas the length of the nanotubes is around $0,5\ \mu m$. Nanotubes were formed by self-assembly of numerous six-radiated branches of hexagram nanosheets.

Nanosheets integrated with nanowalls are an heterostructure with sixfold symmetric nanostructures and were synthesized by a strain-assisted self-catalyzed process at high temperature. The nanostructures are well isolated and separated. The nanostructure is composed of epitaxial nanowalls (thickness $20 - 30\ nm$) in the core with overhangs (width around $100\ nm$) radiated horizontally from the edges of the core and composed of multiple stacked single-crystalline nanosheets. In addition to the sixfold units, elongated twofold symmetric units and rare fourfold symmetric units were also present. The integrated nanostructure may be applied to develop self inclusive nanoelectronics.

To summarize, morphology is highly dependent on three parameters: source material composition, growth temperatures, and diffusion rates. Moreover in some techniques, the competition of the capture of impinged molecules by different surface planes under certain supersaturation determines the nanostructures dimensionality and the morphology.

The reduction of dimensions of materials to nanometric scale has enormous consequences in their properties. Modifications can happen to energy gap, optical properties, vibrational properties and so on. Changes in Raman spectrum happen for example in ZnO nanocrystallites embedded in a gold oxide matrix [17]. There thin films containing nanocrystallites were obtained by magnetron sputtering in pure O_2 using Zn and Au targets, with different contents of Au from 0 % to 71 %. As we can see in Figure 1.6, typical peaks of ZnO were observed (E_2 line at 437 cm^{-1}, $A_1(LO)$ and $E_1(LO)$ lines from 540 to 670 cm^{-1}). In addition to these, there is also a multi-phonon band in range $1050 - 1150\ cm^{-1}$. This last band is observed also in absence of Au, so it derives by ZnO nanocrystallites.

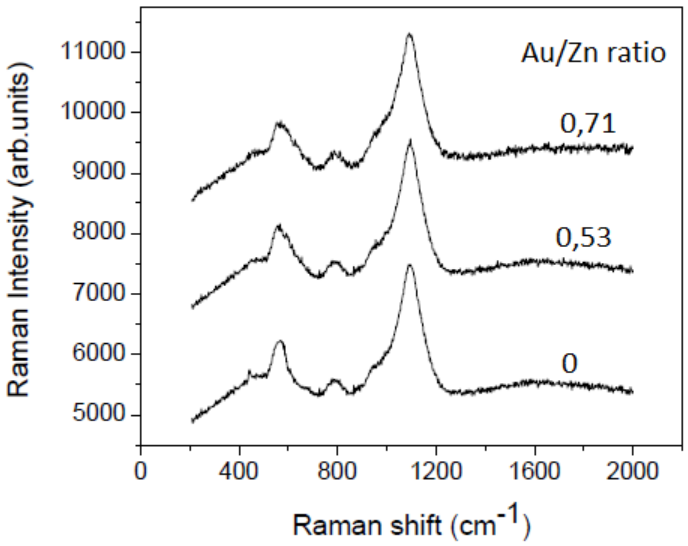

Figure 1.6: Raman spectra of ZnO nanocrystallites embedded in a gold oxide matrix, with excitation wavelength of 488 nm obtained at different Au/Zn ratio [17].

1.3 Present techniques to synthesize nanostructures

Chemical Vapour Deposition (CVD) technique consists of a chamber where a vapour gas precursor containing the required species enters and a chemical reaction happens (pyrolysis, photolysis, oxidation, reduction, doping...), typically at high temperature, more than 500^oC. CVD is a large scale technique, because the only limitation is the chamber dimension. An implementation of this technique is Molecular Organic CVD, where the precursor is a metal bonded to an organic molecule. The advantages are a higher working temperature and so a faster process; the main disadvantage is the toxicity to humans of the greatest part of organometallic compounds. Via this technique can be synthesized both 1D- and 2D- ZnO nanostructures. Thin film grows spontaneously and quite homogeneously on all the parts of substrate exposed to vapour gas; for 1D nanostructures additional expedients should be made, as Vapour-Liquid-Solid [18], where a liquid catalyst, as gold nanodroplets at high temperature, is exposed to vapour precursor phase. The catalyst droplet captures the precursor and, when the system is saturated, the growth of solid desired species starts below the liquid droplet. In this way nanowires can be achieved, but varying oxygen contents some branches can be inducted, leading to dendritic side branched,

comb-like or sheet nanostructures. In other conditions, many structures can be performed, such as nanorods, nanoneedles, nanotetrapods, nanohelices, nanobelts and nanorings.

Chemical methodology includes a lot of techniques able to synthesize many nanostructures. We can mention for the case of ZnO, an aqueous solution method to grow highly oriented nanowires and other nanostructures as nanorods. Huge variety of Zinc-based precursors and solutions can be used, with the great advantage of working at low temperature. A very used solution is composed by $Zn(NO_3)_2$ and hexamethylenetetramine (HMT): hydroxide ions are formed by decomposition of HMT and they react with Zn^{2+} to form ZnO.

Nanocolumnar ZnO crystal or ZnO thin film can be performed by Electrodeposition. The outcome depends on conditions such as density, deposition time and bath temperature. This technique is interesting for simple doping and for bandgap energy control.

Sputtering is a process whereby atoms are ejected from a solid target material due to bombardment of the target with energetic particles. In Magnetron Sputtering the particles are accelerated by magnetic field, so there is a better control of particles path. Advantages are low cost, simplicity and low operating temperature. It is possible growing also epitaxial thin films.

Molecular Beam Epitaxy (MBE) is another method useful for thin film growth. It consists in an array of effusion cells, one for each element or dopant that we want to deposit, in a high vacuum chamber. So great control of composition, monitored in real time with Reflection High Energy Electron Diffraction, and epitaxial growth can be achieved, but high cost apparatus and long time are the main limits to this method. For ZnO, source materials are Zn and O_2.

In Pulsed Laser Deposition (PLD) technique a laser beam is focused on a target, where such high energy density causes ablation (instantaneous vaporization) of material and generation of a plume which expands to

an apposite substrate, where thin film grows. Many parameters can be tuned, as the target-substrate distance, the environment of the chamber, the energy of the laser, its repetition rate and so on. PLD is very suitable for high melting materials, as ceramics or oxides, but has the disadvantages of small deposition areas and of the formation of droplets which cause inhomogeneity. In ZnO case, usual lasers are UV excimer (KrF, $\lambda = 248\ nm$, and ArF, $\lambda = 193\ nm$) and Nd:YAG (typical harmonic of $\lambda = 355\ nm$); the ZnO targets are preferred to Zn metallic. Doping is performed modifying the composition of target.

Pulsed Laser Ablation in Liquid (PLAL), as known as Laser Ablation Synthesis in Solution (LASiS) is a new technique to obtain nanostructured materials; it may be considered as having some aspects both of PLD technique and of chemical methods, and it will be discussed in Chapter 2.

1.4 Doping of ZnO: the case of Aluminium-doped Zinc Oxide

In order to obtain the maximum potential by ZnO, in many applications both high quality n- and p-type doping are required. However, as in many other II-VI semiconductors such as ZnS or $ZnSe$, but also in GaN, n-type doping is simple, instead p-type encountered difficulties up to date.

As explained in Subsection 1.1.2, undoped ZnO has a natural n-type behaviour: electron density is about $10^{17}\ cm^{-3}$ [1]. Elements used for n-type doping can belong to III group (Al, Ga, In) or to VII group (Cl, I). III group dopants substitute Zn in lattice, so they add an electron and the number of charge carriers increases. On the other hand, VII group elements substitute O, adding an electron too. In particular, great success was achieved with Al, Ga and In in terms of high quality doping and high conductivity (minimum resistivity was $1,2 \cdot 10^{-4}\ \Omega cm$ via CVD).

Many attempts of p-doping were performed with I group elements (Li, Na, K) in Zn sites, with noble metal (Cu, Ag) and trying inducing Zn-vacancy, but the results in terms of conductivity were not satisfactory. The most probable factors of this p-doping difficulty are:

- The compensation of dopant elements by low-energy native defects, such as oxygen vacancy or interstitial zinc.
- Low solubility of dopant elements in ZnO.
- Deep impurity level which could oppose to the formation of shallow acceptor level.
- Due to their small atomic size, I group elements tend to occupy interstitial positions rather than Zn sites, acting as donors.

Nowadays, most promising dopants are V group elements in O positions: N, P and As. In particular for N doping some solutions were suggested to improve its solubility: ion implantation or codoping with III group elements (Al, Ga, In).

1.5 Aluminium-doped Zinc Oxide: modifications of properties

As stated, Al doping is very beneficial for some properties of ZnO, however the right concentration of Al is not a trivial question and depends on applications. The main limits concern degradation of electrical and optical properties, as we will see in this section. Currently, 2 % (w/w) of Al_2O_3 is considered the best balance between advantages and disadvantages [19], [20].

1.5.1 Crystal structure

From XRD measurements, it is believed that AZO has the same hexagonal wurtzitic structure of ZnO at ambient temperature and pressure [21], where also very good epitaxial growth was obtained for AZO on ZnO substrate. In effect no other phase corresponding to Al_2O_3 or to other Al compounds were detected in the XRD patterns. So a reasonable hypothesis is that Al^{3+} is incorporated in ZnO lattice, in Zn^{2+} positions. However some differences about lattice parameters, noticed via XRD analyses, may suggest occupation of interstitial positions for Al^{3+}, at least in some conditions of growth [22].

1.5.2 Electronic and electrical properties

Al^{3+} substitutional doping in Zn^{2+} sites has double effect: addition of electrons due to 3+ charge in place of 2+ and increase of already present oxygen vacancy due to charge balance with anions. So a new filled electronic band is created $30 - 50$ meV below the conduction band, where electrons can be easily promoted to. They act as a free electron gas, in good agreement with Drude model theory. A similar situation is shown in Figure 1.7, where In_2O_3 is the base material and Tin is the doping element. Coming back to AZO, electron density is enhanced from 10^{17} cm^{-3} to 10^{21} cm^{-3}; resistivity is turned down to 10^{-4} Ωcm. We have to be careful about excessive doping: when it is too high, scattering negatively influences the mobility and so the conductivity (Figure 1.8).

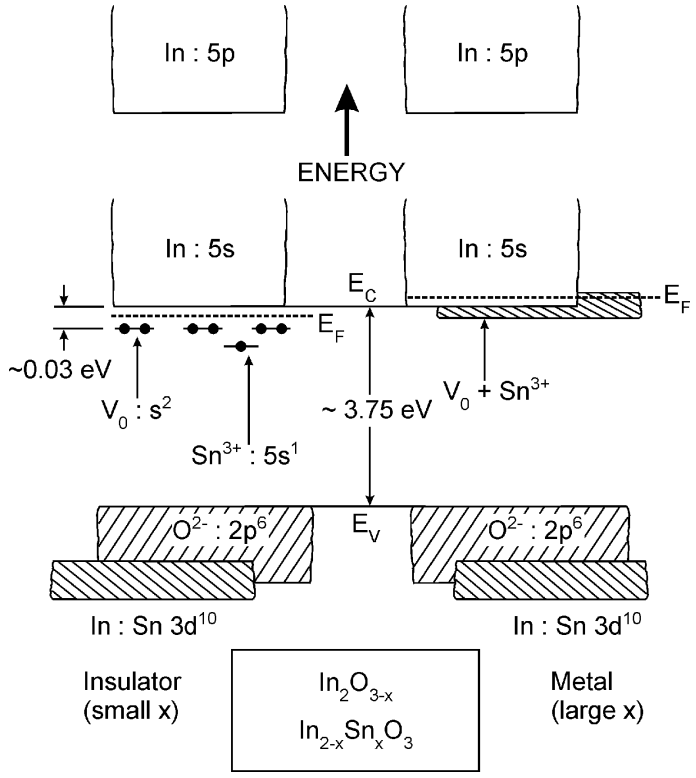

Figure 1.7: Schematic energy band model for Tin-doped In_2O_3 for small x (Sn contents) and large x [23].

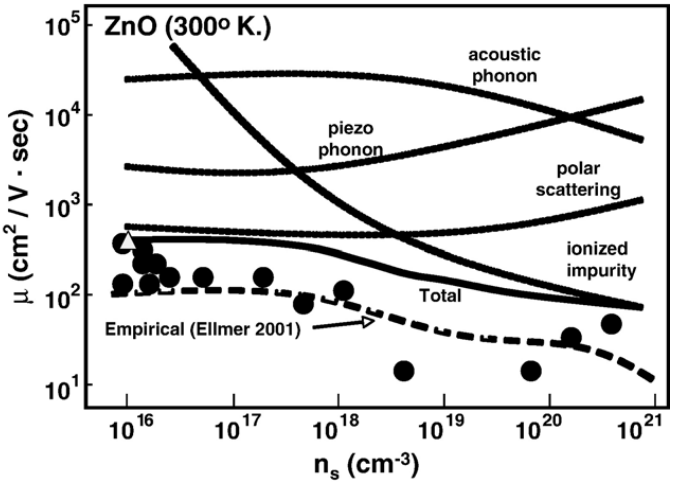

Figure 1.8: Dependence of mobility from main scattering mechanisms in function of electron density; points and dot line are experimental data and fitting, continuous lines come from calculation [24].

1.5.3 Vibrational properties

Some modifications in Raman spectrum occur doping ZnO [9]. As typical in doped ZnO, new peaks appear; the main ones are at 275 cm^{-1} and at 510 cm^{-1}. Their origin is open to argument: someone suggests that they are B_1 silent modes activated by doping-induced breakdown of translational crystal symmetry or by modification of electric field at grain boundary; others support the origin from completely new doping or defect vibrations. On the other hand, their sharpness could also suggest a molecular origin [9]. Additionally, some modifications in peaks and bands are detectable; typically LO band becomes broader and more intense, and other considerations can be formulated starting from observations in Subsection 1.1.3, with addition of Al doping element to explain variations in local order, stoichiometry and defects.

1.5.4 Other properties

New electrons and new levels make possible the absorption of photons at low energy, due to proximity of new levels to conduction band. The result is a limitation of transparency window at low energy: an absorption peak appears in infrared region. However in visible range a wide transparency is maintained, usually greater than 90 %, whereas in UV region absorption

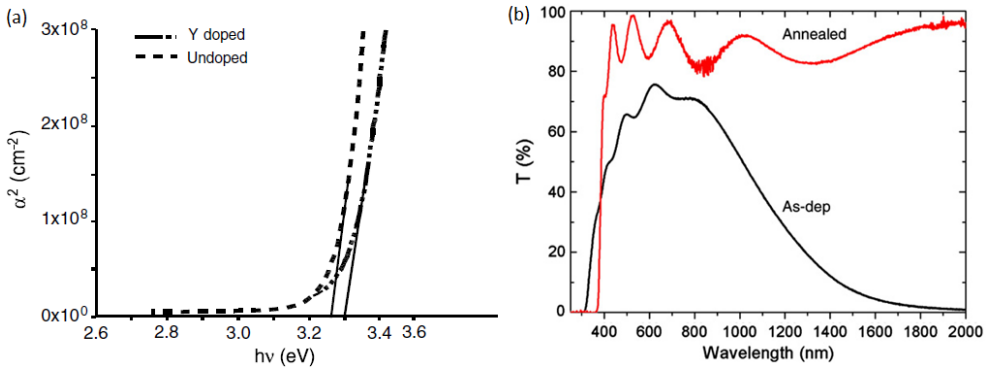

Figure 1.9: Two spectra of doped ZnO: (a) Tauc plot (square of optical absorption vs photon energy) highlights the shift of energy gap due to doping of ZnO thin film with Yttrium, as predicted by Moss-Burstein law [25]; (b) Transparency spectrum of AZO thin film as deposited with PLD and after annealing treatment [22].

is still dominant phenomenon for $E_{phot} > E_{gap}$. However, energy gap is modified by new charge carriers introduced by doping for Moss-Burstein effect:

$$\Delta E_{gap} = \frac{\hbar^2}{2m^*}(3\pi^2 n)^{2/3} \tag{1.3}$$

In Figure 1.9 we can see this phenomenon. For 2 % (w/w) of Al_2O_3 the shift is 500 meV. The risk of an excessive doping is the reduction of the visible transparency window, due to appearance of new defect levels in the middle of band gap and to coupling of conduction band and doping band, which practically cause the conversion of semiconductor behaviour into metallic behaviour.

1.6 Applications of ZnO and AZO

ZnO and its doped compounds have an enormous range of actual and possible applications. Further advantages, which encourage even more the choice of ZnO, are the abundance of zinc in nature, its low cost, the chemical stability and the non-toxicity. Because of its optical, electrical and catalytic properties, potential applications in the fields of solar cells, UV-blue emitter for lasers and diodes, biological sector and gas sensors become obvious.

ZnO is a powerful and good promising material in electronic applications. It can be used both as Transparent Conducting Oxide (TCO) and as element in Dye Sensitize Solar Cell (DSSC). For example, in [26] ZnO films are synthesized via hydroxides deposition and thermal treatment, in order to apply them in DSSC as substitute of TiO_2 due to its similar electron-injection process. The great interest about ZnO is motivated by higher electron mobility than TiO_2 and its huge variety of nanostructures, which are preferred to bulk material to obtain larger surface area. TCO materials must have an energy gap above 3 eV, a resistivity of the order 10^{-3} Ωcm and a transparency higher than 80 % in visible range. Essentially, basic materials for TCO are ZnO, SnO_2, In_2O_3, and CdO, not used for its toxicity. To obtain such resistivity, a doping process is necessary, but it has the same limitations seen for ZnO (Section 1.4): it is easy obtain n-doping, but difficult p-. The most used TCO material is Indium Tin Oxide (ITO). However ITO producing process is very harmful for environment and highly expensive due to indium scarcity. So other materials were considered, and doped ZnO is the most suitable because of its already mentioned non-toxicity and availability, also valid for doping elements as aluminium oxide. Nowadays the same conductivity of ITO was reached by Aluminium doped ZnO, but some problems are still present: weak stability in oxidizing or humid environments (due to chemical activity of Zn) and absence of a high rate deposition technique on large area substrate [27]. In photovoltaic applications doped ZnO films can be used as transparent electrodes in organic and hybrid solar cells, and as nanostructured highly scattering layers or photoanodes for solar hybrid devices [9]. In addition to these, ZnO as TCOs finds application also in flat panel displays, liquid crystal displays, in smart windows and other optoelectronic devices [28].

ZnO nanowires epitaxially grown by vapour phase transport process using Au as catalyst and as substrate, were obtained in order to build an UV-laser at room temperature [29]. This is possible because exciton energy has a high value of 60 meV, more than thermal energy (26 meV), and because low dimensional structures lower the stimulated emission threshold. In effect, quantum size effects yield a substantial density of states at the band edges and enhance radiative recombination due to carrier confinement. So high and sharp peak emission was achieved even without

resonance cavity.

The biological applications range:

- ZnO quantum dots were covalently linked to biorecognition molecules such as peptides, antibodies, and nucleic acids [30]. Then they can be used as fluorescent probes in cancer targeting (to detect cancerous cells) and in-vivo bioimaging by attaching the corresponding antibodies to the bare surface of ZnO quantum dots.
- Cell drug delivery [31].
- Some applications related to its antimicrobial and antibacterial activities [32]: ZnO is suitable as bactericide both in inorganic and in organic compounds, for example in those foods sensitive to intense thermal treatment [33].

Nanostructured or also bulk doped ZnO is particularly suited as diluted magnetic semiconductor due to its Curie temperature above room temperature. Manganese is the impurity most studied because it optimizes the ZnO ferromagnetism. Moreover other factors influence the ferromagnetism, such as fabrication conditions and processing. It is believed that defects or vacancies are the explanation. [34]

ZnO is widely used as an additive in the production of a variety of materials and products, including plastics, ceramics, glasses, lubricants, adhesives, paints and ointments [35]. In particular, ZnO nanoparticles are used to improve electrical properties of conductive polymers, for example PEDOT:PSS, to obtain excellent organic optoelectronic materials [36]. ZnO nanoparticles tend to transform benzoid structure of chain into quinoid structure, essential to conjugation conduction.

As mentioned in Subsection 1.1.4, ZnO strongly adsorbs NO_2 and SO_2 and catalyses their decomposition by alkanes. This could be very useful because NO_2 and SO_2 are two of the most harmful environment poisons, responsible of acid rains and of photochemical smog. In effect many researches talk about ZnO applications for desorption of nitrogen and

sulphur oxides ($De - NO_x$ and $De - SO_x$ processes) in a manner much more economical than noble metal catalysed processes [11], [12].

There is also the possibility of applying ZnO as chemical sensor, due to its high sensitivity to toxic and combustible gases, enhanced by high surface area nanostructures [26]. Other applications include: surface acoustic devices, optical waveguides, in spintronics [4], as UV-filter in sunscreens [35] and as cantilevers in Atomic Force Microscope [18].

Chapter 2

Pulsed Laser Ablation in Liquid technique

2.1 Advantages respect to Pulsed Laser Deposition and other techniques

In recent years, Pulsed Laser Ablation in Liquid (PLAL) is becoming more and more popular and investigated, and nowadays it is competitive to other techniques to obtain nanostructures. In general we can consider PLAL as an evolution of Pulsed Laser Deposition in order to synthesize various types of 0-D nanostructures, which eventually can be grown in a thin film. The main difference lies in the ambient surrounding the ablated material: not gas or vacuum as in PLD, but a liquid. So the ablated material is not ejected in one direction, but it is scattered inside the liquid. From the point of view of the apparatus there is a big advantage: PLAL does not require a vacuum chamber because ablation happens simply in the container of liquid. In some cases a chamber can be used to control the temperature or to prevent undesired reactions for example between flammable liquid and oxygen in air, but generally vacuum systems or pumping gas systems are not required in PLAL. Another limitation of PLD is the low rate of production; studies on ablation rate and on crater formation [37] indicate that liquid medium enhances the ablating effect of laser pulse, and future development could make it suitable for mass production of nanoparticles.

The PLD apparatus without the vacuum chamber is very economical and simple: it consists only of a laser, which can be so small to make this technique portable, an optical path with mirrors and lens, the liquid in a beaker and the target. Another huge advantage of PLAL respect to other techniques is the absence of by-products. In effect the greatest part of other techniques to obtain nanoparticles is based on chemical reactions of precursor containing species of desired material with other compounds. The products are the nanostructures and frequently one or more by-products, that must be removed from solution. This comports a loss of time and money, and usually a possible pollution of the environment; instead PLAL is famous to be a environment friendly technique [38]. On the other hand, PLAL is a physical technique (PLD itself is a Physical Vapour Deposition method), so chemical reactions are not mandatory and the products may be composed by the same elements of target without formation of other species. However if adequately planned, chemical reactions can happen during or after ablation; for example many metals ablated in water can transform in respective oxides depending on conditions of ablation. Other reactions can be planned, such as melting, welding, sintering, fragmentation and recrystallization; these increase the huge variety of obtainable structures in PLAL.

Moreover new structures and nanostructures are investigable with PLAL, because during ablation extremely high levels of temperature and pressure are reached. This implicates that structures not obtainable with other techniques at room temperature and pressure can appear. For example nanodiamond particles were synthesized from graphite target in water and ethanol [38]; this means that a temperature of at least 4500 K and a pressure of at least 10 GPa were reached. Another advantage is the absence of limitations in choice of material. In effect every target is suitable for ablation (metals, semiconductors and polymers, but also liquid), and absorption of photons of laser happens also if the material is transparent at that wavelength. An explanation is present in [36]: although the energy of the laser beam is lower than the band gap of the semiconductor, electrons are still excited into its conduction band via the non-linear two or three photons absorption (due to the high laser peak intensity). Moreover PLAL can be effectuated also starting from powder or nanostructures already in

solution. In these cases re-ablation or modification in liquid could occur. A last advantage that we can mention is the huge variety of parameters that one can control to optimize the products. Definitively, we can state that PLAL combines the compositional control of vacuum deposition techniques and morphological control of liquid-based synthesis approaches [39].

Nevertheless, PLAL presents also some disadvantages. One of these is the impossibility of making prediction about characteristics (dimensions, morphology...) of produced species, due to the difficulties in studying and modelling a process at such high temperature and pressure. So every new material has to be investigated from scratch, and also a small variation in ablation condition could originate a big variation in products. We can resume saying that an aleatoriety in produced species is constantly present in all PLAL experiments, and it causes difficulties in prediction of results. So in any experiment involving PLAL, each parameter must be controlled with care and varied in a systematic and rigorous way, in order to perform a right study on properties of ablated materials.

2.2 Fundamental mechanism of PLAL

As mentioned, PLAL apparatus is very simple. It consists of:

- A pulsed laser of wavelength which can be infrared, visible or ultraviolet. Depending on material generating beam, the pulse duration is fixed, and the range typically used in PLAL is from femtoseconds (fs) to nanosecond (ns). Other parameters as energy or repetition rate can be adjusted for the ablation.
- A beaker containing the liquid and, if required, an appropriate system to cover it to prevent splashing of liquid outside the beaker. It is important to know the volume of liquid and, of consequence, the thickness of liquid crossed by beam.
- The target completely submerged inside the liquid. However the target can be in the form of powder, dispersed in liquid.
- A suitable optical path that directs the beam from the laser to the target. The disposition of optical elements depends on the type of

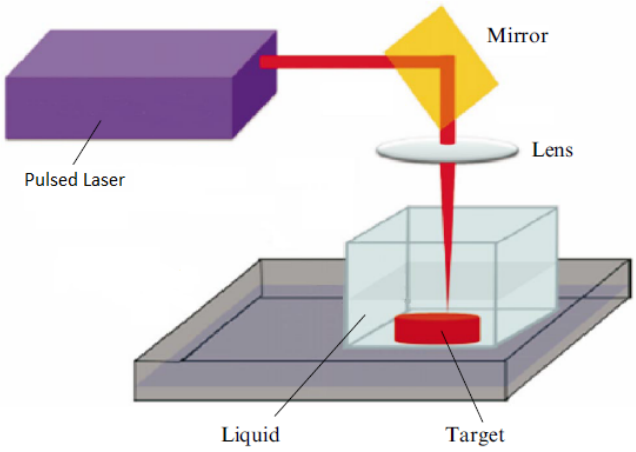

Figure 2.1: A schematic view of a Pulsed Laser Ablation in Liquid system; readapted from [38].

planned incidence with target. Sometimes the beam crosses a wall of the beaker, so even zero mirrors are necessary if laser is horizontal; other times the beam comes from upper side, so at least one mirror is required. The lens is positioned in order to focus the beam on surface of the target, so at a distance equal to its focal length, with some correction due to path in liquid.

In contrast with the simplicity of the technical realization, the explanation of phenomena is quite difficult and not completely understood. During ablation, all elements (laser pulses, liquid, target and produced nanostructures) have interactions each other [40]. One of these is the interaction of laser beam during the penetration inside the liquid. In effect liquid and laser must be selected in order to guarantee transparency of laser pulse wavelength and to permit it to reach the target surface. Due to optical path in liquid, some corrections in focus are mandatory. Due to refraction or even self-focusing, the focal length of the focusing lens will change; this is particularly true for picoseconds (ps) and femtosecond (fs) lasers with high intensity. The increase of focal length, and so the increase of distance of target surface from the air focus point, is:

$$\Delta f = l\ (1 - \frac{f}{\sqrt{n^2 f^2 + (n^2 - 1) r^2}}) \tag{2.1}$$

Where f is the focal length in air, l is the liquid thickness, n is the refractive index of the liquid, and r is the radius of unfocused laser beam. When the radius of unfocused laser beam is very smaller than focal length (as typical in all practical situations), the Equation 2.1 can be written:

$$\Delta f = l\ (1 - \frac{1}{n}) \tag{2.2}$$

Another problem which we must pay attention to, is that even if the liquid was chosen transparent for laser beam, small attenuation is unavailable, due to absorption of photon and to scattering by liquid molecules. The light intensity decreases exponentially in agreement with:

$$I_v = I_{v0}\ exp[-\int_0^x \mu_v dx] \tag{2.3}$$

Where x is the path length and μ_v is the attenuation coefficient, composed by absorption coefficient α and scattering coefficient at that specific wavelength. When scattering is negligible, Equation 2.3 can be simplified in Lambert-Beer law:

$$I_v = I_{v0}\ exp(-\alpha x) \tag{2.4}$$

Absorption and scattering can be caused, in addition to liquid molecules, by the ions in solution and by the products of ablation.

The possible interactions of product must be considered every time, even if their a priori prediction is not simple. Interactions between ablation products and laser beam cause first of all a reduction in energy reaching the target and, more importantly, an alteration of these products. Obviously, these interactions are influential when the ablation time is quite long, especially when the nanoparticles are metallic with the surface plasmon resonance fitting the laser wavelength. Absorption of photons by produced nanoparticles can lead to:

- Heating of nanoparticles until their melting, if melting temperature is low, or even partial vaporization causing a reduction of dimensions.
- Welding of two nanoparticles and, if phenomenon is widespread to many nanoparticles, sintering. This can be useful to sinter together two different target materials.
- In case of metals, if laser photon energy is larger than the material

work function, the laser irradiation could also induce photoionization of the particle, which could cause fragmentation of the particle by spontaneous fission due to charge repulsion inside the particle, also known as Coulomb explosion. In this way smallest nanoparticles are obtained.

- Induction of thermoelastic stresses.

The most important interaction which happens during the process is between the solid target and the laser pulse: the ablation. There are five main steps: an optical emission, a first shock wave, the straight jet ejection, the cavitation bubble which includes the solid ablation process, and a second shock wave. They are observable in the shadowgraph images of Figure 2.2.

The optical emission is irradiated in the period $0 - 50\ ns$ after the impact of the laser pulse with solid surface. Usually multiple peaks of emission are present, corresponding to electron transitions between electronic bands; moreover a continuous emission band is present in the spectrum, due to other effects [41].

Then, at *ca*. 50 ns, the first shockwave emission propagates inside the liquid with pressure up to 1200 MPa. This is a way to relax the excess quantity of laser energy absorbed by solid surface; in particular, calculation showed that 35 % of laser energy is consumed in shockwave emission [40]. Actually the emitted shockwave is double: the first is in the solid and the other in the liquid, but the solid shockwave is difficult to study and has no effect in products formation.

The straight jet ejection is a very rapid material expansion perpendicular to surface target, starting 5 μs after the impact and continuing up 50 μs, with a velocity of 10 000 m/s [42]. Its formation is probably explained by photothermal heating of solvent by the incident laser irradiation, enhanced by the reflected laser beam.

The cavitation bubble is an hemisphere with centre in the point of impact of the laser pulse with solid surface. It is formed by the expansion of emitted materials and by the local heating of the solvent in the vicinity of the ablation spot; we can argue that a state of plasma is reached inside the bubble, containing atoms, ions and molecules of material and liquid. The bubble starts its growth few μs after the impact and reaches its maximum

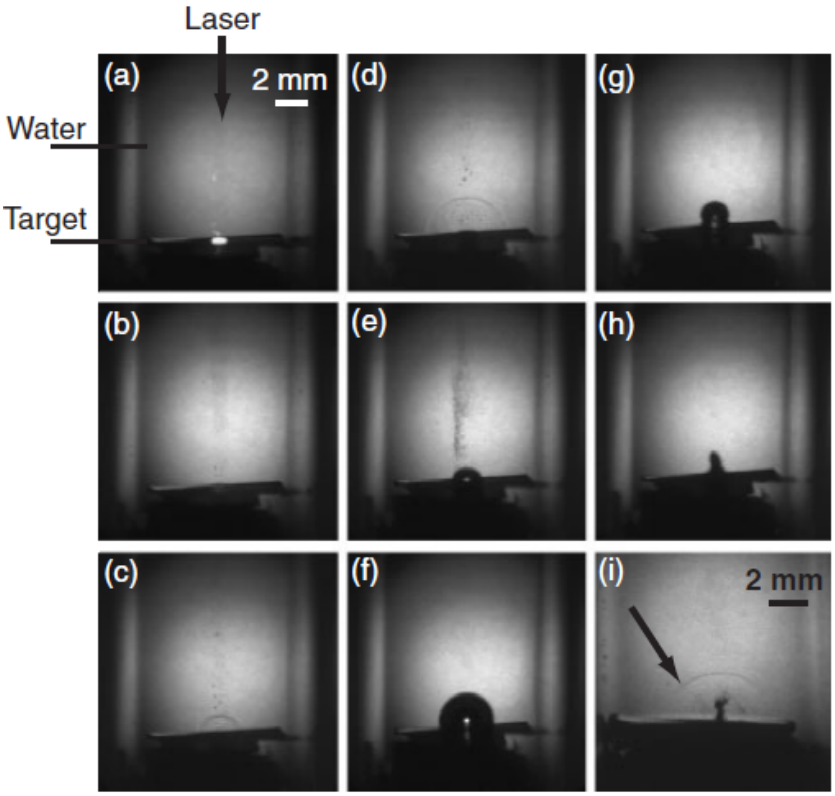

Figure 2.2: Time-resolved shadowgraph images of the laser ablation process for a Ag plate in water. The delay times from laser irradiation are: (a) 0 ns where we can see the optical emission, (b) 60 ns, (c) 570 ns and (d) $1,3$ μs, where the first shockwave is evident, (e) 9 ms, (f) 160 μs, (g) 260 μs and (h) 290 μs, where we can follow the growth and the collapse of cavitation bubble and at the end (i) 300 μs where we can admire the second shockwave [41].

radius of $2-4$ mm after $100-200$ μs, both depending on laser fluence, pulse duration and solid properties. It is important underlining that bubble dimensions exceed the crater size on target (*ca*. $0,2$ mm). After that, the bubble rapidly collapses and, due to aggregation and cooling, there is the release of colloidal particles: nanostructures are finally formed.

After the collapse of cavitation bubble (300 μs), a second shockwave is formed, due to new increase in pressure.

Similar results were obtained in [43], whose shadows revelation was reported in Figure 2.3. The main steps correspond to those of [41], with some additional calculations and observations. From the black body radiation

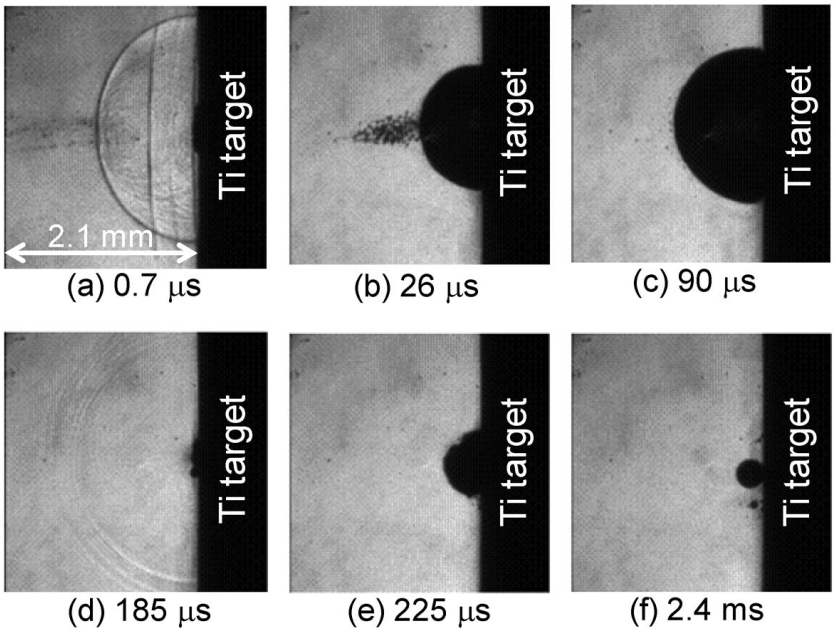

Figure 2.3: Snapshots of cavitation bubbles observed at various delay times after laser ablation of a *Ti* target in water [43].

emitted in the first 20 *ns* after laser irradiation, a temperature of 4300 *K* was estimated. From this value and from the estimation of number of ejected atoms, the evaluate pressure was $0,8$ *GPa*. Following a different estimation method reported in [44], the calculated pressure was 1 *GPa*. As in previous case, the two shock waves were observed, as we can see in Figure 2.3 (a) and (d); calculations stated that propagation speed of the wave agreed well with the sound velocity in water. In Figure 2.3 (b) straight jet ejection is evident at $20 - 26$ μs; moreover a later shadow photo (Figure 2.3, e) reports evidence of a second irregular and oscillating cavitation bubble, which collapses in a smaller sphere at $2,4$ *ms*. A question about the place of growth of nanoparticles (inside or outside cavitation bubbles) was solved via nanoparticles detection by laser light scatter. Particles ejected from the target are transported toward the cavitation bubble. A strong scattered laser light was observed in the region close to the boundary between water and the cavitation bubble, suggesting a fast growth of nanoparticles after the transportation into the cavitation bubble. This fast growth may be attributed to the lower temperature inside the cavitation bubble. So one can assert that the growth of nanoparticles occurs inside the cavitation bubble.

Moreover, the straight jet ejections can be inductively explained: due to high laser light scattering, they probably correspond to the ejection of child bubbles full of nanoparticles. After the collapse, the enhanced pressure and temperature cause the growth of the second cavitation bubble. The inside of the second cavitation bubble was occupied by a large amount of nanoparticles. The size and the structure of nanoparticles stored in this second cavitation bubble would be probably different from those of nanoparticles ejected from the first cavitation bubble in the straight jet ejection. However, further investigation is necessary to understand the relationship between the dynamics of the cavitation bubble and the synthesis characteristics of nanoparticles.

In order to perform an optimal ablation in liquid, some expedients must be followed. First of all, it is appropriate rotating the target to avoid a deep ablation crater. Alternatively, the laser beam can be delivered by scanner optics to move the ablation spot [40]. We can see two cases in Figure 2.4: in (a) the target is anchored on the bottom of the beaker, which is in rotation during laser irradiation; in (b) the target is the powders or particles in suspension and a rotation is performed via magnetic stirrer to homogenize the solution. In this last case, the laser focal point can be adjusted inside the solution or on the suspension surface. Alternatively, the system can be placed in an ultrasonic bath to homogenize the liquid.

Another possible implementation is limitation of liquid splashing which happens when the laser pulse crosses the liquid; this is particularly true when the surface of liquid is free and the radiation power is high [38]. In order to avoid the undesirable consequences, the radiation can be directed at a particular angle, the Brewster angle of 53^o, which minimizes the splashing; where inclination is not feasible, a simple coverage should be applied on beaker with a dedicated opening where laser pulse can enter. In addition to these, a p-polarized radiation can be used to minimize the reflection losses.

Many variations of PLAL technique are possible. First of all, the use of a microsecond pulse laser causes big changes in mechanism and in produced nanostructures. Due to low power density in millisecond pulsed laser, the main formation mechanism is based on the explosive ejection and

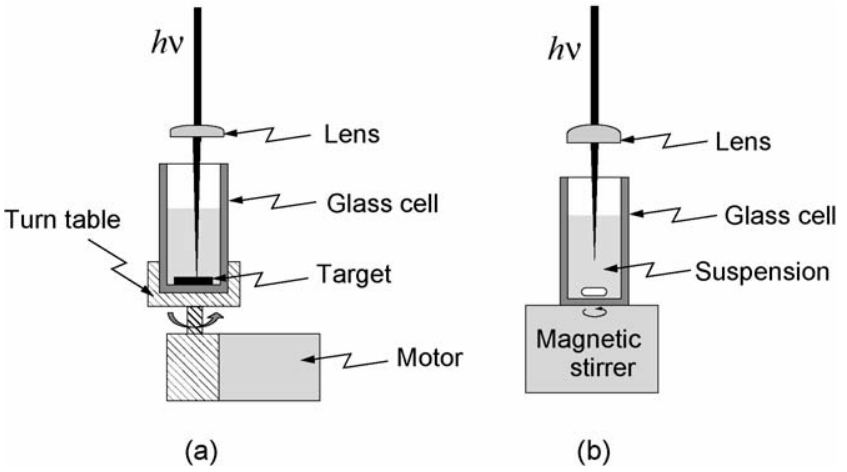

Figure 2.4: Typical experimental setups to rotate PLAL system. In (a) a solid target is mechanically rotated. In (b) the suspension is homogenized via magnetic stirrer [45].

the primary ablation products are mainly nanodroplets [46]. Hypothetical working mechanism is that laser irradiation could cause a local melting of the target. Owing to the heat transfer from the target, the adjacent liquid layer can be heated to a vapour or plasma state with a high pressure, and the expanding vapour/plasma splashes the molten target into a large number of nanodroplets, which then react with the liquid medium and produce the final nanostructures. However, in all PLAL experiments probably both mechanisms (the previously described thermal evaporation and this one, the explosive ejection) may occur simultaneously and thus their effects should normally overlap to produce nanostructures.

A second possible variation is a hybrid between PLD and PLAL: essentially, the target is placed in air but the ejected plume goes to a liquid drop [47]. A variety of ablation product is reported as a function of laser wavelength: from perfect nanospheres to fragmented particulates, maybe for direct solid target removal.

Another possibility, already mentioned before, is ablation of powder or micro- or nano- particles in solution in order to further fragment them. The problem of focusing is resolved in smart way in [48], where the suspension flows in a small gap and the pulsed laser is focused in that point. This method is called Pulsed Laser Fragmentation in Liquid (PLFL). Laser can be used to induce a chemical reaction starting from a precursor, as in the

case of Pulsed Laser-induced Liquid Deposition (PLLD) [49].

Finally, as evidence that all materials can be ablated with PLAL, also metal liquid were used as targets [50]. *Ga* was used to obtain Gallium Nitride *GaN* structures, but also *In* and *Sn-Pb* alloy were ablated. In these cases a layer of product between metal and air elements was built as a microtower, with liquid metal inside.

2.3 Main parameters involved in the process

In general we can state that the influence of ablation parameters on properties of products is rather intricate, which can be used to adjust the ablation conditions for a particular task [38]. The product modifiable properties are so many: composition, structure, morphology, dimensions and their distribution, presence of defects, eventual second reactions, self-assembly, optical, electrical, ferromagnetic or thermal properties, and so on. All these properties of materials can be regulated by tuning ablation parameters. However it does not exist a right way to perform ablation; rather, it depends on properties that we want to achieve. For example in some applications monodisperse particles can be useful, so it is suitable to ablate with short pulses of short-wavelength radiation of limited power [38].

Some considerations can be done for influence of pulse duration on nanoparticles dimensions and production rate. The use of femtosecond pulses allows to achieve higher temperatures and pressures and for producing more dispersed particles with a narrow sizes distribution [38]. Instead, production in mg/h is greater in longer time pulse (*ns* than *ps* than fs), but ablation efficiency in mg/J decreases in the same scale of time [51].

Variation in distribution is narrower at short-wavelength laser radiations and dimensions are smaller [38], [42]. This last behaviour was reasonably attributed, at least in the case of metals, to the fact that the penetration depth of the short-wavelength radiation is enormously thinner that for the long-wavelength radiation. Hence, in the former case, much faster heating and (what is more important) cooling of the material take place, and these processes give rise to sharp temperature gradients. In few words, a smaller amount of substance is heated to a higher temperature. Laser wavelength also influences the ablation rate: it increases with increase of wavelength. A possible explanation is that the ablation rate depends more on the number

of photons rather than photon energy [32]. So smaller number of photons in short wavelength laser beam leads to smaller rate of ablation.

Laser energy strongly influences the results. Primarily, structure and morphology are affected by the energy of the laser pulse. In the case of Zn target [52], lower energy leads to a greater fraction of amorphous phase, whereas higher energy to a more crystalline structure. Moreover increasing energy, the morphology changes from nanoflakes to nanoparticles and finally to nanorods. In the case of low laser power, the plasma plume has a relatively low temperature and pressure, and density distribution inside is less homogeneous; so the weak plasma is strongly affected by liquid media, and the pre-formed ZnO clusters incline to self-assemble into low density nanoflakes. Contrarily, at high laser power, the plasma plume is intense, ensuring a longer plasma lifetime and a higher temperature and pressure in the plasma plume; in such conditions, the influence of liquid media will be much weaker. As a result, the nucleation and the growth of these species would obey to the habits of ZnO to develop along (0001) direction. The plasma at medium laser power would be in the middle between the previous two, producing spherical nanoparticles. Similar considerations can be applied also about defects through photoluminescence spectral analyses: increasing energy there is a reduction of interstitial Zn and an increase of oxygen vacancy. Energy has an impact also on products dimensions, but their dependence is conflicting in different papers [32], [38], [53]. Some researchers suppose that the increase in the laser intensity decreases the sizes of products, and the cause must be found in two key PLAL mechanisms (thermal evaporation and explosive ejection). The vaporization mechanism prevails at low radiation intensity. The nanoparticles formation rate and nanoparticles size are determined by the temperature and concentration of the ablated substance. Larger particles (tens of nanometres in size) are formed if the explosive ablation mechanism predominates, whereas if vaporization prevails, more dispersed particles (several nanometres in size) are formed. As we can see in Figure 2.5 (a), production rate strongly depends on the laser energy, with proportionality varying from linear to quadratic [51]. The change in proportionality over a certain threshold is probably caused by a change in ablation mechanism; the hypothesis of explosive ejection regime was proposed to justify such a violent increase in ablation productivity.

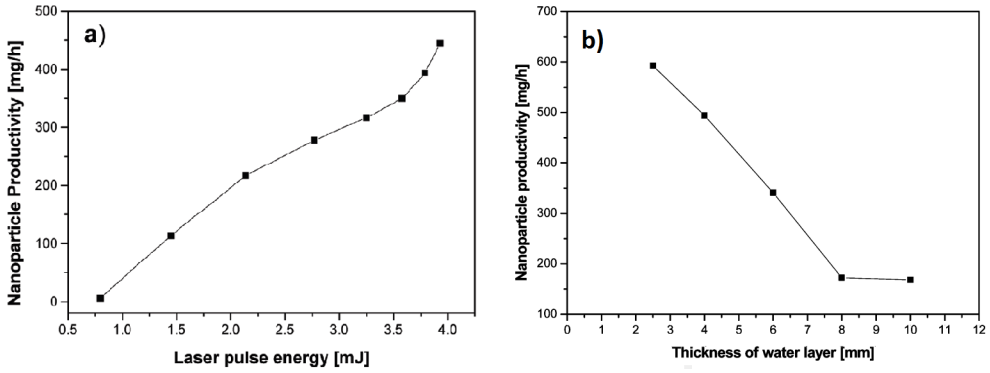

Figure 2.5: Al_2O_3 nanoparticles production rate as a function of the applied laser pulse energy (a) and of the thickness of the distilled water layer (b). Other conditions for (a) are 6 mm of distilled water layer and 5 kHz laser repetition rate; for (b) laser pulse energy of $3,8$ mJ and 5 kHz repetition rate at 120 mm/s scan speed [51].

A dependence of ablation efficiency from repetition rate exist, but only at very high values of repetition rate [51]. In effect at low repetition rate (< 2000 Hz) every pulse can be considered independent from previous one, due to typical duration of ablation phenomenon (hundreds of μs). Over this threshold, overlapping of pulses has a negative influence on ablation efficiency because the cavitation bubble is substantially opaque to radiation.

Obviously, longer ablation times mean more quantity of products, in a linear dependence. Less obvious is the dependence on characteristic of products: longer ablation leads to more monodisperse nanoparticles [38]. However, a further increase in the treatment time (up to 45 min) induced destruction of the compound.

The liquid, one of the most relevant protagonists, should be chosen with particular care. First of all, it implicates two possibilities: reactive-PLAL and non-reactive-PLAL, depending if the target material reacts with the molecules in liquid or not. A peculiar example of reactive PLAL can be found in [43]: a target of Ti is immersed in N_2 liquid to obtain Titanium Nitride TiN nanostructures. Even in the case without reaction, choice of solvent and of eventual surfactants is relevant; in particular, the liquid environment affects ablation, particle formation and cluster mechanisms and can be used to adjust the structure, size and shape of nanoparticles [54]. For a correct choice of surfactant, the value of zeta potential (ζ) should be

known, so the class of surfactant will be identified between anionic, cationic or amphoteric. Optimal choice leads to smaller nanoparticles and narrower dimensions distribution. The solvent choice must be performed depending on its properties: density, surface tension, viscosity, dielectric constant and so on. The shape, the defects and the self-assembly derive from electrostatic interactions between species in plasma and molecules of liquid; so knowledge of the dielectric constant of liquid and the dipole of products is fundamental. For example in xylene a narrower sizes distribution and colloid solution stability were obtained, attributed to high viscosity of liquid [38]. Interactions between liquid and material continue after ablation: some papers [53], [55] report a progressive decrease of oxygen vacancy in oxide nanoparticles, depending on presence and position of oxygen in solvent molecules. Also mixtures of more solvents are possible, with a great variety of obtainable structures. For example in [56] and in [57] a mixture of water and ethanol is used, both with Zn target. In the first case, where also SDS is added in solution, beautiful intersections of layers are produced (as we will see in Section 2.4), recalling the form of flowers in nano scale; it was argued that layers are formed of $Zn(OH)_2$ and corners of ZnO, in the sites where ethanol hides water to Zn, blocking thus the hydroxidation. In the second case the mixture leads to a particular product, the hollow nanoparticles, as we will see better in Section 2.4. Another example where liquid greatly influences the product, in this case the composition, is reported in [54]. Here, pH of aqueous solution is varied with addition of $NaOH$ and a Zn metal target is used: at $10 < pH < 13$ nanoparticles were formed of Zn, meanwhile at $6 < pH < 9$ ZnO nanoparticles were synthesized. Moreover they were able to control the size and the stability of ZnO nanoparticles simply by changing the pH; in effect dimensions decrease when pH increases in both ranges, but stability problems were observed near to transition pH.

The thickness of overhead liquid plays an important role on productivity; it was noticed that production rate continuously increases lowering the liquid thickness [51] (see b in Figure 2.5), but due to configuration where laser crosses the beaker glass in front of the target, a liquid layer smaller than $2,5\ mm$ was not feasible. A possible motivation is that the increased absorption and the scattering of laser irradiation by already ablated nanoparticles can occur, diminishing thus the ablation rate when the

liquid layer is thick.

Moreover the use of a flowing liquid appears to have an impact on productivity due to elimination of ablated particles and of generated air bubbles from the ablation zone. An increase in productivity was estimated of 20 % [51].

Interesting ablation experiments can be performed varying the position of target in proximity of focus point of lens [58]. The target was Ti; ablation leads to different stoichiometry and structures of Titanium Dioxide nanospheres at different focus conditions. In particular, above focus ablation may result in low fluence and lower temperature and pressure of plasma, so insufficiently oxidized nanoparticles of titanium are formed. Instead just below focus, the focus point is inside the cavitation bubble, leading to formation of anatase (a phase of Titanium Dioxide metastable at room temperature and pressure) particles as main product.

As already mentioned, rotation of target is advantageous to avoid deep ablation craters. Moreover the velocity can be optimized to enhance the production rate [51]. In Figure 2.6 is reported the dependence between the productivity and the scan speed, and a schematic explanation of this phenomenon: the scan speed is optimal when a second pulse irradiates a point inside the region of thermal effect (decreasing the evaporation heat) but outside the cavitation bubble of the first pulse. In this way, interference due to overlapping of pulses is avoided. So the optimal scan speed strongly depends on repetition rate, but also on the properties of material.

Temperature may have a great impact on properties of products. For example in metal target in water, oxidation can be inhibited at low temperature, and also variations in absorbance spectrum occur [54]. Also differences in structure were noted varying the temperature: from amorphous welded spheres at room temperature to crystalline nanorods radially growing (Figure 2.9) at $60 - 80^{o}C$, in the case of Zn target [59]. Another possibility is performing a thermal treatment after ablation.

The plasma contains electrons and ions, which can be driven by external electric and magnetic fields [46]. Therefore, the application of external electric and magnetic fields to the plasma plume can control:

- The kinetics of reactions at the plasma/liquid interface.
- The clustering of the produced species into various nanostructures of

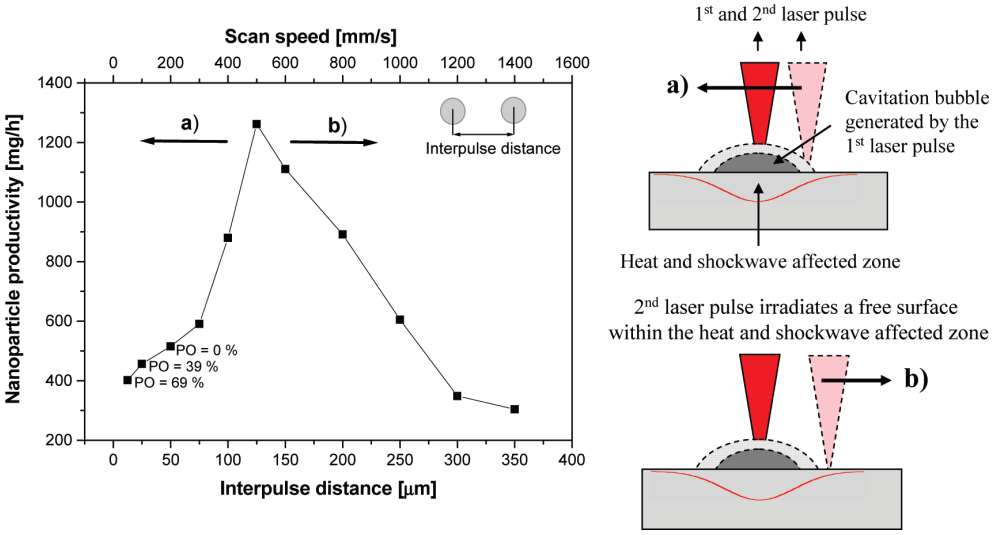

Figure 2.6: (Left) productivity of Al_2O_3 nanoparticles as a function of interpulse distance and scan speed using a fixed laser pulse energy of $4,6\ mJ$ at $4\ kHz$ repetition rate and a $4\ mm$ thick distilled water layer. Calculated laser pulse overlaps (PO) are also shown in percentage. (Right) simplified scheme of the processes taking place under laser ablation of a target material in a liquid, demonstrating the impact of the cavitation bubble and heat affected zone on subsequent laser irradiation [51].

controlled sizes and shapes.

- The assembly of these nanoparticles into larger nanostructures.

In addition, because the surfaces of nanoparticles are charged, the application of electric field after synthesis can affect their size, shape and assembly. The use of an external electric field also assists in the fabrication of high pressure nanophases, i.e., metastable phases of nanostructures that can not be prepared under normal experimental conditions.

Gas bubbling is a way to alter the composition from target to nanostructures. Ablating an oxide target in presence of oxygen bubbling, products with less oxygen vacancies than normal ones are obtainable [30].

Nanostructures in solution have different stabilities depending on material composition and liquid. After ablation, a certain grade of stability is guaranteed by surface charge. However, after a certain rest time in liquid, structures tend to lose their charges and can modify themselves, producing new self-assembled structures. This is the case of ZnO nanospheres reported in [60], left in liquid from two weeks to two months at room temperature. A sedimentation and an assembly in tree-like nanostructures were observed, involving the 90 % of initial nanospheres; the assembly was ascribed to preferential direction of aggregation, due to interaction of nanoparticles and SDS surfactant. Also in [4] there is an interesting example of aggregation induced by aging: in a first stage, a variable number from 6 to 35 of ZnO quantum dots assembles to form drop structure; after that, many drops assemble together in a leaves-like group. These can be explained with electrostatic charge inside a drop, which favourites a specific pattern of assembly. If agglomeration is not desired, surfactants and/or pH adjusting additives may be used to stabilize the nanostructures [39].

2.4 Overview on obtainable nanostructures

The first materials ablated with PLAL were the noble metals, more or less 10 years ago. After some years, there was an increasing interest in ablation of all other metals, obtaining nanoparticles of the same composition or their oxides. Nowadays more and more attention is focused on ablation

of semiconductor materials, as oxides or ceramics. Also targets as alloys, polymers or bioconjugates materials were tested.

When the target is a noble metal or material such as carbon or silicon, the ablation leads usually to pure elemental products, which are formed in the laser generated plasma in the absence of any chemical reactions with the liquid medium [46]. On the contrary, when more active metals are ablated in water, the as-prepared metal nanoparticles normally react with water, leading to the formation of oxide or hydroxide nanostructures. Also in this case, a smart way to stabilize the produced nanoparticles and to prevent reactions is the addition of surfactants. The other typical class of material, the oxides, leads to formation oxide or hydroxide nanostructures, depending on advancement state of typical reaction. We can see the example of ZnO target in water in Equation 2.5.

$$Zn^{2+} + O^{2-} + H_2O \leftrightarrows Zn(OH)_2 \leftrightarrows ZnO + H_2O \tag{2.5}$$

Where the ions from plasma state interact with water to form hydroxide, then gradually the hydroxide transforms in oxide and water. Many metastable products can be obtained via PLAL. In addition to anatase TiO_2 and diamond already mentioned, we can mention other examples:

- Metastable Zinc Peroxide ZnO_2 nanoparticles produced by ablating a metal Zn target in a very oxidizing environment, such as aqueous solution with 3 % (w/w) of Hydrogen Peroxide H_2O_2.
- Silicon metastable phases: microcubes with a Zinc-Blende structure, via ablation of a Si target in inorganic salts solution; nanocrystals with face centred cubic (fcc) crystal structure through a long-pulse (μs) laser ablation in water.
- A novel type of carbon micro- and nanocubes with a $C8$-like structure in the same inorganic salts solution used for Si, ablating a Si target covered by amorphous carbon (A and B in Figure 2.8).

The products shapes are often solid spheres. However, a vast variety of different morphologies has been observed, such as hollow particles, cubes, rods/spindles/tubes, disks/plates/sheets, and more complex structures

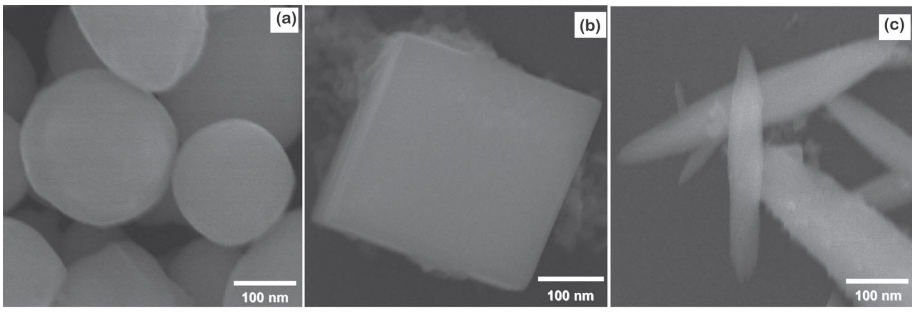

Figure 2.7: SEM images of nanostructures produced by conventional PLAL (*Ge* nanospheres, a) and electric field assisted PLAL with $14,5\ V$ (GeO_2 nanocubes, b) and $32\ V$ (GeO_2 spindle-like structures, c) dc voltages [46].

[40]. Among these micro-/nanostructures, some were fabricated with the assistance of external factors, such as templates and electrical field (see Figure 2.7), whereas others were formed directly by PLAL. In the case of non-spherical particles, the crystal structure and the surfactants in the liquid could strongly affect the morphologies.

A particular type of obtainable structure is hollow nanoparticle. They have attracted much interest due to their unique properties such as the high surface/volume ratio, low density and coefficients of thermal expansion, and they have found applications in catalyst support, rechargeable batteries, sensing, drug delivery, and biomedical imaging. The materials which reassemble in hollow particles are both metal (*Al*, *Mg*, *Ag*, *Cu*, *Zn*) and ceramic (*Si*, TiO_2). Kinetically, the bubble surface requires to trap enough clusters to form a shell, and the clusters mainly come from the liquid. Thus the clusters, undergoing Brownian motion, need enough time to diffuse to the bubble interface, which in turn requires a long lifetime. Two methods were discovered to favourite hollow nanoparticles: one is the ablation of materials highly reactive in water (such as *Al*, *Mg*), generating in this way atomic and/or molecular hydrogen gas which is trapped inside the nanoparticle in formation; the other is the use an ethanol-water mixture, thus the bubbles have longer lifetime (up to tens of second [57]) and formation of hollow nanoparticles is possible.

Another particular structure is core/shell nanoparticles. In its simpler case with metal target, the core is metal and the shell is its oxide, formed for oxidation of external layers by water. This principle is used in [61], where the effect of aqueous oxidation was controlled through surface mod-

ification by surfactant coverage and manipulation of laser parameters. In this case SDS surfactant was used and, depending on its concentration, it could have a capping effect limiting the oxidation to the external layers of Zn nanosphere, creating in this way a Zn/ZnO core/shell nanoparticle. Semiconductor-metal composite nanoparticles have been extensively studied for their attractive capability in improvement of catalytic and sensing properties and for their tunable luminescence.

There is another quite frequent shape in PLAL technique: cubic nanostructures. They are good building blocks for self-assembly of superstructures and mesocrystals, and due to the exposure of certain facets, they are also good candidates to study the surface-related properties. PLAL shows the ability to produce cubic particles under at least three experimental conditions: electrical field assisted PLAL, as seen in Figure 2.7 (B); with addition to solution of the mentioned inorganic salt that facilitates the formation of micro- and nanocubes, as A and B in Figure 2.8; intrinsic property of some materials with cubic structure, as the Ag in C and D of Figure 2.8.

PLAL also shows the ability to fabricate one-dimensional nanostructures. Typical examples are ZnO nanorods or spindles produced by PLAL of Zn in water at elevated temperature or with the addition of surfactants, and the ZnO nanorods assembled into three-dimensional clusters (Figure 2.9). Other examples include: $Mg(OH)_2$ nanorods, Ag_2O pentagonal rods and bars, Carbon Nitride CN nanorods from graphite in ammonia solution, GeO_2 (see c in Figure 2.7) and CuO nanospindles induced by electrical field. Also some kinds of nanotubes were synthesize: BN nanotubes and PbS ones.

We can also list a short series of 2D nanostructures (nanodisks, plates and layers) synthesized by PLAL. In majority of cases, surfactants are involved in formation: Ag_2O triangular plates, Zinc Hydroxide/Dodecyl Sulphate composite nanolayers, $AgBr$/CetylTrimethylAmmonium Bromide (CTAB) composite nanolayers.

There are also a few reports on three-dimensional complex nanostructures formed directly by PLAL, due to self-assembly of laser-produced nanostructures. Here the time is an important variable. Examples of self-assembly behaviour are: tree-like Zn/ZnO nanostructures, $Cd(OH)_2$ nanotetrapods and nanoflower-like structures, and the formation of Zinc

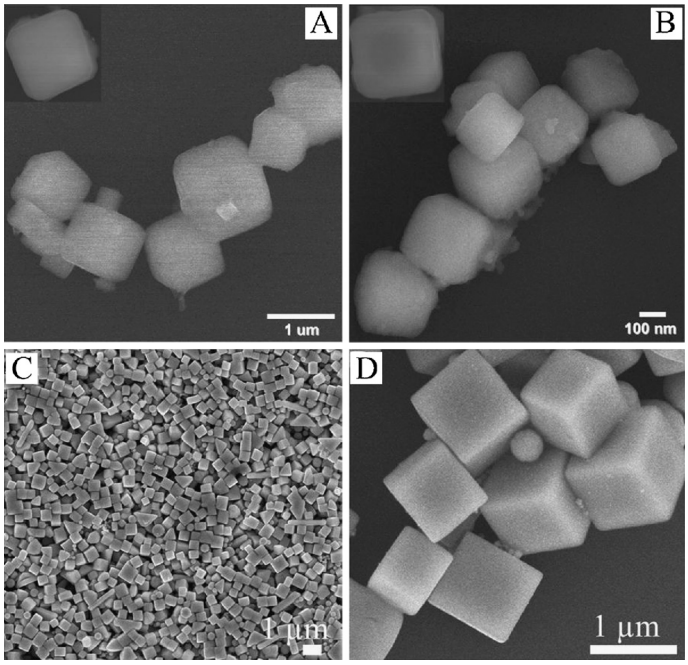

Figure 2.8: (A) and (B) SEM images of carbon micro- and nanocubes fabricated by PLAL of amorphous carbon in liquid. (C) and (D) SEM images of Ag_2O cubes fabricated by PLAL of Ag in aqueous solution of polysorbate 80 [40].

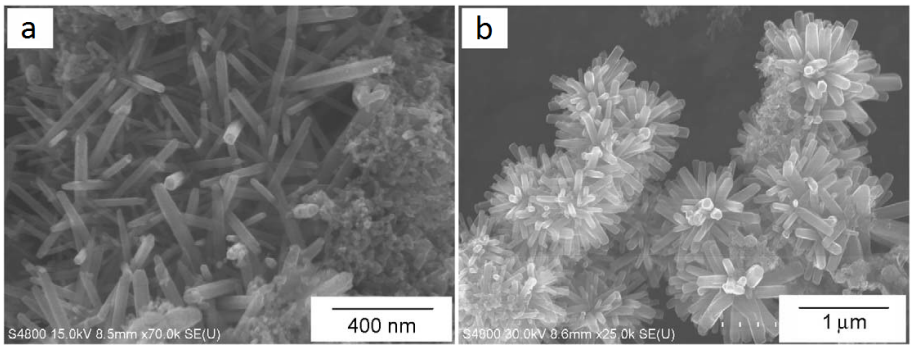

Figure 2.9: SEM images of ZnO nanostructures (a) aged at 80^oC for 40 min after ablation at room temperature and (b) prepared in a CTAB solution at $0,14$ M [59].

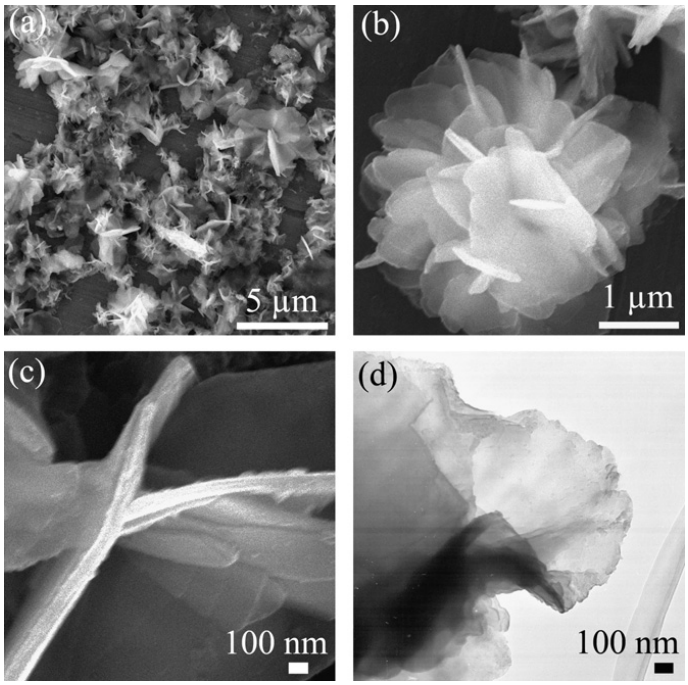

Figure 2.10: SEM images of products from laser ablation of Zn in ethanol-water solution of SDS: (a) a general view, (b) a typical nanostructure assembled by nanolayers, (c) jointed nanolayers with higher magnification. (d) TEM image of a typical nanolayer on a nanostructure [56].

Hydroxide/DS flower-like structures (Figure 2.10).

In conclusion, authors of [38] make an exhortation to develop PLAL in particular fields:

- Ablation using multicolour laser or a pulse train excitation.
- A deeper comprehension of ablation mechanisms and of involved phenomena, in order to eliminate the existing drawbacks of the method: noticeable nanoparticle size variability and relatively low efficiency of laser ablation.
- Trying growing μm thick films composed of many alternating layers about 10 nm thick with different chemical compositions.
- Trying synthesizing doped multicomponent nanoparticles.

Chapter 3

Experimental Design

3.1 Realization of experimental apparatus for ablation process

In order to perform this thesis work about ablation of oxide materials in liquid, a dedicated setup was built. The components are listed in Section 2.2. The target material has no particular requirement; we have to couple the liquid with the pulsed laser so as to guarantee the transparency at that wavelength. As liquid we choose distilled water, because it is safe and not flammable, and because for the first experiment we consider appropriate starting from the most used liquid in PLAL. However we can add surfactants to see the interesting differences induced in nanostructures formation; Sodium Dodecyl Sulphate (SDS, see the chemical formula in Figure 3.1) is a very used surfactant in PLAL, so we choose it. As consequence, a laser wavelength must be selected in the regions of low absorbance in water spectrum reported in Figure 3.2. We discard infrared and far ultraviolet due to high absorbance of water. An excimer laser based on Krypton Fluoride (KrF) was available; it has a wavelength of 248 nm and pulse time of 30 ns. At that wavelength, absorption coefficient of water is $ca.\ 10^{-3}\ cm^{-1}$; so for example with a water thickness of 2 cm, the $99,8$ % of radiation will be transmitted.

The optical path must be built from the laser exit to the surface of target. We choose the configuration where the laser pulse comes vertically, crosses the liquid free surface and hits the target surface. Because the laser beam exits horizontally, we build a system to support a mirror, a lens and a

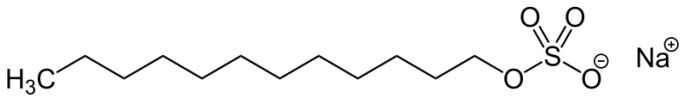

Figure 3.1: The chemical formula of Sodium Dodecyl Sulphate.

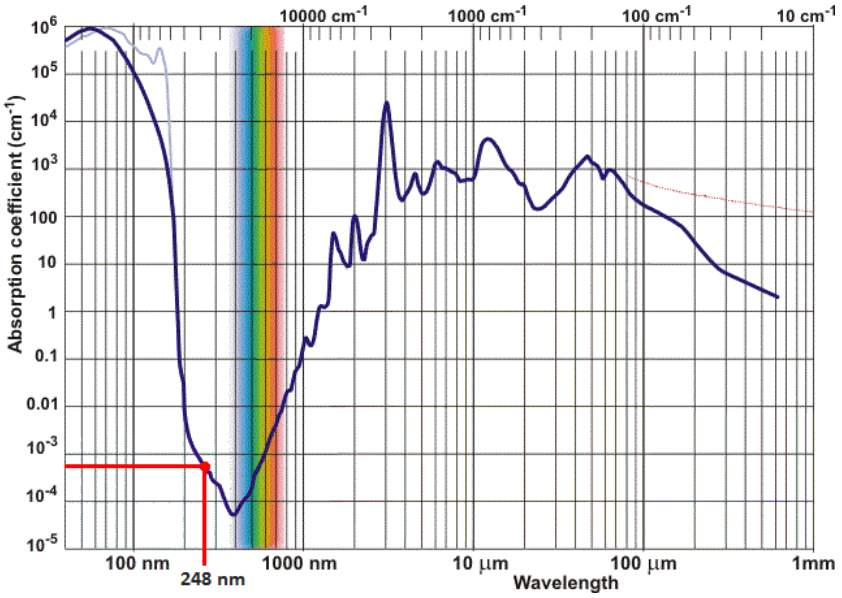

Figure 3.2: Absorption coefficient of water in range of wavelength 40 nm – 1 mm, where the wavelength of our laser is highlighted.

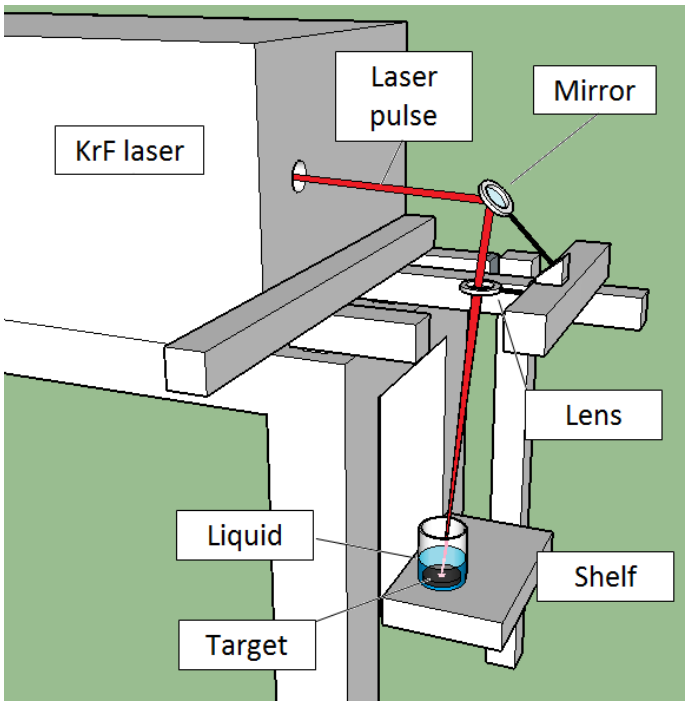

Figure 3.3: A schematic representation of built apparatus for PLAL, with indication of main components. The laser beam is in false colours to see the path; the shields are not represented.

shelf to put the beaker; our apparatus is schematised in Figure 3.3. Due to ultraviolet radiation, the mirror is in quartz; the lens has a focal length of 50 *mm*.

In particular, the shelf is assembled so that its distance from lens can be regulated. In effect, over the shelf there is a beaker with a variable level of liquid; and due to variable level, adjustment in height must be realized to focus correctly in agreement with Equation 2.2. Moreover in this way some interesting tests could be performed varying the position of the target above or below the focal point [58]. The variable height is also useful to find the right position of the focus. In effect it is not simple calculating and verifying the exact position where placing the shelf, because many factors must be taken in account: the height of the beaker bottom, the height of the target, the thickness of the lens, *etc*.. So after a first-estimate calculation, we shoot a set of pulses on a UV sensitive paper at various heights of shelf. Inspecting the areas of these spots at optical microscope, we find the minimum one and so it corresponds to the correct focal point. Moreover

with the spot area seen in this way, we can transform the energy of the laser into the fluence. To prevent irradiation of harmful intense UV pulse, we use a poly methyl-methacrylate box to cover the optical system and a double layer of the shelf in polymer and metal, in addition to UV safety goggles.

After the realization of apparatus, we must decide which parameters to set. We choose:

- Target: we will use three targets. The first and most important is AZO target, with a composition of 2 % (w/w) of Al_2O_3, so the ratio of elements is $Zn_{0,9535}Al_{0,0310}O$; the other two are pure ZnO to see the difference with doped one, and anatase TiO_2 to see the nanostructures of a material with similar applications of AZO.

- Ablation time: we will perform analyses at different ablation times. To avoid too long tests where conditions can change (temperature of liquid, evaporation of liquid, decrease of pulse energy, excessive interactions with particles in solution), we put a maximum time of 1 $hour$. The selected times are: 5 min, 10 min, 20 min and 60 min.

- Thickness of liquid: it is quite difficult measuring directly due to alteration of water and beaker glass. We can overcome this problem calibrating the thickness h with the liquid volume V, for that beaker with each target. In the case of AZO the calculated relation is:

$$V(mL) = 2,48\ mL/mm \cdot h(mm) + 3\ mL \tag{3.1}$$

  The chosen volumes are: 6 mL, 7 mL, 10 mL, 15 mL and 25 mL, corresponding to $1,21\ mm$, $1,61\ mm$, $2,82\ mm$, $4,84\ mm$ and $8,87\ mm$, respectively.

- Laser energy, with the drawback that after some time KrF laser reduces the maximum energy at that repetition rate. So we choose a typical energy value not excessively high, 150 mJ. However scan in energy will be performed at energy of: 50 mJ, 100 mJ, 125 mJ, 150 mJ and 200 mJ.

- Concentration of SDS: we will test two concentrations of SDS, one under the Critical Micellae Concentration (CMC, $0,0081\ M$ for SDS)

and one above. The under CMC concentration does not cap the products. The above one is calculated so that the excess from CMC guarantees a complete capping of products, with hypothesis about mass ablated, dimension of particles and thickness of the capping shell equal to the length of the surfactant (for SDS 2 nm). The SDS concentrations will be $0,005\ M$ and $0,01\ M$.

We decided to do not vary repetition rate, because as we saw in Section 2.3 it requires very high value to see some differences in characteristics, and our KrF laser can not reach them. We set a repetition rate of 30 Hz, greater than 10 Hz usually set in literature, so as to have a faster production.

To conduct an ablation first of all we have to weigh the target in order to have the data for calculation of the ablated mass in solution. We arrange on the shelf the beaker, with the target and the known quantity of liquid inside. Then we switch on the pointer laser and place the beaker in the position; we can aim at the ablation position on the target quite precisely. After that, we work on laser: we put the protection shields and set the desired parameters (repetition rate and energy). During the ablation some interruptions are useful, in order to control that temperature of the system does not increase and to change the ablation point. In effect also ablation craters with depth of 1 mm relocate the target surface out of the focal point.

Other troubles that we encountered, with respective expedients are:

- Sometime the laser fails to shoot a pulse; a possible explanation is in that moment the two electrodes failed to generate the discharge.
- As depicted in Figure 3.3, we set the pulse laser so that it does not strike the surface perpendicularly. A perpendicular reflection can come back along the same path and interact with the incidence pulse.
- Specially at high energy and low volume, there was an evident splashing even outside the beaker. Many solutions was tried: first ones concerned a perforated parafilm which allowed to pass the laser beam; at the end was realised an apposite polymeric cap which does not interfere with laser. So even if the splashing happens, the liquid drips inside the beaker.
- For the previous mentioned decrease of laser energy, two times the energy can not be guaranteed at the set level. So we applied the hy-

pothesis of independence of the pulses at low repetition rate: because the process duration is hundreds of μs, if the sequent pulse arrives after $0,03$ s the interaction with the first will be completely finished. In few words, only the number of pulses counts. So a test at 15 Hz for 2 h and another at 10 Hz for 1 h were considered equivalent to tests at 30 Hz with time of 1 h and 20 min, respectively.

- We estimated the losses in energy due to mirror and lens, in addition to possible erroneous emission of laser. The losses due to reflection of water are not simple to estimate and probably quite small, so we will neglect them. The laser in exit is higher up to $2,5$ % than nominal value, lightly increasing with energy. After the mirror the pulses are ca. 5 % weaker than nominal value and after the lens ca. 28 %.

- We noted that the laser spot has not a spherical shape; exiting from the laser, it has rectangular shape with dimensions of $2,5$ cm horizontally and 1 cm vertically. After focusing of the lens, the spot becomes more roundish, but still maintains the disequality in dimensions, leading to an elliptical shape. Also little variations in horizontal and vertical dimensions happen, due to non exact 45^o inclination.

- Actually, spot area depends on laser energy: higher energies etch bigger spot in the target. In following dissertation we will refer preferentially a the real Energy-Area ratio (fluence) rather than at the nominal energy; respective conversions are reported in Table 3.1.

Energy (mJ)	**Area (mm^2)**	**Nominal fluence (J/cm^2)**	**Fluence with optical losses (J/cm^2)**
50	$0,697$	$7,17$	$5,16$
100	$0,856$	$11,68$	$8,41$
125	extrapolation	$13,36$	$9,62$
150	extrapolation	$14,78$	$10,64$
200	extrapolation	$17,04$	$12,27$

Table 3.1: Table of areas measured with optical microscope at various energies and values of Energy-Area ratio (the fluence) without and with considering the losses due to optical system.

3.2 Deposition of thin film on suitable substrates

Right after the ablation we perform the deposition of the suspension of nanoparticles in water, in order to analyse them on a solid substrate. A certain quantity of suspension is deposited on an apposite substrate and then dried in a little brass disk covered by a glass and connected with a vacuum pump. We choose to deposit the solution on three substrates: silicon, glass and titanium. Silicon substrate is suitable to observe the structures at Scanning Electron Microscope (SEM) and Atomic Force Microscope (AFM). Glass is used in Raman spectroscopy and to perform electrical measurements. Titanium substrate is useful to obtain Raman spectra, in particular to observe the eventual signals covered by glass. We have to bear in mind that deposition and drying strongly depend on the substrate nature, so we will not be surprising for eventual big differences among them. The typical liquid quantities deposited are 50 μL and 500 μL. The first is to see isolated nanoparticles, the second is to try depositing continuous films. Sometimes the solutions are so concentrated that 50 μL are too much; in these cases 25 μL of solution are dissolved in 1 mL of isopropyl alcohol and 50 μL of this mixture are deposited on substrate. The isopropyl alcohol evaporates very quickly, so the structures in solution have not the time to aggregate; it supplies a good way to see isolated structures. Depositions after a certain rest time are performed in order to study possible aging phenomena in solution.

3.3 A technique to investigate nanoparticles in solution: Dynamic Light Scattering

Dynamic Light Scattering (DLS) is an useful technique to evaluate the dimensions of nanoparticles when they are in a liquid suspension. It works very well with monodisperse nanoparticles, but with some more complex models it can give results also in polydisperse systems. A monochromatic polarized laser beam crosses a certain amount of solution. If the particles are small compared to the wavelength, when light hits them, it scatters in all directions (Rayleigh scattering). The scattering intensity fluctuates over time, because the particles in solutions are undergoing Brownian motion, so their distance changes constantly during time. The light is subjected to

constructive or destructive interference; information about the time scale of particles movement is contained inside this intensity fluctuation. The scattered light is then collected by a detector at a specific angle. Two signals revealed at short time delays, have a strong correlation because the particles have not the time to move much away from the initial state. As the time delays become longer, the correlation decays exponentially, meaning that, after a long time period, there is no correlation between the scattered intensities of the initial and final states. This exponential decay is the quantity related to the motion of the particles, specifically through the known diffusion coefficient of the solvent. To interpolate the decay, numerical methods are used, based on calculations of assumed distributions. If the sample is monodisperse the decay is simply a single exponential. In polydisperse cases, there is an overlapping of exponentials but, because the intensity depends on sixth power of radius, the signal of biggest particles tends to dominate the signal of smallest ones. We will use the CONTIN model, a method to analyse the autocorrelation function via an inverse Laplace transformation; it is ideal for polydisperse systems.

3.4 Microscopy techniques

3.4.1 Scanning Electron Microscope

As the name says, the Scanning Electron Microscope (SEM) is an instrument that allows us to see the morphology of a material, scanning its surface with an electron beam as a probe. It has a elevated resolution ($1 - 10\ nm$), a big depth of focus and a good 3D appearance. The primary electron beam, produced monochromatly by an electron gun (for thermoionic effect or for field emission), is focused by electromagnetic fields. Then it reaches the sample surface, and many interactions can happen. An important one is reflection of incident electrons, with intensity dependent on sample elements; a beam of back-scattered electron at high energy is generated. Another important interaction is the emission of secondary electrons, generated extracting valence electrons from material, up to a depth of $5 - 50\ nm$, but only the most superficial ones can escape. So the number of electrons is function of the exposition (and so of inclination) of the surface; the out-coming beam contains the desired information about sample morphology. The detector

system measures these beams therefore the topographical image can be rebuilt.

Additionally SEM can be equipped with Energy Dispersive X-ray spectrometer (EDX). In effect another possible interaction between incident electrons and material is the emission of X-ray. Collecting them, a compositional analysis can be performed, with possibility of mapping the surface. The interaction volume has a spherical shape with radius of $ca.\ 5\ \mu m$. The two main limitations of SEM are the vacuum environment operation, which can alter some kinds of sample, and the necessity that analysed material must be conductive, otherwise it charges itself and the charges interact with incoming electrons. However some methods to overcome these limits exist. For our experiment, we will use a Zeiss SUPRA 40 Field Emission Scanning Electron Microscope, equipped with Oxford Energy Dispersive X-ray Spectroscopy (EDXS).

3.4.2 Atomic Force Microscope

Another instrument to see the surface of a sample is Atomic Force Microscope (AFM). The probe is a cantilever ending with a thin tip; the tip scans the material surface, and it moves in agreement to physical interaction between tip atoms and surface atoms. Many modalities are possible: contact, where the movement corresponds to sample surface and the tip feels a repulsive force; intermittent contact; non-contact, with attractive force and oscillating movements. A laser beam irradiates the cantilever, so it is deviated by the vertical movements of the cantilever. The reflected beam is analysed by a photodetector and, knowing the mechanical parameters of cantilever, we can calculate the force. The vertical resolution is excellent, up to $0,1$ Å; instead the lateral resolution is limited by shape and curvature radius (typical 10 nm) of the tip. A great advantage, also respect to the SEM, is the absence of limitation on material types: all metals, semiconductors and insulators can be seen at AFM. However some drawbacks exist: the risk of damaging or altering a soft sample, working in contact mode; the air can create an humidity layer, but it can be avoided working in vacuum; some artefacts are possible if the asperities are sharper than tip or with cavities; thermal noises. Our Atomic Force Microscope is Thermomicroscope Autoprobe CP Research (now Brucker) in non-contact mode.

3.5 Raman spectrometer

The Raman effect is an inelastic scattering of the light interacting with phonons in material. If we irradiate a sample with a monochromatic electromagnetic beam, the reflected beam will be composed mainly by waves with same wavelength of incident one, but also some waves shifted in wavelength. Because direct photon-phonon coupling is weak, a three particle interaction happens via electron [9]. The photon excites an electron into a virtual level, creating an electron-hole pair. The electron-hole pair may change its energy due to electron-phonon interaction: a phonon is created or annihilated. At the end, the electron releases its energy and comes back to original state, but in this way the energy of the photon is higher (if a phonon was annihilated) or lower (if a phonon was created). The energies of phonons are the fingerprint of the element. A Raman spectroscopy apparatus is composed by a laser, the focusing optics, a filter or gratings and a CCD matrix. The detected light allows us to recognise the elements by means of confront with known spectra; moreover the spectra depend on crystalline structure, so also crystallographic information is contained inside Raman scattering. We will use a Renishaw InVia micro-Raman spectrometer, with Ar^+ laser emitting at $514,5\ nm$; the edge filter has a cut-off at 100 cm^{-1} or at 50 cm^{-1}.

Chapter 4

Results and Discussion

4.1 Maximization of ablated mass

In order to characterise the production process, we believe that a systematic analysis of ablation rate is essential. So we measure the mass of target before and after ablation, in order to know the ablated mass from their difference. The sensitivity of the weighing scale is $0,1\ mg$. However this difference may not exactly correspond to the mass in solution; especially after ablation, there are many errors affecting values:

- Due to splashing, part of liquid containing the produced nanostructures could come out the beaker in the form of drops. So there will be less liquid and less products than nominal ones.
- Ablated products could deposit on the bottom of the beaker. In this case the target was ablated, but the products are not present in final suspension.
- Ablated products could also redeposit on the target: for the weight measurement, they do not result as ablated mass, even if the ablation happened.
- Once, due to intense ablation, relatively large dark fragments were present in solution; maybe they are small parts of the target removed during ablation.
- We find some problems in measurements of target mass after ablation in aqueous solution of SDS. In particular, final mass is higher than

initial one. A possible reason is that the mass of ablated target was less than residual surfactant on target. So the ablation rates in SDS will be ignored.

Moreover some alterations of the quantity during deposition of liquid on substrates may happen. Due to boiling at low pressure inside vacuum disk, liquid droplets can splash outside the substrates. So the effective quantity of deposited material is smaller than nominal one.

The targets are obtained by sintering of respective oxide powder; so a residual porosity is inevitably present. When a target is immersed in water, it absorbs small quantity of water and retains it for a certain time. Our measurements of mass are influenced by this retained water. So in order to correctly estimate the ablated mass, we have to subtract the mass of water. We studied the drying of water in time starting from extraction of target. In a target mass-extraction time plot, the points arrange themselves along an exponential curve; so we modelled as in Figure 4.1 and in Equation 4.1.

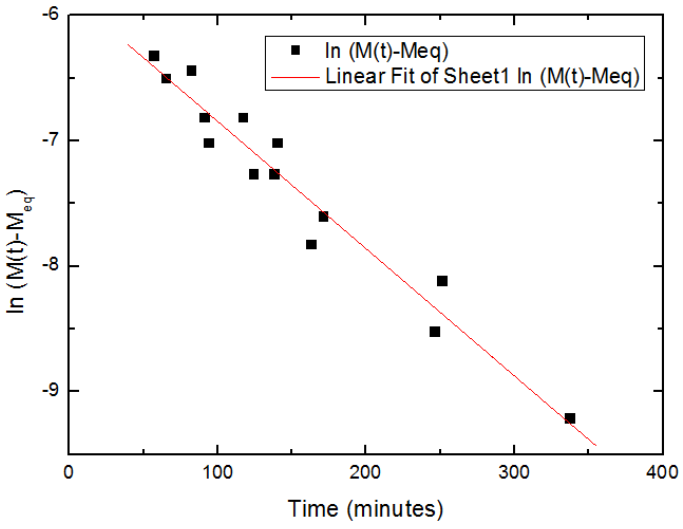

Equation	y = a + b*x		
		Value	Standard Err
ln (M(t)-Meq)	Intercept	-5,832	0,11421
ln (M(t)-Meq)	Slope	-0,0101	6,82618E-4

Figure 4.1: The plot of the extraction time and the logarithm of difference between mass at that time and equilibrium mass.

$$M(t) = M_{eq} + \Delta M \cdot \exp(-\lambda \cdot t) \tag{4.1}$$

Where the computed ΔM (the retained water at time extraction) is *ca.* $2,9\ mg$ and λ is $0,0101\ min^{-1}$. We also calculated the time to a complete drying of target (retained water less than sensibility of the scale): we found $7\ h$, too much time to wait for a complete drying. So we prefer to measure the mass after a shorter time and to use this model to subtract the estimated retained water.

In Figures 4.2, 4.3 and 4.4 we report the plot of ablated mass-ablation time, ablation rate-liquid thickness and ablation rate-fluence, respectively. All plots refer to ablation of AZO in distilled water; in each plot only the quantity reported in x axis is varied, the others are maintained constant.

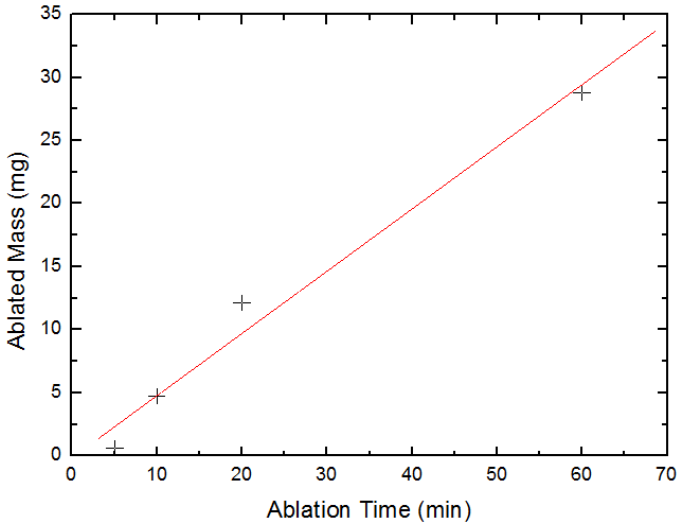

Equation	y = a + b*x		
		Value	Standard Err
Ablated Mas	Intercept	-0,1772	1,58067
Ablated Mas	Slope	0,49378	0,04922

Figure 4.2: Plot of the ablated mass of an AZO target in distilled water in function of the ablation time. Each point corresponds to a different experiment. Other conditions are: $6\ mL$ of distilled water, $150\ mJ$ of energy and $30\ Hz$ of repetition rate.

As intuition suggests, the ablated mass increases with time; the increase is quite linear (Figure 4.2), so we approximate it as a straight line:

$$M(mg) = 0,494(mg/min) \cdot t(min) - 0,177(mg) \tag{4.2}$$

This means that we have a production rate of nearly $0,5\ mg/min$. Comparing this value with others from literature, it is a very high value. Two considerations can be done. The first is about the intercept less than zero in Equation 4.2: it looks like than we have to wait a small time for starting the ablation. Maybe the time needs to reach the equilibrium inside the beaker: the water is splashed on the walls and on the coverage of beaker and then it drips inside the beaker. After a certain time it reaches a stable thickness (as we will see, it has a great influence), so the ablation rate is stabilized. Another possible explanation is given in [62], where a similar delay was observed. In their opinion, in first pulses the surface of the target was smooth, so it could reflect part of energy of the pulse. After a certain amount of pulses, estimated in a dozen, it becomes rougher, so it absorbs more energy. We can do another consideration, about the light decrease of ablation rate at long time. We can explain it considering that at higher time more material will be in suspension in liquid; so it can interact with laser pulses and attenuate the irradiation arriving on target.

In Figure 4.3 we can note how much is important the quantity of the liquid to obtain high ablated mass. In effect at *ca*. $9\ mm$ and *ca*. $5\ mm$ of thickness, the ablated mass is quite similar. Beneath $5\ mm$, the ablation rate increases rapidly, reaching a peak at *ca*. $1,5\ mm$. At lower thickness the ablation rate is minor; maybe at such thin thickness the liquid can not guarantee a complete coverage for all the experiment, and it may pass in a condition of ablation in air (similar to Pulsed Laser Deposition that has lower ablation rate). This can be connected to surface tension of water because we noted that below a certain volume is difficult to immerse completely the AZO target in water. We try modelling this dependence with two straight line:

$h > 3,5\ mm$

$$\dot{m}(\frac{mg}{h}) = -0,1\frac{mg}{h \cdot mm} \cdot (h(mm) - 3,56mm) + 2,13\frac{mg}{h} \tag{4.3}$$

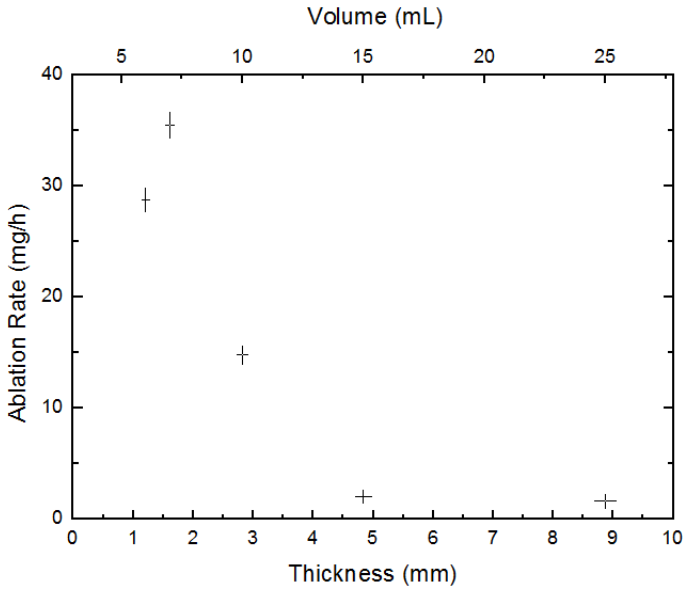

Figure 4.3: Plot of the ablation rate of an AZO target in distilled water in function of the thickness of the liquid. Other conditions are: 60 min of ablation time, 150 mJ of energy and 30 Hz of repetition rate.

$1,5\ mm < h < 3,5\ mm$

$$\dot{m}(\frac{mg}{h}) = -17,11\frac{mg}{h \cdot mm} \cdot (h(mm) - 3,56mm) + 2,13\frac{mg}{h} \tag{4.4}$$

Where h is the thickness of the liquid and $\dot{m}$ is the ablation rate.

At the end, the Figure 4.4 reports the ablation rate with the fluence of the laser pulse. In this case the dependence is controversial: it increases almost linearly up to *ca.* 10 J/cm^2 (150 mJ), then decreases. Basing on literature papers, we can attribute this variation in ablation rate to a change in mechanism [51]. At low-middle fluences, there is a linear ablation regime; at high fluences, it passes to a saturation regime, where the main ablation mechanism is the vaporization of target. We also tried an ablation at 20 mJ (with ZnO target), but in that case almost nothing was ablated and the target did not show an evident spot. Maybe at such low energy there is only a very weak interaction with the target; the experiment was not reported.

Our best ablation rate was $0,605\ mg/min$ ($0,0363\ g/h$). Only few papers report the ablation rate. Considering ZnO nanostructures production from

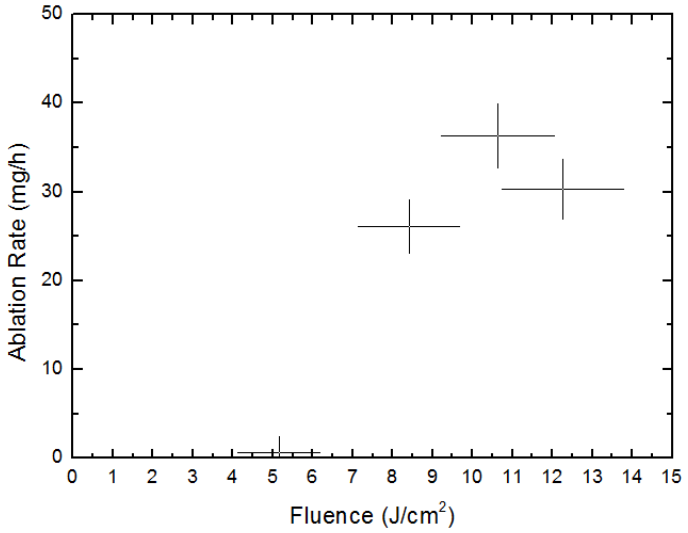

Figure 4.4: Plot of the ablation rate of an AZO target in distilled water in function of the laser fluence. Other conditions are: 20 min of ablation time, 6 mL of distilled water and 30 Hz of repetition rate.

Zn or ZnO target, papers have an ablation rate considerably lower than ours: in [35] it is $0,0001\ mg/min$ (at repetition rate of 10 Hz) and in [36] $0,02\ mg/min$ (1000 Hz). A paper about ablation of many alloys targets reports an ablation rate of our order of magnitude 1 mg/min, but with an enormous repetition rate of 500 000 Hz [63]. Only one, the [51] on Al_2O_3, reports a higher rate: optimizing a long set of parameters, they obtain 22 mg/min, at 4000 Hz. However with the hypothesis of independence of pulses, their ablation for each pulse is lower than in our experiment. For comparison, a high deposition rate obtainable with PLD technique is of the order of 10 nm/min, in an area of $ca.$ 1 cm^2. Transforming it in ablation rate, we obtain values of $0,01 - 0,001\ mg/min$, much less of our PLAL results. So a great enhancement in terms of ablation is observable in PLAL respect to PLD, mainly due to more extreme conditions of pressure and temperature for the confinement effect of liquid. In terms of deposition, PLAL has the disadvantage that it takes relatively long time to dry the liquid; however this process can be parallelized so many deposits can be dried simultaneously. Moreover other intrinsic differences are present: the PLAL obtains nanoparticles in solution, so a wide variety of processes are feasible; from solution, the deposition is more tunable, because we

can choose the area and the shape of deposit, and also cover non-plane substrate in uniform way.

Each laser pulse on target causes a certain emission of light and an acoustic sound. We note a remarkable difference of these during experiments: if the thickness is lower than *ca*. 3 mm the intensity of light is very high and the noise is strong. Also the target spots present difference in depth of ablation. As we can see in Figure 4.3, the ablation rate is very different below and above this thickness, as if a threshold existed. Almost independently on other parameters, all experiments can be arranged in one of these two regimes: low thickness with high ablation rate ($\sim mg/min$) and high thickness with low ablation rate ($\sim mg/h$). We note that the threshold value has dimension comparable with the typical radius of cavitation bubble (2 mm, see Section 2.2); so we suppose that thickness lower than this critical size can be the origin of the change of regime, and so the cause of the enhancement of production rate.

4.2 Analysis in solution: Dynamic Light Scattering

We would like to study the dimensions of products directly in solution, so we identify that Dynamic Light Scattering is a smart way to achieve our purpose. The measurements via Dynamic Light Scattering method were performed with the support of Professors Roberto Piazza and Stefano Buzzaccaro at Dipartimento di Chimica, Materiali e Ingegneria Chimica Giulia Natta. The criteria to choose the sample were the absence of suspension in solution visible to naked eye and the absence of sediments on the bottom of the test-tube. The sample which better fits these requests is the AZO ablated with energy of 150 mJ in 25 mL of distilled water for 60 min. We divide it in two test-tubes; one is left as ablated, to the other we add a certain quantity of SDS. In this way eventual phenomena of aging or aggregation are stopped by capping of surfactant molecules. With the hypothesis of a monolayer covering of spherical nanoparticles, one can demonstrate that the right quantity in volume of surfactant must exceed the CMC (equal to $0,0081\ M$) of a value equal to:

$$\%vol_{SDS} = 3 \cdot \frac{d}{R_{NP}}\ \%vol_{NP} \tag{4.5}$$

Where d is the length of the chain of SDS, $ca.$ 2 nm, and R_{NP} is the radius of nanoparticles, measured in the same units of d. Measuring the ablated mass in known volume, and knowing also the density of nanoparticles, we calculate the $\%vol_{NP}$. At the end we have to estimate the order of magnitude of nanospheres radius R_p; from AFM analyses, it could be from tens to an hundred of nm. We find that a SDS concentration of $0,01$ M satisfies this condition up to few nanometres of radius.

However, due to technical problems, the samples were analysed three weeks after ablation. After this period, both samples presented a certain amount of sediments on the bottom of test-tube, especially the one without SDS. This can due to the big size of particles or to their agglomeration in solution and sequent deposition.

Before measuring, we centrifuged the samples at 5000 rpm for 10 min in order to decant the dust or the eventual agglomerates in solution. We performed two measurements, the first was realized the same day of centrifugation and the second after a day of rest. The results of the same sample in two different days are similar; we choose to report the measurement after the day of rest, because it is cleaner due to further time to deposit the agglomerates and the dust on the bottom of test-tube. The results of sample without SDS show that only surfactant micellae are present in suspension. So all the produced nanostructures are deposited on the bottom of the test-tube. Summarizing, the reported data refer to sample with this history: ablation, addition of SDS to obtain a concentration of $0,01M$, three weeks of aging, centrifugation and a day of rest.

In Figure 4.5 we can see the correlation function $g_2(\tau) - 1$ versus the delay time in microseconds. The conditions of DLS experiment were inclination of 135^o to collect the light and a temperature of 30^oC. The points arrange themselves not as a simple exponential, meaning that the sample is not monodisperse. We can discern two bend-points, the first at low delay time (some microseconds) and the other at longer times (some hundreds of microseconds). To fit this bimodal curve, we use the CONTIN method, which permits a good approximation of data trend. Via the CONTIN method we are able to calculate the distribution of dimensions of particles.

In Figure 4.6 we report the dimensions distribution; we remind that the dimensions in DLS correspond to the diameter of nanostructures. There are two scales: the intensity of signal and the count of particles. In in-

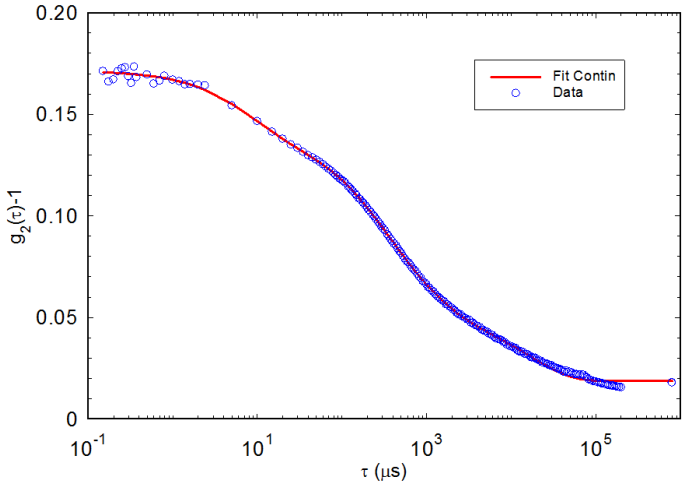

Figure 4.5: Plot of the correlation function versus the delay time in microseconds, obtained by DLS at $30^{o}C$ and 135^{o}. Blue circles represent experimental point, the red line the fitting via CONTIN method.

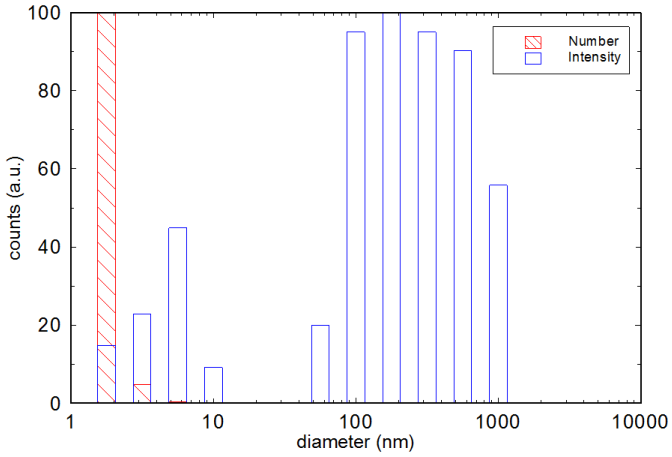

Figure 4.6: Population histogram obtained by CONTIN method: the intensity and the consequent number of particles in function of dimensions in nanometres.

tensity, a bimodal distribution is evident: particles of the order of some nanometres correspond to delay time of microseconds and particles of hundreds of nanometres in dimension correspond to delay time of hundreds of microseconds. Then we can transform the intensity into the number of particles generating the signal; because the intensity is proportional to the sixth power of radius, the number of low dimension particles is enormously higher than bigger ones to generate comparable intensity. So the greater part of particles in solution has small dimensions, with only few bigger particles.

However we can hypothesize that smaller distribution corresponds to micellae of SDS. If it corresponded to the products and the distribution at higher dimension to the aggregates, there would be a too large region without particles, making difficult explanation of agglomeration. Moreover we investigated also a sample without centrifugation: the correlation functions at small delay time are identical, so it corresponds to something that does not sediment. The surfactant micellae have exactly this characteristic. Our nanoparticles correspond to polydispersed distribution at higher diameters; they have dimension of *ca*. 200 *nm*, with range from 100 *nm* to 1000 *nm*. In conclusion, we have to pay attention to:

- Due to long aging time, we can not exclude that the distribution does not represent the as-ablated particles, but maybe the aggregates of particles.
- The values extrapolated via CONTIN method are not extremely accurate, because they strongly depend on many parameters of interpolation. So we can only have a general idea about dimensions and distribution of products.
- Actually, DLS method measures not the real diameter of particles, but the so-called Hydrodynamic Diameter [32], [51]. The Hydrodynamic Diameter is some tens of nanometres bigger than real one. In effect, in liquid other molecules, for example the solvent or the surfactant, are weakly bonded to nanoparticles. During scattering of light, they cause an alteration of duration of the correlation. In particular the delay time is longer, so the particles appear bigger.

4.3 Considerations about stability

From literature it is known that ablation in liquid of noble metals leads to very colourful solutions of nanoparticles in liquid. On the other hand ablation of semiconductors, since they do not absorb visible light, should lead to transparent or lightly white solution. In effect our as-ablated suspensions are completely transparent or whitish, depending on concentration of ablated material. In Figure 4.7 we report two indicative examples of AZO as-ablated suspensions. The Figure 4.7 (A) illustrates a typical sample with milky colour, probably due to high density of products in suspension. On the other hand, the Figure 4.7 (B) shows naked-eye visible particles in solution. Maybe in this case the evolution of products (assembly or agglomeration) started when the solution was still in ablation.

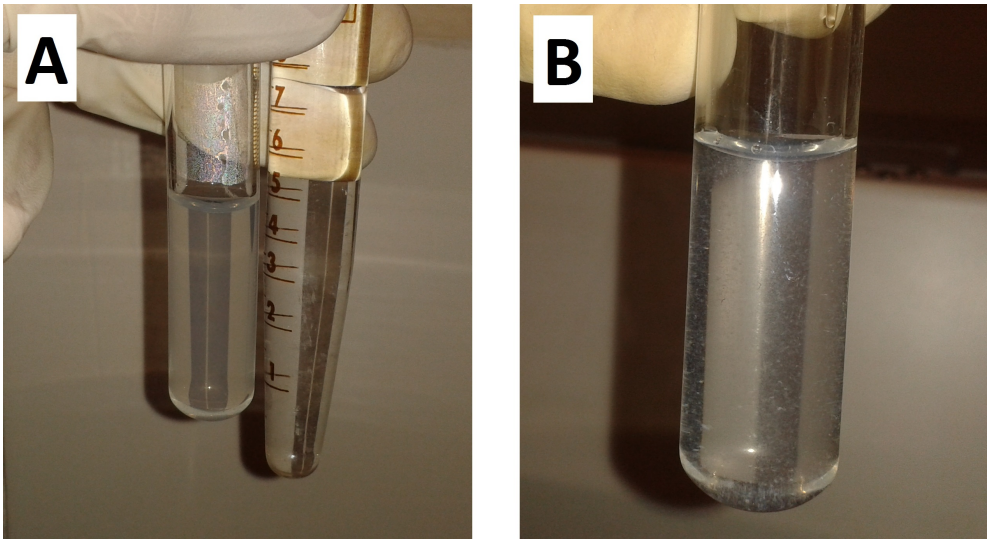

Figure 4.7: Two samples of as-ablated AZO in distilled water in conditions (A) 10 mL, 150 mJ, 60 min, 30 Hz, compared with distilled water and (B) 6 mL, 100 mJ, 20 min, 30 Hz.

After a certain time among some days to some weeks, the majority of samples sediments on the bottom of test-tube. The sedimentations are more rapid and more abundant when the concentration of the solution is higher. We can recognise a first step, when big pale particles form in suspension and a second step, when they deposit in the form of a woolly sediment. We can see two examples in Figure 4.8, where the (A), performed in a volume

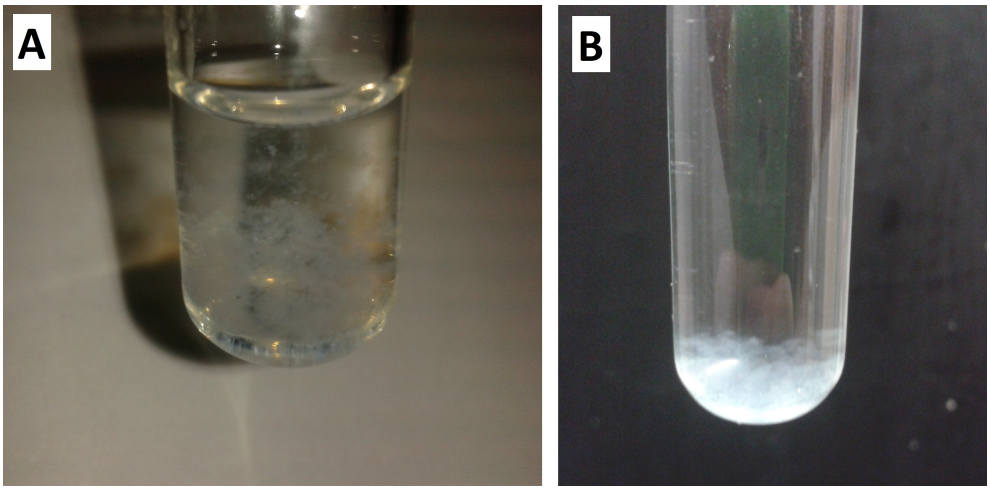

Figure 4.8: Two samples of AZO in distilled water in conditions 150 mJ, 60 min, 30 Hz and 10 mL (A) or 15 mL(B). Both suspensions are aged for 5 $months$.

of 10 mL, has a higher ablated mass and so it has more decanted sediments than the (B), ablated in a volume of 15 mL.

So far only one sample, ablated in 7 mL of distilled water, has presented an additional step: the milky sediment switch colour to yellow after some months of rest, as we can see in Figure 4.9. We will perform SEM and Raman analyses comparing the situation as-ablated with situation after changing colour, in order to understand if there are some modifications in properties of suspension.

In conclusion, we can say that suspensions are stable for at least some days; this phenomenon probably depends on charge of nanostructures. In effect in many technique to synthesize nanostructures, the products present a surface electrical charge. In PLAL we can hypothesize that it comes from an imperfect re-equilibration of charges after transformation from plasma state. So it needs some days to re-equilibrate the balance. After that, the neutral particles in suspension can collide and aggregate, and when they are sufficiently big (on the order of hundreds of nanometres) they can precipitate.

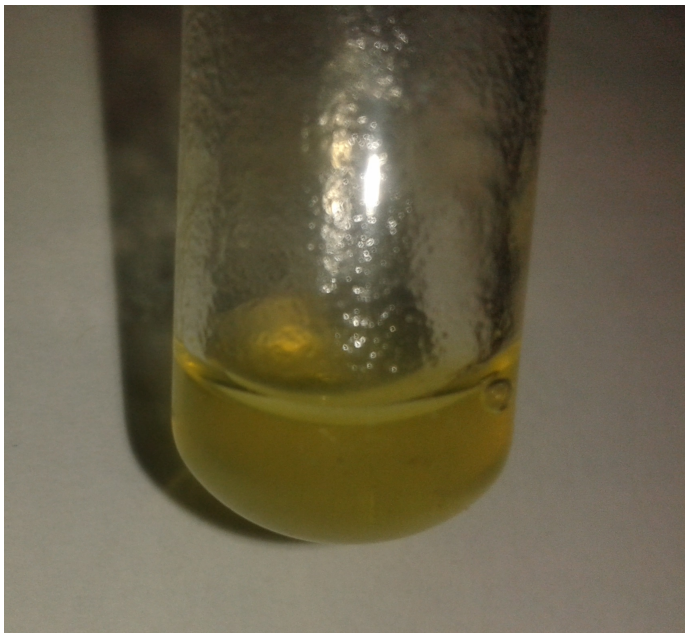

Figure 4.9: A sample of AZO in distilled water in conditions 7 mL, 150 mJ, 60 min, 30 Hz, after aging of 5 $months$.

4.4 Analysis after deposition: morphology and its dependence on ablation conditions

We study the morphology of deposits via SEM and AFM. We perform also some observations with optical microscope; an example is reported in Figure 4.10. Even if only 50 μL are deposited, the film appears very thick. However the thickness seems also variable: the evidences are the differences in colour, due to the interference of light, and the impossibility to focus every point of the area, because the finite depth of the field prevents to see simultaneously such different material heights.

4.4.1 The effect of ablation volume

In order to compare different morphologies in function of the ablation volume (directly proportional to liquid thickness), we analysed via SEM five samples of AZO ablated in distilled water with an energy of 150 mJ at repetition rate of 30 Hz for 60 min. The volumes were 6 mL, 7 mL, 10 mL, 15 mL and 25 mL; because all other parameters are identical, we will refer

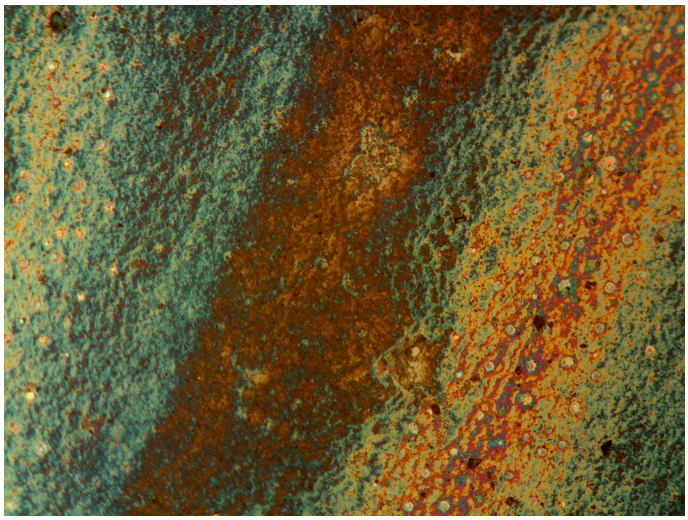

Figure 4.10: Optical acquisition of 50 μL deposit of suspension of AZO in distilled water, ablated in conditions of 10 mL volume, 150 mJ of energy, 60 min of ablation time and 30 Hz of repetition rate. The substrate is Si and the magnification is $32x$.

to them only with their ablation volume. For each one, we deposited 500 μL on a Si substrate.

The deposit of sample 6 mL forms a complete and thick film on the substrate. It presents some cracks and separations. The morphology of the film is a sort of wave-form structure (A in Figure 4.11), with many elongated ridges quite compact. There are also a lot of holes, similar to caves. Somewhere few little cubes are present. Observing another deposit with much less materials, only a partial film is grown; we note that it is formed by flattened lamellae. Maybe they are the constituent structures of compact film.

In the sample of 7 mL the film is thick and cracked as the previous one, but an evolution in morphology is present: the structures are sharper and the caves are bigger and deeper. So the structures appear as leaf-like intersecting layers, with net or smooth veins, as we can see in B of Figure 4.11. This intersecting layers morphology was reported also in [56], and it was attributed to $Zn(OH)_2$ layers via XRD diffractometry.

On the contrary, the main structures that compose the film at 10 mL are the small cubes, of dimension *ca*. 100 nm. Typical nanocubes are reported in C of Figure 4.11, where we can see that they are very good welded with

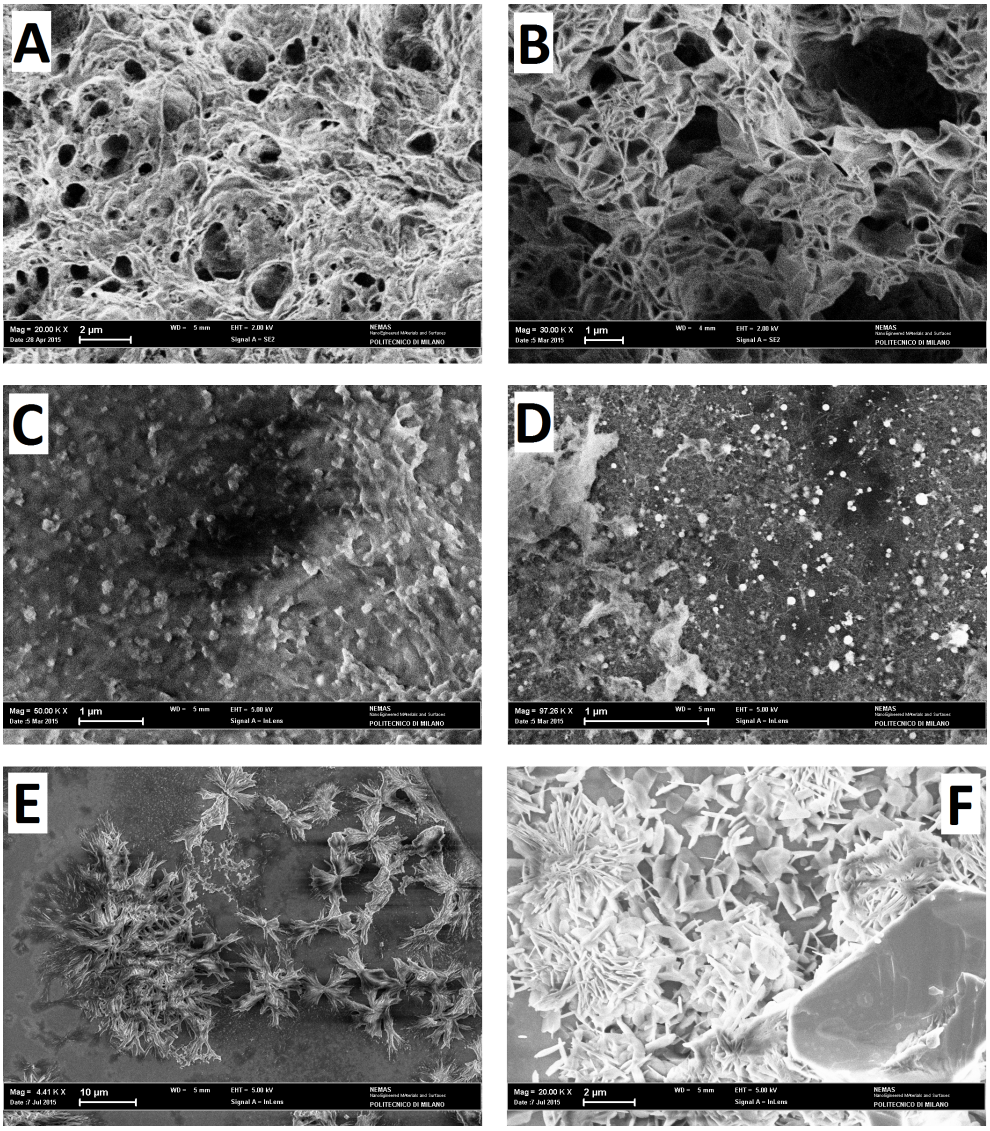

Figure 4.11: The SEM images of 500 μL of deposited solution, containing AZO ablated with an energy of 150 mJ at repetition rate of 30 Hz for 60 min in a volume of distilled water of 6 mL (A), 7 mL (B), 10 mL (C), 15 mL (D) and 25 mL (E, F).

underlying material; they cover the greatest part of substrate, except some small island where the predominant structure is intersecting layers type.

The sample at 15 mL (D in Figure 4.11) presents a more jagged structure: there are spherical nanoparticles, veins and compact parts. The nanospheres have a diameters from 20 nm to 100 nm. The background is compact as in 10 mL.

In 25 mL sample there are two different structures. In E of Figure 4.11 3D reliefs seem corals or flakes. They are dark (at electron microscope) and they branch off from a centre; they look like composed by irregular rods long some micrometres. The other typology is sharp straight needles (some micrometres in length and a hundred of nanometres in width), that sometimes are enlarged up to disks. They are white, so emit more electrons than coral structures. Their assembly is very dense and radially arranged. In general all samples can be easily seen at SEM, specially in comparison with the deposit of ablation of ZnO target, which are not reported due to difficulty to visualize it. This means that the effect of Aluminium in conductivity is maintained also after ablation. The complexity increases with ablation volume: from well welded ridges or layers to more defined structures, as nanocubes, nanospheres or nanoneedles. Moreover at low ablation volume, the structures appear more porous (greater surface area) and watery.

4.4.2 The effect of laser energy

Then we performed test varying energy at 50 mJ, 100 mJ, 125 mJ, 150 mJ and 200 mJ. The other fixed parameters are AZO target, 6 mL of distilled water, repetition rate of 30 Hz and a duration of 20 min. Images are reported in Figure 4.12.

The first test of 50 mJ sample is not so clear, maybe due to low quantity of material or to a low conductivity. There is a background composed sometimes by squared nanoparticles of few tens of nanometres in side, but more frequently by irregular agglomerates with many holes. From this background, discoid particles of 2 μm in diameter appear, as visible in (A of Figure 4.12).

The sequent sample, at 100 mJ, allows good images for resolution and contrast. It can be due to a higher conductivity. The covering of substrate is complete; at low magnification, it looks like waves or vortices. At higher

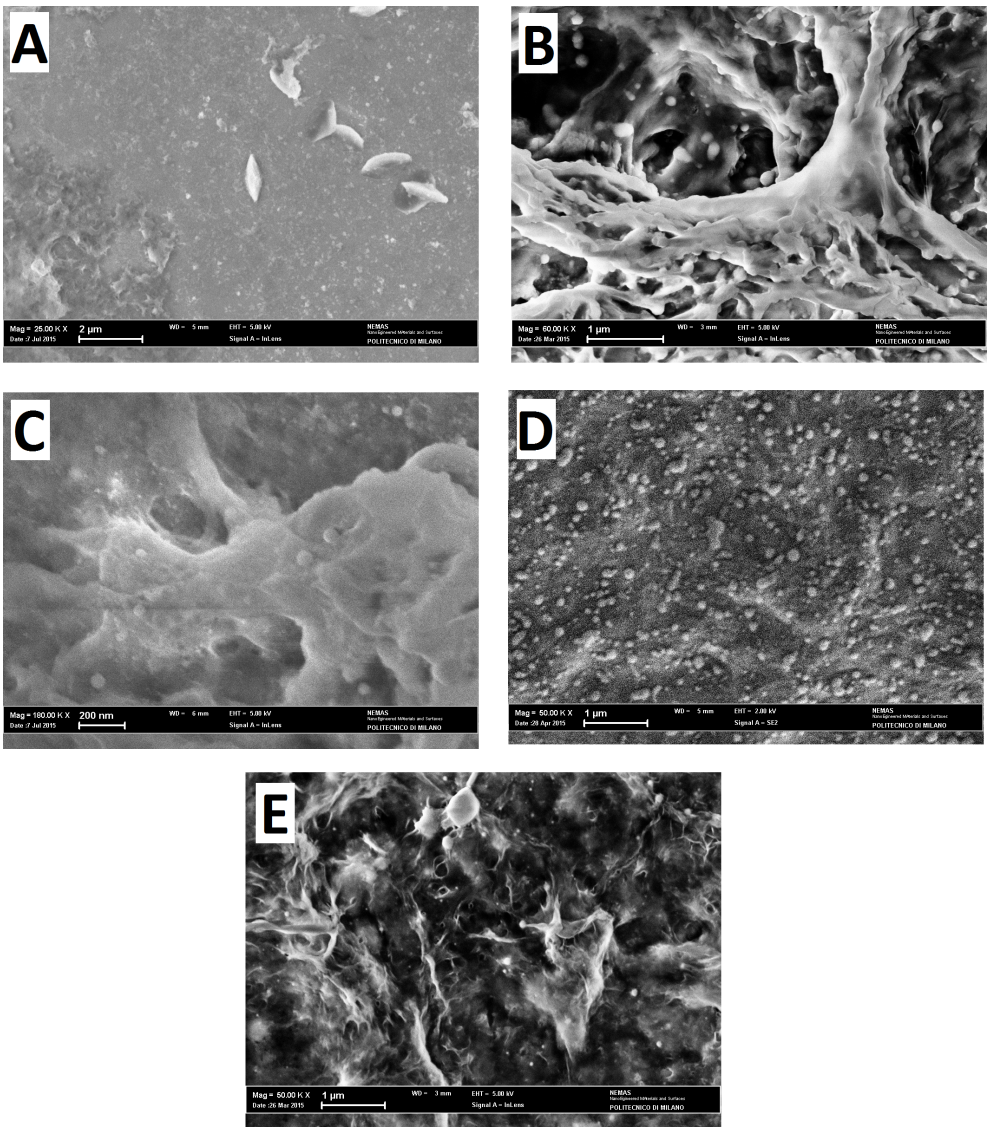

Figure 4.12: The SEM images of 500 μL of deposited solution, containing AZO ablated in 6 mL of distilled water at repetition rate of 30 Hz for 20 min at energy of 50 mJ (A), 100 mJ (B), 125 mJ (C), 150 mJ (D) and 200 mJ (E).

magnification, a branched-like structure is visible (Figure 4.12, B), with inclusions of nanospheres. The nanospheres are 100 nm in diameter or a little less. In general it appears compact below surface and porous externally.

At 125 mJ, none characteristic structure is recognisable. It appears as a compact and shapeless deposit (Figure 4.12, C), with some inclusions of quite spherical nanoparticles. Maybe these nanoparticles are the constituent elements of shapeless agglomerates; their dimensions range from 20 nm to 200 nm.

Also for 150 mJ is very difficult identifying sharp structures; as 125 mJ, it appears as an indistinct background, with many round particles well welded (Figure 4.12, D), with diameter of an hundred of nanometres.

In 200 mJ deposit, we note pointed structures, with many veins and holes (Figure 4.12, E). At lower deposited liquid (50 μL), we see the step before the thick film: there are not aggregates, but only nanoparticles, which can be big spherical or small fragmented.

In its entirety, structures appear more defined at higher energy. A possible explanation is that low energies lead to amorphous structures, whereas high energies to more crystalline ones, with mechanism explained in Section 2.3.

4.4.3 The effect of ablation time

In Figure 4.13 (A) we can see the deposit of AZO with conditions of 6 mL of distilled water, energy of 150 mJ, repetition rate of 30 Hz and ablation time of 5 min. The coverage is high, despite the time is brief; however visualization is quite difficult due to charge effect. The deposit is composed by horizontal slivers (or leaflet) of various dimensions and by other smaller fragments.

The Figure 4.13 (B) has the same conditions, but 10 min of ablation. It presents a variety of different structures: masses, veins, spheroidal particles and flat slivers. The slivers are similar to those in 5 mi ablation, but in this case they weld themselves along more direction, looking similar to desert rose.

Other tests at longer times are the 20 min ablation time reported in (D) of Figure 4.12 and 60 min in (A) of Figure 4.11. Even if the time is the only changing parameter, the deposits appear quite different each

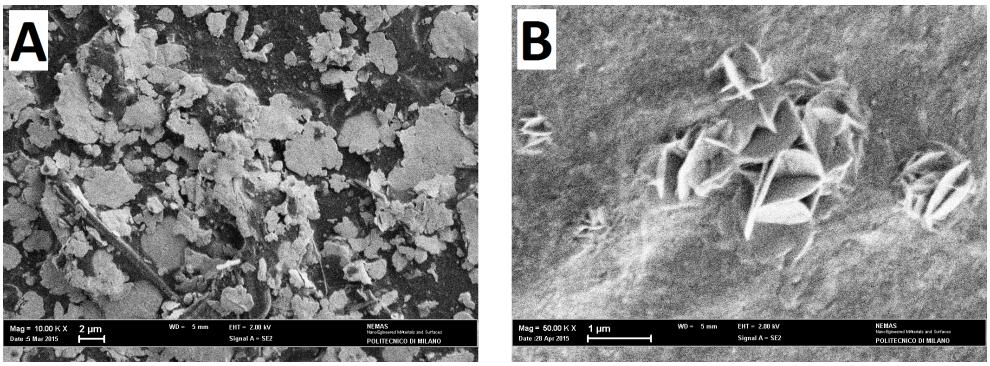

Figure 4.13: The SEM images of AZO ablated in 6 mL of distilled water at energy of 150 mJ and repetition rate of 30 Hz for an ablation time of (A) 5 min (50 μL deposited) and (B) 10 min (500 μL deposited).

other. However a tendency in forming layers at low time is present (5 min and 10 min). Moreover from 10 min there is the appearance of shapeless amasses that become predominant at longer times. A certain amount of small particles is always present. We think that this evolutions can be ascribed to a modification on the already ablated products by laser pulses or to some differences in deposition or drying maybe due to different concentrations of solutions.

4.4.4 Other remarkable effects

Unfortunately, the sample ablated in SDS solutions are very difficult to see, due to significant presence of insulator SDS in deposit. Only one sample is reported in (A) of Figure 4.14, at concentration of $0,005$ M. Also at this concentration, a thick underlying layer of SDS is visible. From this layer some particles protrude; they are clearly visible thanks to their sharp border. The shape is spherical, lightly elongated in some cases and the dimensions are $100 - 200$ nm or less. We think that the so sharp borders of nanoparticles are caused by adsorbed surfactant on their surface. This prevents also agglomeration of particles.

We analysed also a sample of AZO after long aging in solution (5 $months$), reported in (B) of Figure 4.14; the as-ablated deposit is in (B) of Figure 4.11. The structure is completely changed: now is present a very compact background with some layers emerging. Moreover, some big particles are

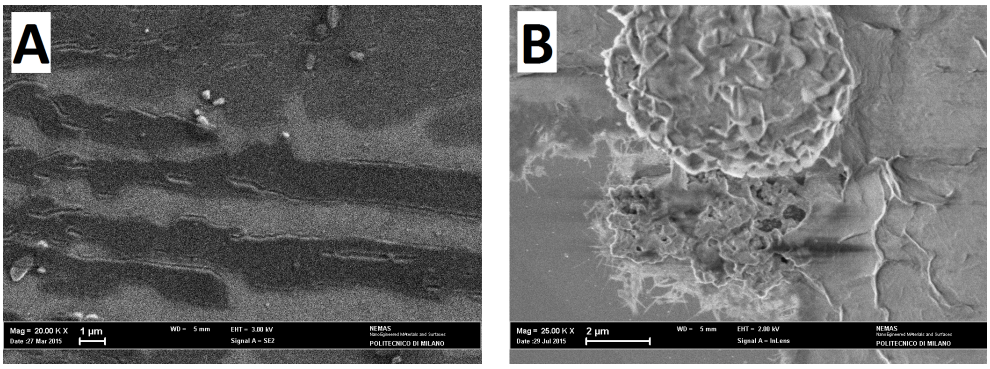

Figure 4.14: The SEM images of: (A) 50 μL deposit of AZO ablated in 15 mL of aqueous solution of SDS $0,005$ M at energy of 100 mJ for 20 min and (B) 500 μL deposit of AZO ablated in 7 mL of distilled water at energy of 150 mJ for 60 min, after 5 $months$ of aging; both samples have repetition rate of 30 Hz.

apparently laid on surface: maybe they are assembled in solution and during deposition they lay on substrate. We can correlate this compactness with the loss of charges after some days in suspension: when the deposit is grown right after ablation, the particles are charged and tend to repulse themselves, leading to a more porous structure (for example, coral-like). After aging, the charges disappear and particles can grow in a more compact way. So we can tune the properties of deposited film changing the aging time.

In general the morphology is very sensitive to ablation conditions. Moreover some modifications can be induced by deposition and drying. Lastly, also the electron beam of SEM can alter the deposit due to charging or interaction with electrons.

4.4.5 The cross sections of the films

We saw the deposits also in cross section, selecting the deposits which seemed thickest.

In Figure 4.15 (A) is present the deposit obtained from sample in condition 150 mJ, 20 min and 6 mL. The deposit appears as a continuous film, quite compact and with snow-like aspect. It presents also few small elongated cavities. The thickness is constant at high magnification, but presents higher variability at low magnification: we reveal thickness from 193 nm to

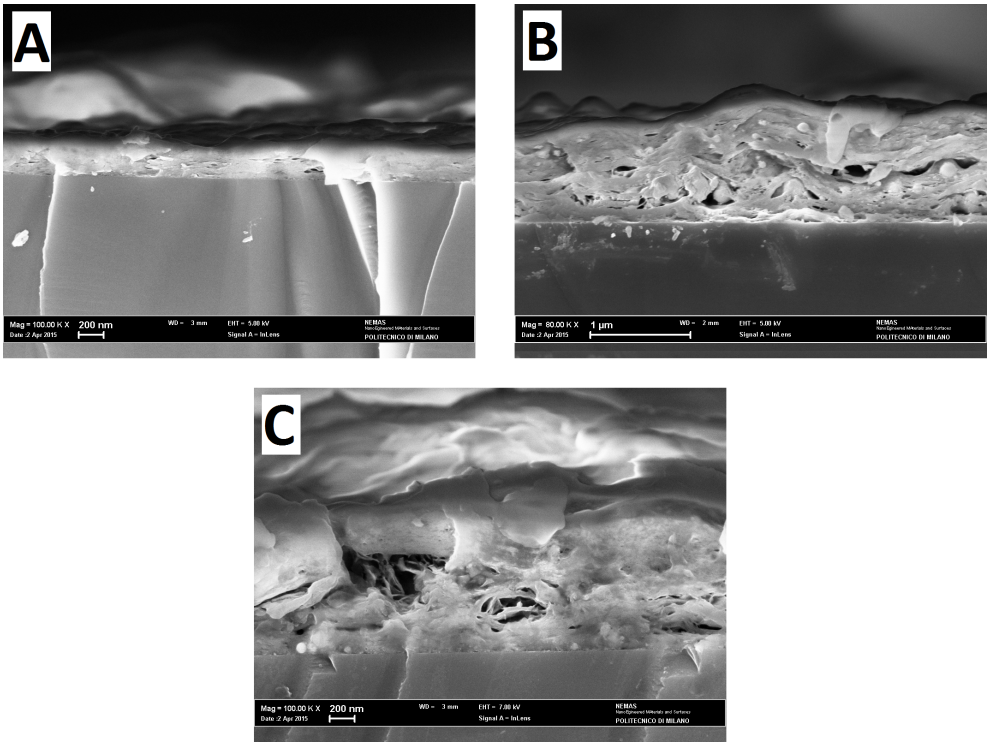

Figure 4.15: The SEM images in cross section of deposits obtained by 500 μL of solution of AZO ablated in following conditions: (A) 6 mL of distilled water at energy of 150 mJ for 20 min, (B) 10 mL of distilled water at energy of 150 mJ for 60 min and (C) 6 mL of distilled water at energy of 200 mJ for 20 min. All samples have repetition rate of 30 Hz.

309 nm, with an average of 260 nm. However in these measurements errors are unavoidable, due to difficulty in distinguish where film section ends and where background starts. On the background some higher mountains are present, maybe formed for inhomogeneous drying or maybe they were big particles formed inside the liquid and deposited on substrate.

The cross section reported in (B) of Figure 4.15 was obtained by a sample with triple ablation time, so it has about triple thickness. It ranges from 764 nm to 1072 nm, with an average of 950 nm. Its morphology is striated (due to drying effects), with inclusions of nanoparticles and also with some cavities.

The last image (C) of Figure 4.15 is the deposit of sample at 200 mJ. Also this one is quite thick, with an average thickness of 970 nm. The holes increase from previous ones, becoming as caves.

4.4.6 The hypothetical structural evolution

In order to study the evolution of structures, other samples were analysed varying the deposited quantity. When only few solution is deposited, isolated structures are the most frequent morphology. In (A) of Figure 4.16 we clearly see nanorods of length *ca*. 200 nm and width *ca*. 60 nm. These nanorods recall the hexagonal wurtzitic structure of ZnO (as well as AZO) because they are a direct consequence of the preferential growth along the main axis respect to radial assembly. Zooming in (B) of Figure 4.16, these nanorods appear to have more material in edges than in the centre. If it is not an artefact due to SEM, this would mean that nanorods are hollow. Generation of hollow nanostructures is a common phenomenon in PLAL (see Section 2.4) [40], [57], [64], [65]. In these two images, two or more nanorods seem to join together in a perfect welding. So aggregation of nanorods as building blocks can generate the other structures reported in (C) and (D) of Figure 4.16. In effect the dendritic assemblies seem to be formed by coalescence of elongated structures, as visible in (C) in conditions of enhancing concentration. Further growth can lead to coral assemblies (D). Here the majority of substrate is covered by these coral-like assemblies with large surface area. In general this mechanism of growth can be valid for high volume ablations; when the volume is lower, we saw that were present other basic structures, i.e. nanoparticles and nanolayers. In the same way, they can assemble as building blocks to form more or less

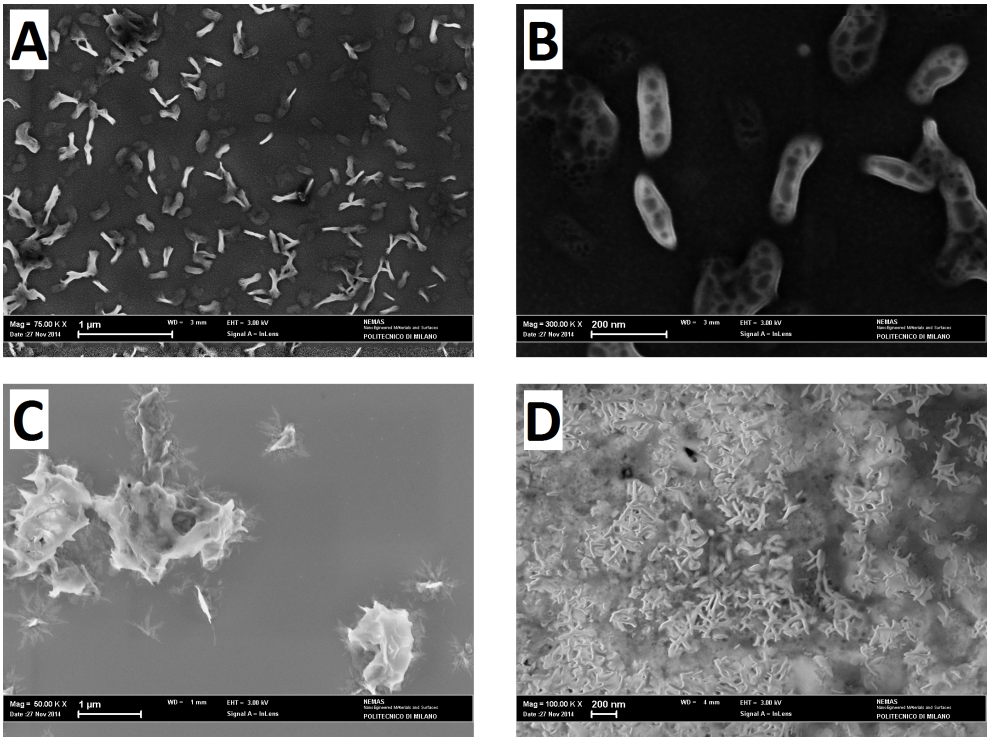

Figure 4.16: The SEM images of deposited solution of AZO ablated in distilled water at energy of 150 mJ, showing (A) nanorods, (B) apparently hollow nanorods, (C) dendritic structures and (D) coralline self-assembly.

compact films or nanoflowers (B in Figure 4.13), respectively.

4.4.7 AFM microscopy and distributions of dimensions

We performed also many measurements with Atomic Force Microscope, for the purposes of obtaining precise dimensions distributions and comparing with DLS and SEM values. To analyse the AFM images, we use the software Gwyddion 2.41. Three examples of results are observable in Figure 4.17. For (A) and (B) the distributions are wide and quite regular; the order of magnitude of the mean radius is from one hundred to two hundreds of nanometres. We note that overall they are a bit bigger than dimensions of nanoparticles seen in SEM images, whose valour was between 20 nm and 200 nm. Maybe this difference can be explained through the difficulty of revealing too small particle with AFM, because they are indistinguishable from background in presence of bigger particles. In order to compare with DLS, we have to consider the samples reported in (C) of Figure 4.17, which has more similar conditions (aqueous solution of SDS, ablation time, energy), with only a difference in volume (15 mL instead of 25 mL). In AFM the radius is $ca.$ 50 nm with a non homogeneous distribution from 20 nm to 120 nm; in DLS were estimated a diameter of 200 nm and a distribution from 100 nm to 1000 nm. The dimensions are lightly different. Two motivations can be given to explain it: the overestimation of dimension with DLS due hydrodynamical diameter (as stated in 4.2) and a possible aggregation happening during three weeks of aging in DLS. According to this last interpretation, the DLS population at 100 nm of diameter is the original one. Then they can aggregate in bigger particles up to 1000 nm, but at such high dimensions they unavoidably precipitate, leaving only few particles in suspension. So SDS concentration higher than CMC leads to much smaller radii: from an average of $100 - 200$ nm to $ca.$ 50 nm. Also the distribution is less wide respect to absence or low concentration of SDS.

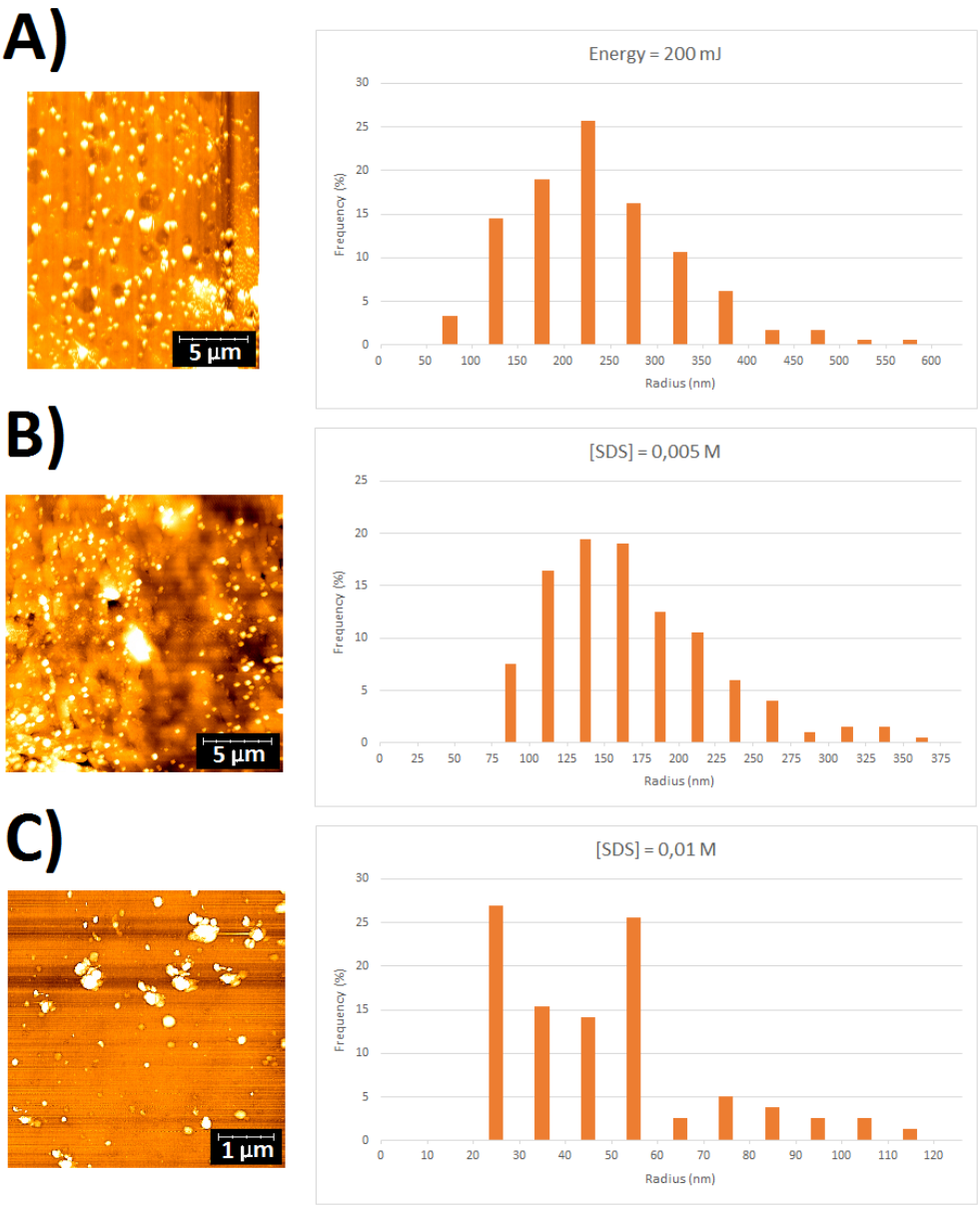

Figure 4.17: Three AFM images with respective distributions of radii at different conditions: (A) via isopropanol deposit of solution of AZO ablated in 6 mL of distilled water at energy of 200 mJ for 20 min; (B) 50 μL deposit of aqueous solution of SDS $0,005$ M ablated in 15 mL of distilled water at energy of 100 mJ for 20 min; (C) rinsed 50 μL deposit of aqueous solution of SDS $0,01$ M ablated in 15 mL of distilled water at energy of 100 mJ for 20 min.

4.5 Structural and compositional analyses

Now we want to identify which species are present after ablation and their percentage, and obtaining information about their crystal structure and bonds. We use Raman spectroscope and the EDX equipped in SEM. For Raman spectroscopy we deposit AZO or TiO_2 solution on glass or Ti substrate. For first analyses we use a green laser with wavelength of $514,5\ nm$ (Ar^+ laser) and a power of $7\ mW$; the investigation range is from the cut-off (here $50\ cm^{-1}$) to $2000\ cm^{-1}$ in extended acquisition modality and magnification $50x$. As reference, the spectrum of AZO target is shown in Figure 4.18.

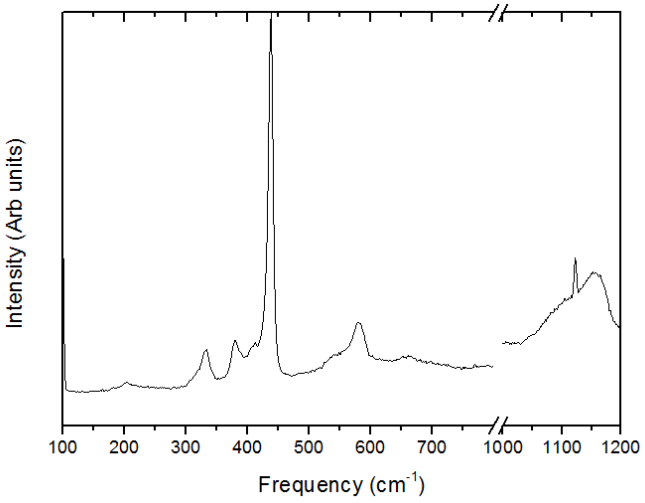

Figure 4.18: Raman spectrum of AZO target.

We encounter some difficulties in selection of suitable point of deposit on glass substrate. The film displays as in Figure 4.19: many white and bright islands in a dark background. The islands appear above-ground and formed by agglomerated material. To acquire sufficiently intense Raman spectra, we have to point to these islands. Maybe this is a characteristic due to drying of solution on glass substrate.

In some samples we detect photoluminescence in spectrum, easily recognisable by the increase in signal at high frequency in form of a Gaussian tail. In these cases, we subtract a straight line interpolated in interval $200 - 700\ cm^{-1}$, because it is the most interesting for us. Moreover when the substrate bands appear in the spectrum, we subtract them to

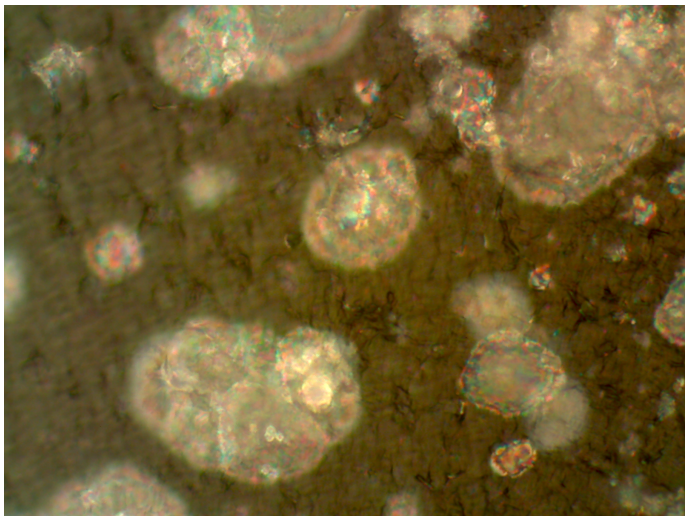

Figure 4.19: Image at optical microscope of film obtained drying on glass 500 μL of suspension of AZO ablated in 10 mL of distilled water with fluence of $10,6\ J/cm^2$ for 60 min at 30 Hz of repetition rate. The magnification is $100x$.

signal, in order to have a clean spectrum of deposited material; this is the case of glass substrate with thin film deposited on. A typical spectrum is reported in Figure 4.20.

Here two main peaks and other lower are clearly distinguishable:

- When the cut-off is 100 cm^{-1}, a rise to this direction; where it is 50 cm^{-1}, it appears as a whole peak, not caused by elastic scattering of light. We can identify it as the E_2^{low} peak, at 99 cm^{-1} of ZnO (or even AZO) wurtzitic structure.

- Small peaks above 400 cm^{-1}, which can correspond to other ZnO peaks $E_1(TO)$ and E_2^{high}, at 407 cm^{-1} and 437 cm^{-1} respectively.

- The highest peak at $1054,4\ cm^{-1}$, very sharp.

The peaks attributable to AZO are incomplete in number and not in the expected ratio of intensity. This can suggest that AZO could be completely in amorphous state or in a not clean condition which can suppress the missing peaks. Moreover we can not exclude that the partial appearance of AZO typical peaks could be due to the presence of other structures, for example hydroxides $Zn(OH)_2$ and $Al(OH)_3$. The peak not attributable to

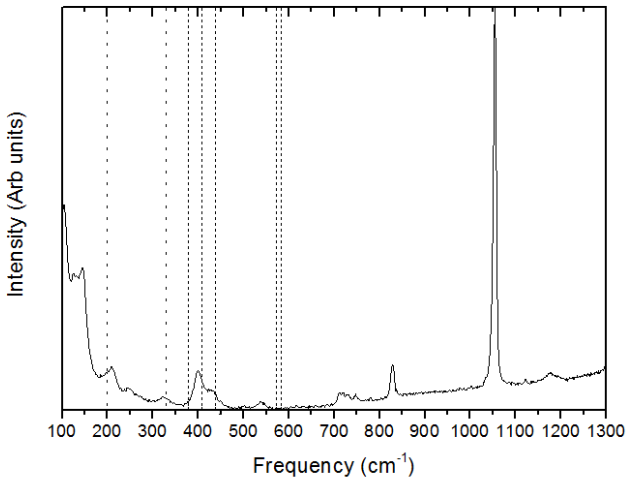

Figure 4.20: Raman spectrum of 500 μL deposit of AZO ablated in 10 mL of distilled water at fluence of $10,6\ J/cm^2$ for 60 min. Bulk values for primary and secondary peak positions are indicated with dotted lines.

AZO is present in all samples which have sufficiently thick deposit to make visible some Raman signals different from substrate. Calculating them, they are centred in $1053 - 1055\ cm^{-1}$ and they always are the highest and very sharp. For this peak we can formulate some hypotheses:

- A such sharp peak, in contrast with all other broad peaks, could be related to a vibrational mode of a molecule, which have the peculiarity of being very sharp. In particular, the adsorption of NO_2 by ZnO was explained in Subsection 1.1.4 and the spectrum was reported in Figure 1.5. An evident peak was present at $1055\ cm^{-1}$ and ascribed to O-N-O symmetric stretch. Also smaller peaks in the range $1300 - 1500\ cm^{-1}$ should have a correspondence: the N-O asymmetric stretches.

- An origin from nanocrystallites of ZnO embedded in an amorphous matrix, which generate a band exactly in this spectral region, as stated in Section 1.2 and Figure 1.6. However the width of that peak is broader than ours.

- A combination of modes of ZnO due to multi-phonon effects. In our case, it can be the combination of A_1 and E_2, which leads to a peak in the range $1050 - 1070\ cm^{-1}$ [66].

Moreover we have to be careful when doing Raman spectroscopy: for example the risk that during laser irradiation the film could heat up or could be subject to modifications due to laser energy. The deposits on titanium substrate show a peak on the right of E_2^{low}, recalling the peak at 144 cm^{-1} of TiO_2 and so a possible oxidation of substrate. However once it was seen also in deposit on glass, making this interpretation more improbable.

We use EDX spectroscopy to detect the eventual presence of N in the films. Results of a selected sample are reported in Figure 4.21 and in Table 4.1, where there are atomic percentages of elements in five areas in order to have a significant statistic.

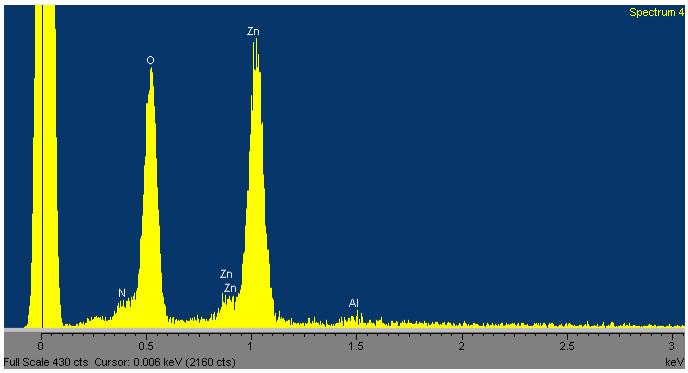

Figure 4.21: EDX spectrum of 500 μL deposit of AZO ablated in 6 mL of distilled water at fluence of 10,6 J/cm^2 for 60 min.

Element and electron shell	**Area 1**	**Area 2**	**Area 3**	**Area 4**	**Area 5**
C K					4,39
N K	8,60	5,85	6,69	8,69	8,17
O K	65,93	66,60	66,69	66,30	62,72
Al K	0,00	0,00	0,51	0,55	0,51
Zn K	25,47	27,55	26,11	24,46	24,20

Table 4.1: Table of atomic percentages of elements measured via EDX in 500 μL deposit of AZO ablated in 6 mL of distilled water at fluence of 10,6 J/cm^2 for 60 min.

Five species are identified: carbon, nitrogen, oxygen, aluminium and zinc. Silicon of substrate is not recorded by instrument, so the thickness of sample should be higher than interaction length, $ca.\ 1\ \mu m$. Carbon is a typical contaminant of samples in EDX, coming from environment. Nitrogen is present, with variable percentages from 6 $\%_{at}$ to 9 $\%_{at}$, in all areas scanned; so we can state that the correct justification of $1053 - 1055\ cm^{-1}$ peak in Raman spectra is NO_2 adsorption. Aluminium is detected in three areas on five, in a percentage little more of $0,5\ \%_{at}$. This is about a third of nominal value; also removing the contribution of NO_2, it is still half of nominal value. The value of the zinc ranges from 24 $\%_{at}$ to 27 $\%_{at}$. Oxygen has a percentage higher than nominal and it is very constant value for each measured area; it can not be explained only with excess of O due to NO_2. Probably there is another source for O, for example:

- O_2 adsorbed from air, in a quantity proportional to surface area (and so to porosity) of deposits.
- An higher number of O bonded to Zn, as in hydroxide $Zn(OH)_2$ or in peroxide ZnO_2.
- Residual molecules of H_2O present in deposit.

Using EDX as mapping, we made also an interesting observation. Whenever a whole and quite large area is scanned, the atomic percentages are similar to Table 4.1, in terms of excess of O and sub-stoichiometry of Zn and Al. Instead focusing on specific structure, as big nanospheres, the stoichiometry resembles the nominal one of target. The oxygen is present between 51 $\%_{at}$ and 55 $\%_{at}$, the zinc $43 - 47\ \%_{at}$ and the aluminium $ca.\ 2,0\ \%_{at}$; the nitrogen is absent. This can be explained in agreement with previous hypotheses in these ways:

- O_2 from air is highly adsorbed in all deposit, except in nanospheres which could have less porosity.
- Eventual $Zn(OH)_2$ or ZnO_2 could be widespread on the area of the film. In effect removing the contribution of O in NO_2, the ratio between oxygen and zinc varies from 1,9 to 2 on large areas. On the other hand on nanoparticles the ratio is little more than 1, with a composition very similar to starting AZO target; also aluminium increases its percentage from 1 $\%_{at}$ to 2 $\%_{at}$.

We think that, due to very constant O/Zn ratio of 2, the second option is the most plausible: many stoichiometric AZO particles embedded in a film of $Zn(OH)_2$. However investigations more in details were prevented by the lateral resolution of instrument, limited by interaction volume of X-ray with film.

So the detection of N via EDX implicates the formation and the adsorption of NO_2. This is not completely new in PLAL, because also in [67] presence of NO_2 and NO_3 was detected. Here a suspension of Pd powder in water was irradiated with a Nd:YAG laser focused exactly at the interface air/water. The plume of PLAL is thus composed by three species: Pd powder target, water and air. The via-XPS identified products were PdO_2 nanoparticles and nitrogen oxides NO_2 and NO_3. In the same conditions, but in Ar atmosphere, the products were Pd nanoparticles, without oxidation nor adsorption; so the nitrogen comes from air and not from other sources, such as some salts dissolved in water. In our case, a similar phenomenon could occur. The air can enter in our process during:

- The formation of the plume: when the thickness of the liquid is comparable with the radius of the cavitation bubble, the overhead air may be included inside the plume. In plasma state, the nitrogen could recombine with oxygen of air or water and lead to formation of NO_2.
- The interaction of laser pulses with the already ablated nanoparticles in solution, in a similar way to [67]. In particular the closest to surface air/water could be involved in adsorption.

Further EDX analyses on samples with high thickness of water (up to 1 cm) show that N is present here too. So it is difficult that air is involved in such deep plume mechanism, making more plausible the second hypothesis. Of course high ablation rate and relatively low liquid volume increase the concentration of products, making the NO_2 formation and adsorption more significant.

We are interested also in the results for the samples of highly aged AZO which changed colour. It did not show any particular variation in composition via EDX respect to as-ablated deposit; however the Raman

spectrum has a very intense signal of photoluminescence. This overcomes the NO_2 peak that was predominant before aging. So we think that the aging can increase the photoluminescence of samples.

4.6 Annealing of AZO films

As seen in Subsection 1.1.4, the NO_2 is completely removed at temperature higher of 700 K [11], [12]. We want to obtain a pure deposit of AZO, hence we perform an annealing treatment. We submit all the samples to annealing in a muffle furnace at 450^oC for 2 *hours*, so we are sure that all NO_2 will be desorbed. The thermal heat treatment is composed by heating from room temperature to 450^oC with a rate of $4^oC/min$; then a maintenance for 2 *hours*; at the end the cooling for heat dispersion with external ambient. The thermal history is reported in Figure 4.22. We select the samples deposited on glass substrates to acquire the new Raman spectra, and on *Si* substrates to note eventual changes in morphology at SEM or changes in composition at EDX.

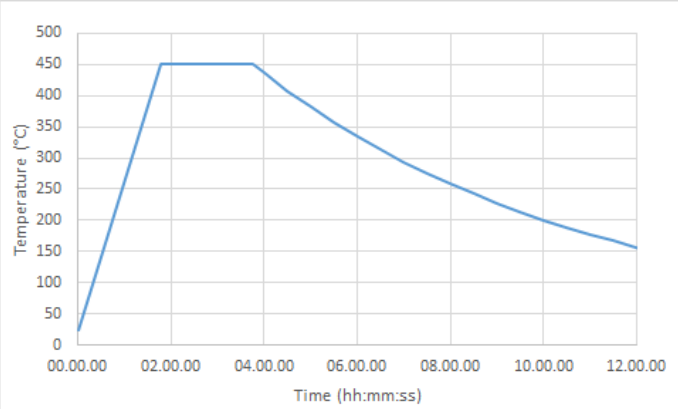

Figure 4.22: The temperature-time plot of the annealing treatment, which the deposits have been subject to.

We must pay attention that at such temperature other transformations happen. The most evident ones are: the evaporation of eventual retained water over 100^oC; the transformation of hypothesised phase $Zn(OH)_2$ into oxide ZnO, which occurs at 300^oC in short time (10 *minutes*) [26]; the transformation of amorphous phase in crystalline.

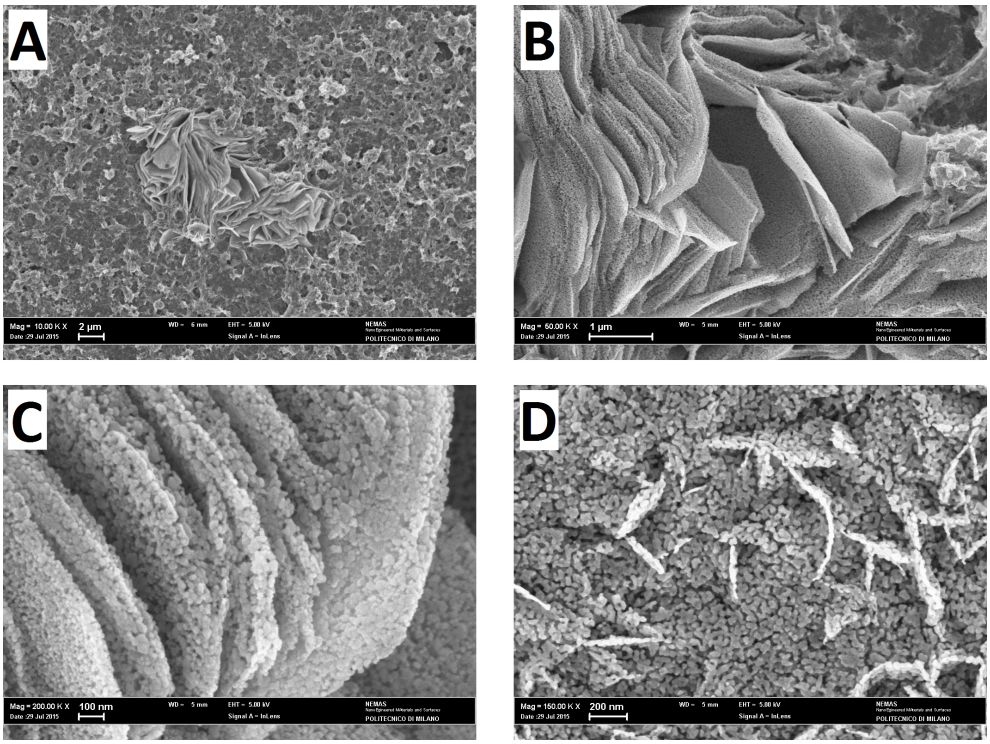

Figure 4.23: SEM images of annealed deposits of 500 μL of AZO aqueous solution. (A), (B) and (C) refer to sample ablated in 15 mL of distilled water; (D) to sample ablated in 6 mL. Both samples have fluence of $10,6\ J/cm^2$ and ablation time of 60 min.

After annealing, we can proceed with new analyses at SEM. As we can see in Figure 4.23 (A), at low magnification there is no change respect to situation before annealing: a typical layered structure in an shapeless background. Zooming in (B) of Figure 4.23, the image appears with undefined boundaries of layers, as they were out of focus. However further zooming in (C) of Figure 4.23 and also in (D), we observe a wavy aspect of structures. It is present in all visible part of annealed deposits and it makes the deposit very porous. The area-to-volume ratio, which was already high at the scale of hundreds of nanometres, is enhanced for this porosity at tens of nanometres scale. In general, it appears as if something went away, and the remaining elements pull back, leaving many voids. Moreover, the observation at SEM is easier than before annealing.

We perform EDX analyses to know if the annealing process was sufficient to remove the nitrogen (present in the form of NO_2). A spectrum is reported in Figure 4.24, whereas detected elements of the same deposit are in Table 4.2.

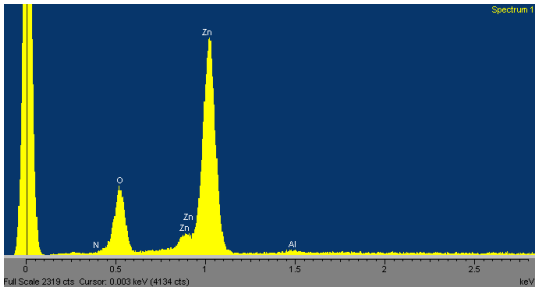

Figure 4.24: EDX spectrum of annealed deposit of 500 μL of AZO ablated in 6 mL distilled water; the fluence is $10,6\ J/cm^2$ and the ablation time is 60 min. The annealing was performed at 450^oC for 2 $hours$.

Element and electron shell	**Area 1**	**Area 2**	**Agglomerate 1**	**Area 3**	**Agglomerate 2**
C K		4,41			
N K	0,00	0,00	0,00	0,00	0,00
O K	50,41	46,74	49,51	49,88	50,76
Al K	0,00	0,66	0,00	1,02	1,07
Zn K	49,59	48,19	50,49	49,09	48,17

Table 4.2: Table of atomic percentages of elements measured via EDX in 500 μL deposit of AZO ablated in 6 mL of distilled water at fluence of $10,6\ J/cm^2$ for 60 min after an annealing at 450^oC for 2 $hours$.

We note that both prove the disappearance of nitrogen. The spectrum does not show any peak or shoulder on the left of oxygen peak; the measurement of element gives always a 0 $\%_{at}$ value for N. So we can state that nitrogen in the form of NO_2 was removed during annealing process. Also oxygen and zinc have variation in their percentage: the oxygen decreases to $47 - 51\ \%_{at}$, meantime the zinc much increases its value up to $48 - 50\ \%_{at}$. Their ratio is always near to unity, which suggests that ZnO, or more precisely AZO due to presence of aluminium, is the

main component of the film. The porosities and the voids could be left by desorption of NO_2 or H_2O, or by other compounds that were linked to ZnO.

We can proceed to Raman measurements of annealed deposits; we use the same Raman spectrometer (Ar^+ laser with wavelength $514,5\ nm$, $50x$ of magnification) in extended acquisition modality with ten measurements, every of duration of ten seconds. The set power for these measurements is 5 mW, even if the incoming power is about a third. Here the cut-off frequency is 100 cm^{-1}, so the investigation range starts from this value and continues up to 2000 cm^{-1}. We perform the analyses of many samples, all on glass substrate and after annealing at 450^oC for 2 *hours*. We encountered the same situation of Section 4.5, with above-ground white islands and dark background. When we focus the laser on white islands, we obtain spectra of crystal-like signals. Instead, when we analyse the surrounding, we detect a weaker signal or only photoluminescence. Maybe this part has a minor thickness or is still amorphous after annealing.

As in pre-annealing case, we subtract a straight line whenever photoluminescence is detected in spectrum. In order to plot the acquisition with similar characteristic in the same graph, we normalize all spectra so that they have the same height. The most relevant spectra are reported in Figures 4.25, 4.26 and 4.27, where they are grouped according to similar ablation conditions.

In general the spectra show a noise dependent on quantity deposited on substrate: less abundant deposits have more noise. However almost all peaks of wurtzitic ZnO are always present: the raise to E_2^{low}, the E_2^{high}, the $E_1(LO)$ and in the majority of cases the $A_1(TO)$ and the $E_1(TO)$. Also the secondary peaks and bands are identified: at 330 cm^{-1}, the bands at $540 - 700\ cm^{-1}$ and $980 - 1200\ cm^{-1}$, and sometimes the peak at 200 cm^{-1}. Other times also a peak due to light pollution is measured at 1122 cm^{-1}, so we will neglect it. Regarding the NO_2, its characteristic peak at *ca*. 1054 cm^{-1} is disappeared in all spectra, except in 6 mL, in 7 mL and in $8,41\ J/cm^2$, where however only small residual peaks are left. So also from Raman analyses, we can state that in almost all deposits after annealing there is not significant residual NO_2.

In all spectra prevails the E_2^{high} peak, very high in intensity and very

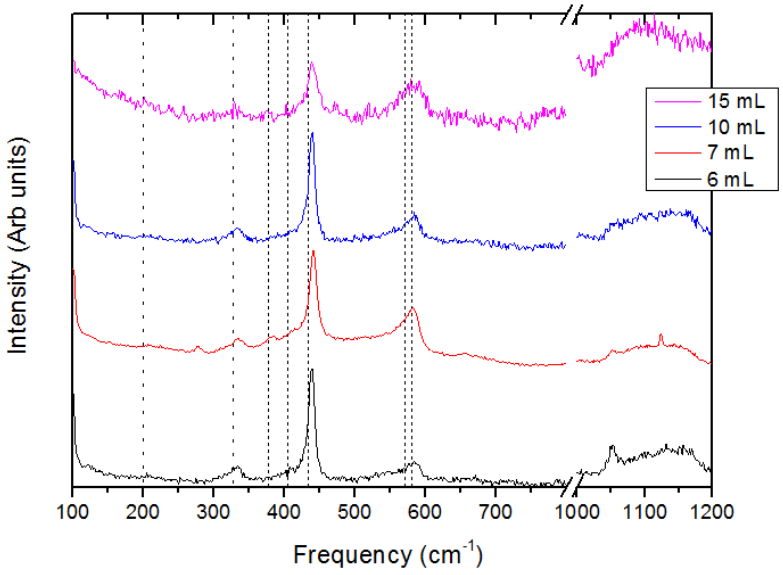

Figure 4.25: Raman spectra of deposits of AZO ablated in same conditions of fluence ($10,6\ J/cm^2$) and time ($60\ min$), and annealed at 450^oC for 2 $hours$. The spectra differ for ablation volume of distilled water: black line in 6 mL, red in 7 mL, blue in 10 mL and fuchsia in 15 mL.

sharp; it appears shifted at higher frequency respect to nominal value of 437 cm^{-1}. The peak at E_2^{low} is under the cut-off of the instrument, so we can not identify its position; we can only see its right shape: sometimes it is sharp, other times it raises as a broad band. The other very important peak to study the properties of material is the $E_1(LO)$, which is always quite high and evident. Its shape is a bit broad, due to superposition with the peak $A_1(LO)$.

In Figure 4.25 the spectra at lower ablation volume have less noise, less photoluminescence and sharper peaks; on the other hand they present a few residual NO_2. A possible explanation is a better crystallinity for deposit of samples ablated in low volume of water.

Less pronounced differences appear varying fluence (Figure 4.26), where only some modifications in intensity of peaks are evident.

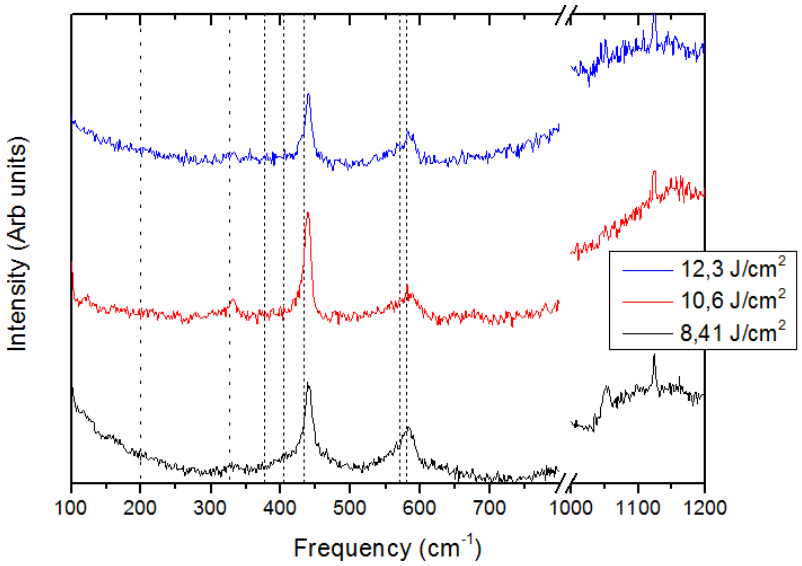

Figure 4.26: Raman spectra of deposits of AZO ablated in same conditions of distilled water volume (6 mL) and time (20 min), and annealed at 450^oC for 2 $hours$. The spectra differ for ablation fluence: black line is $8,41\ J/cm^2$, red $10,6\ J/cm^2$ and blue $12,3\ J/cm^2$.

Instead we can see a small but important variation as a function of the aging time, whose spectra are reported in Figure 4.27. Deposition of solution right after ablation leads to a spectrum with a peak at 277 cm^{-1}; it disappears if deposition happens after aging. This peak, together with others, does not correspond to first or second order modes of wurtzitic ZnO [68]. Their origin is debated: someone attributes these anomalous peaks to N doping, in particular to local vibration modes of N. Other authors support that they come from activation of inactive modes of ZnO, i.e. B_1^{low}, B_1^{high} and possible combinations, due to Disorder-Activated Raman Scattering, which can be related to doping or be present in ZnO itself. In our case probably the aluminium present in material could be the cause of the activation of these modes. Moreover also perceptible signals are present in correspondence of other anomalous modes: at *ca*. 650 cm^{-1} and at *ca*. 810 cm^{-1}. All these signals disappear after aging. Other variations between these two spectra are a change in E_2^{high}-$E_1(LO)$ peaks proportion, a total absence of NO_2 after aging and the confirmation (as seen before annealing) of an higher photoluminescence for aged deposit.

We analyse the spectra with a multi peak fitting, in order to obtain

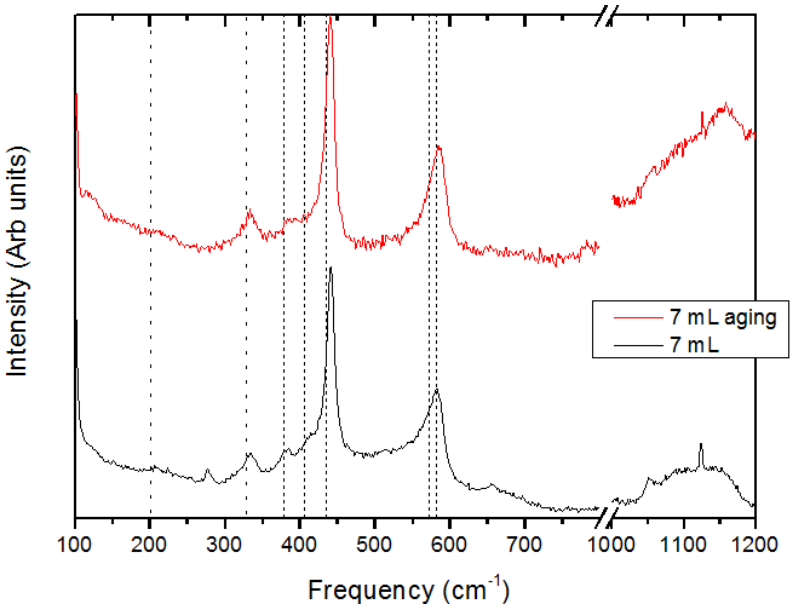

Figure 4.27: Raman spectra of deposits of same AZO sample ablated in 7 mL of distilled water volume, with $10,6\ J/cm^2$ of fluence, for 60 *min*, and annealed at 450^oC for 2 *hours*. The spectra differ for aging in liquid: the black line was deposited as ablated, the red after 5 *months* of rest in liquid.

systematic plots. Each peak is interpolated by a Lorentz peak function, as in Equation 4.6.

$$y = y_0 + \frac{2A}{\pi}\frac{w}{4(x - x_c)^2 + w^2} \tag{4.6}$$

Where x_c is the x-coordinate of the peak, i.e. the frequency in cm^{-1}, w is the Full Width at Half Maximum and A is an indication of the area subtended to the peak. In particular we are interested in the positions x_c of the peaks E_2^{high} and $E_1(LO)$, and in the areas of E_2^{high}, $A_1(LO)$ and $E_1(LO)$, so as to calculate the Area Ratio with the formula in Equation 4.7.

$$Area\ Ratio = \frac{A(A_1(LO)) + A(E_1(LO))}{A(E_2^{high})} \tag{4.7}$$

In some spectra we can not interpolate all peaks; however these three are always fitted, except in sample at 7 mL where a band-like signal between E_2^{high} and $E_1(LO)$ prevents from obtaining comparable results. This can be the second order band or can be originated by residual amorphous phase. The trends of analysed spectra are reported in Figures 4.28 and 4.29.

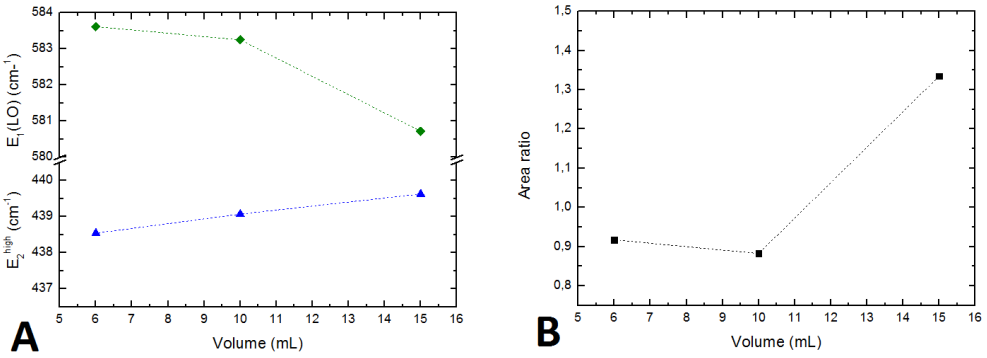

Figure 4.28: (A) The modifications of E_2^{high} and $E_1(LO)$ frequency as a function of ablation volume. (B) The area ratio, i.e. the ratio between the sum of the areas subtended to peaks $A_1(LO)$ and $E_1(LO)$ and the area of the peak E_2^{high}, as a function of ablation volume.

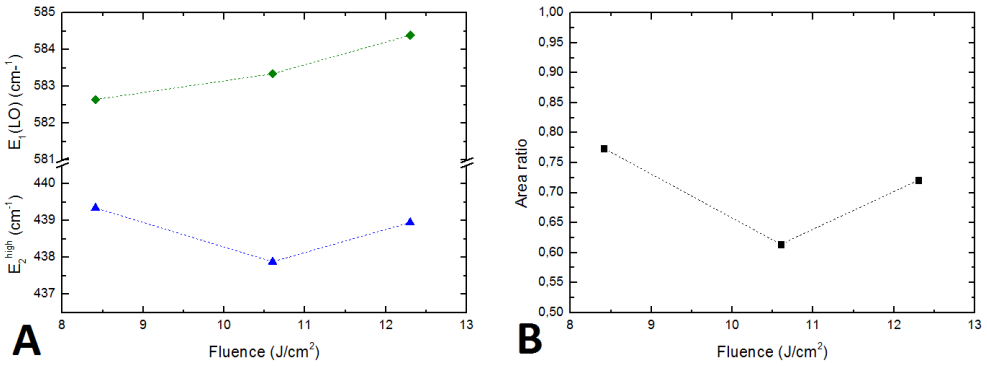

Figure 4.29: (A) The modifications of E_2^{high} and $E_1(LO)$ frequency as a function of fluence. (B) The area ratio, i.e. the ratio between the sum of the areas subtended to peaks $A_1(LO)$ and $E_1(LO)$ and the area of the peak E_2^{high}, as a function of fluence.

The peaks positions and the area ratio are influenced by crystalline order, stoichiometry, residual stresses and so on. So in principle by these quantities one can deduce many information about structure and composition. However this is not simple, and we will limit to propose some hypotheses on trends as a function of volume and fluence of ablation.

The position of E_2^{high} is always higher than nominal one (437 cm^{-1}) and it tends to distance ever more increasing volume, as we can see in Figure 4.28; the FWHM (not reported) tends to increase in the same direction, from 10 to 20 cm^{-1}. These can be the evidences of the more perfect crystallinity at low volume, as stated in Subsection 1.1.3. In effect frequency different from nominal one and large FWHM mean local disorder of the sub-lattice. In particular, the E_2^{high} mode is associated to oxygen sub-lattice, which results quite disorderly at high volumes. The Area Ratio, always above the nominal value of $0,75$, increases at higher volumes, suggesting that the cause of disorder could be the sub-stoichiometry of oxygen.

Dependencies on ablation fluence are more difficult to interpret, because they do not show evident modifications in spectra. The trend of E_2^{high} is controversial, and also the Area Ratio. Maybe the fluence is not a significant variable in the evaluated interval $8,41 - 12,3\ J/cm^2$.

We tried relating the Raman information with the morphological ones. This comparison is quite difficult because their processes involve different scales of materials and because the deposition on glass substrate is substantially different from that on silicon. On glass the material appears more concentrated in some regions, whereas on silicon the deposit is more uniform. We can make a morphological assertion from Raman measurements: there is no evidence of confinement effect in Raman, so the typical dimension of crystallites should exceed tens of nanometres, in agreement with DLS, SEM and AFM measurements.

4.7 Anti-bacterial activity

We proceed to the evaluation of antibacterial activity of samples. We are interested in a specific application: the production of textiles which prevent proliferation of bacteria. We choose as textile the silk, an expensive fibre perishable to many antibacterial treatments, and as samples two suspensions of AZO ablated in 6 mL and 7 mL of distilled water respectively, at

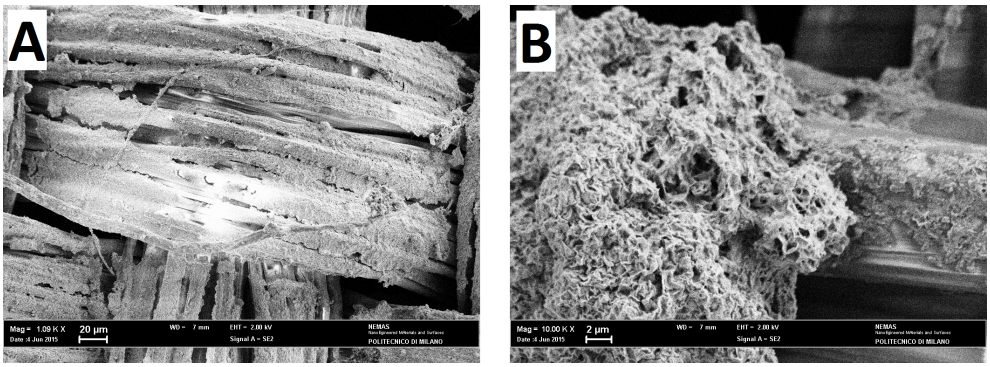

Figure 4.30: SEM images of silk strip covered by 100 μL of AZO ablated in 6 mL of distilled water at 150 mJ of energy for 60 min.

150 mJ of energy for 60 min, because they are two of the most concentrated. We deposit 100 μL of each suspension on a strip of silk and then we let them dry in air. To control if the coverage is sufficient, we see the treated silks to SEM, and they appear as in Figure 4.30.

The coverage appear well-performed and abundant; it covers almost completely silk strip. We are satisfied of coverage, so we can proceed to antibacterial analyses. They are conducted in Dipartimento di Biotecnologie e Bioscienze at Università degli Studi di Milano - Bicocca by Professor Alessandra Polissi. The antimicrobial activity of the fibres is tested according to officially approved methods of American Association of Textile Chemists and Colorists. The Viable Cell Count Method is employed for quantitative purposes, whereas the Zone of Inhibition Method is employed for qualitative purposes. The Viable Cell Count Method consists of cultures of Gram-negative *Escherichia Coli* grown in Lysogeny Broth (LB) for $16 - 18$ h at 37^oC to stationary phase. Then an aliquot is inoculated in flasks containing fresh LB and let it grow up to reach an Optical Densities measured at 600 nm ($OD600$) of $0,40$; the Colony Forming Units per millilitre is proportional to it and is equal to $ca.$ 108 CFU/mL. We prepare the final three bacterial cultures, absorbing 25 mL of this one onto the fibre specimens: the first is not-treated silk, the other two are the silks treated with our solutions. We let the cultures grow at 37^oC under agitation. At selected times (0 h, 6 h and 24 h) the corresponding specimens are quenched in aqueous $NaCl$ ($0,9$ %, 20 mL). Bacterial growth or killing rates are determined

by monitoring the CFU/mL in the presence of treated fibres compared to those obtained with untreated fibres (i.e. control). Quantitatively, the antibacterial activity of the treated fibres after a certain time t is expressed as the Percentage of Reduction of bacteria $\%R(t)$, according to the Jeong formula in Equation 4.8.

$$\%R(t) = \frac{A(t) - B(t)}{A(t)} \cdot 100 \tag{4.8}$$

Where A(t) is the CFU/mL value observed in control, and B(t) is the same in treated fibres at the same time [69]. To be considered as having significant antibacterial activity, a sample has to show reduction percentage greater than 90 %, so reducing the cells number to less than a tenth respect to not-treated one.

We report the results about the titration of bacterial cells and about the percentage reduction, both of not-treated strip and of treated ones at various times, in Figure 4.31.

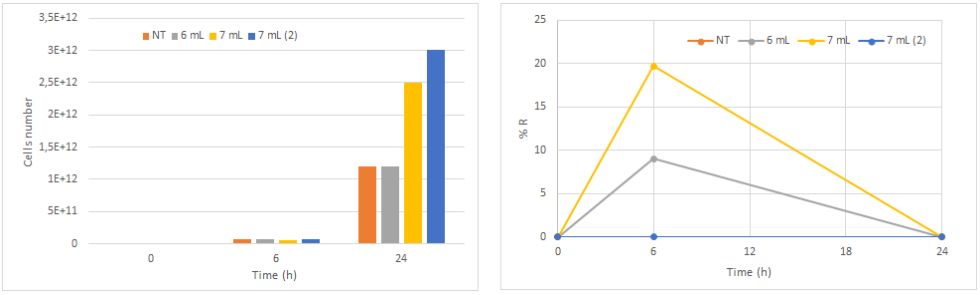

Figure 4.31: The number of bacterial cells (on the left) and the percentage reduction $\%R$ (on the right) at various times for: not-treated sample (orange), treated with 6 mL solution (grey) and treated with 7 mL solution (two tests, yellow and blue).

No sample reaches the threshold of 90 % of reduction percentage, so there is not a significant antibacterial activity in the analysed deposits. A certain reduction is shown after 6 h of culture, but probably this is only a delay in growth, because after 24 h the values are the same of not-treated sample, if not higher. So from these few preliminary tests, we can state that AZO deposited on silk is not a bactericide. We can try explaining this, hypothesizing the non-influence of substrate. A possible reason is that

usually the ZnO nanoparticles are analysed in solution and not in deposit; the deposition decreases greatly the surface area, and so the generation of H_2O_2, because it is a surface phenomenon. However some papers reported antibacterial activity in deposits too [14]. Maybe the cause is the composition of the film: the contaminants which can be present in ablated products or the aluminium could have a detrimental effect on intrinsic antibacterial properties of zinc oxide. We think that NO_2 adsorption or other hypothesized phases, such as zinc hydroxide or aqueous ZnO, could be the cause of low antibacterial activity, and not the aluminium oxide which shows itself antibacterial properties. To a better understanding, other treatments should be performed, for example annealing of deposits on high-temperature resistant substrates.

4.8 Experimental results of ablation of Titanium Dioxide and comparison with AZO

In this section we will demonstrate that PLAL technique can be applied to other oxides too; we select the Titanium Dioxide TiO_2 due to its peculiar properties which make it a suitable material for many important applications. We report the analysis performed via SEM and via Raman. We choose the conditions which maximized the production of AZO: 150 mJ of energy, 6 mL of distilled water and 60 min of ablation time. However before the experiment we noted that the laser does not reach that energy at that repetition rate. So we decrease the repetition rate at 10 Hz in order to maintain an energy at 150 mJ. The duration of experiment is still 60 min, so for the hypothesis of independence of pulses, it is equivalent to 20 min_{eq} of ablation at 30 Hz. The ablated mass results of $0,8$ mg, so a rate of $2,4$ mg/h. This is quite low in comparison of AZO, more or less a tenth. We can justify this difference asserting that the hypothesis of independence of pulses is not valid and also repetition rate has some influences in ablation rate; otherwise, it is also possible that the conditions which optimized the production rate of AZO are not equal to TiO_2 ones. So to improve this result, more tests are indispensable. At the end of ablation, the suspension of TiO_2 target, shows a greyer colour than whitish AZO suspensions. After circa a month, it starts precipitating, in the shape of a woolly sediment of a slightly sky blue colour. So we can state that TiO_2 ablation products

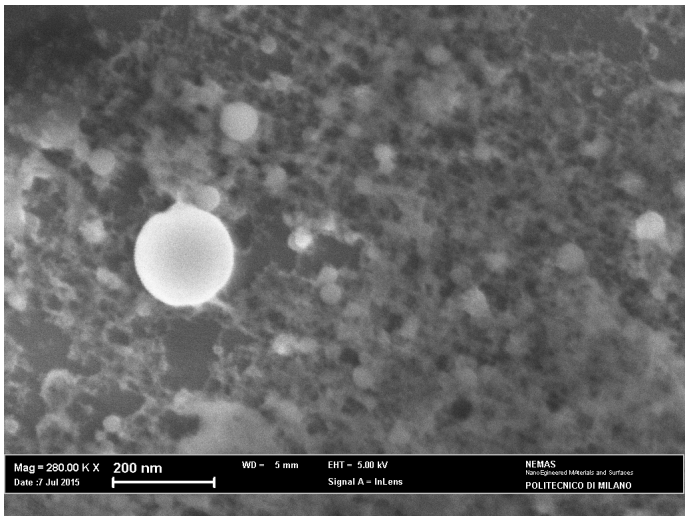

Figure 4.32: The SEM images of TiO_2 ablated in 6 mL of distilled water at energy of 150 mJ for 20 min_{eq}. The quantity deposited is 500 μL.

have a long-lasting stability than AZO ones. In order to make possible a comparison with AZO, same procedures of deposition on silicon and glass and successively of annealing are followed.

SEM morphological view of the ablation of TiO_2 target is present in Figure 4.32. The thickness of deposit is not much high, due to low ablation mass. It is composed by perfect nanospheres linked each other by an irregular reticular structure. Typical diameters of observed spheres are from 30 nm to 200 nm. Respect to AZO, the material is mainly present in the nanosphere, and not in the background.

We are interested also in the Raman spectra of the as-ablated TiO_2. They do not show the peak of O-N-O symmetric stretch, meaning that there is not adsorption of NO_2. A possible explanation is a minor bond affinity of TiO_2 with NO_2. However no typical peak of TiO_2 is detected nor bands of the underlying glass substrate. Probably the deposit it sufficiently thick to cover the signal of glass, but it should be in a complete amorphous state so that it does not emit any typical crystalline signal. The photoluminescence is quite high.

So, as we made with AZO, we proceed to annealing of TiO_2 deposit on glass, in a muffle at 450^oC for 2 h. We are able to acquire a spectrum of annealed TiO_2 deposit, in Figure 4.33.

This is completely different from spectrum before annealing, where

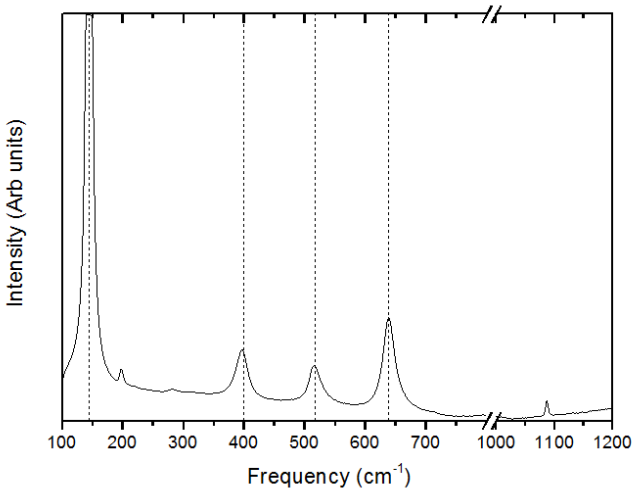

Figure 4.33: Raman spectrum of deposit of TiO_2 ablated in 6 mL of distilled water volume at fluence of $10,6\ J/cm^2$ for 20 min_{eq}, and annealed at 450^oC for 2 *hours*.

only photoluminescence with no peak was acquired. Now many peaks are present, and the noise is modest. The peaks appear very sharp, in particular that at 144 cm^{-1} which is also very intense. All these peaks correspond to the main peaks of Anatase, a tetragonal metastable phase of Titanium Dioxide. The target was in anatase too, so none structural transformation happened during ablation. We reported the reference modes of anatase as dotted lines in graph. Comparing the spectrum with the lines, we can see that all peaks are present and also well placed. A summary of the peaks is present in Table 4.3.

Mode Anatase TiO_2	**Nominal frequency [70]**	**Frequency of deposit**
E_g	144 cm^{-1}	144 cm^{-1}
B_{1g}	399 cm^{-1}	395 cm^{-1}
B_{1g}	519 cm^{-1}	516 cm^{-1}
E_g	639 cm^{-1}	639 cm^{-1}

Table 4.3: Comparison between nominal Raman peaks frequencies of TiO_2 anatase [70] and that ones of our deposit of TiO_2 ablated in 6 mL of distilled water at fluence of $10,6\ J/cm^2$ for 20 min_{eq}, and annealed at 450^oC for 2 *hours*.

Conclusions and Perspectives

We have reached our main purposes: we have been able to build an operative apparatus for ablation of a solid target in liquid, and to observe which were the main physical quantities in formation of nanostructures. This project is one of the first examples of ablation of a doped material, Aluminium doped Zinc Oxide; with some post-treatments, the elemental composition of target is kept. However we understand that we have performed only a preliminary exploration of enormous potentialities of this technique, but with our apparatus and our calibrations many other working projects could keep going.

More specifically, we obtained a high level of ablated mass, with one of the best production rates respect to other papers in literature for ZnO nanostructures and also very high respect to PLD, mainly due to enhanced plume parameters for confinement effect of liquid. We reached it optimizing many parameters involved in ablation: time, fluence of pulse and especially thickness of the liquid. To justify the increase with liquid thickness, we hypothesised that widespread recognised mechanism was modified under a certain threshold of liquid. However our under-threshold ablation carried a disadvantage: interaction of laser pulse with air and consequent incorporation of air based compounds in products.

We achieved a good way to deposit films from suspension of nanoparticles. We can tune the thickness of these films simply depositing a minor or greater amount of liquid on substrate. In particular we successfully deposited a sufficient thick film to be seen with Raman spectroscopy. Evident differences of morphology of deposits appeared depending on substrate,

so a careful choice of substrate must be performed.

Films morphology was analysed both of deposits and of nanoparticles, from the point of view of sizes and shapes. Dimensions of nanoparticles are from tens to hundreds of nanometres, as measured via Atomic Force Microscope and Scanning Electron Microscope. However we found a method to reduce it: ablation in Sodium Dodecyl Sulphate aqueous solution prevents from growth and aggregation of nanoparticles. Analysing these products, a reduction in dimensions was reported, even if it was not durable for long time, as Dynamic Light Scattering demonstrated. The shapes of deposited nanostructures were largely observed, and we understood which are their more influential factors of ablation. For example increase of ablation volume caused a change of deposits morphology from undefined background to defined structures emerging from deposit (nanoparticles and nanorods).

Also the correlation of structures with composition is reported in our work: in general the background presents an excess of oxygen, due probably to formation of hydroxides, whereas the defined structures has the same stoichiometry of target. We also succeeded to find a method to acquire Raman spectra of nanoparticles; from these we identified, after some hypotheses, the contamination of Nitrogen Dioxide. Consequently, we proceeded with annealing and new Raman analyses, which revealed the purification of film and a wurtzitic structure, with good crystallinity of most aggregated parts of deposits. We also gave an introductory sight to some Raman-related quantities, the stoichiometry and the lattice order, with identification of the most relevant and interesting tendencies in terms of ablation volume and aging.

The applications we tested did not show particular advantages in use of our synthesized nanostructures. Despite the high level of coverage, nanoparticles did not present significant antibacterial activity, maybe due to contamination of nitrogen dioxide. For the films, we evaluated their conduction after annealing, which was not satisfactory. Due to composition, we think that in microscale the structures could carry current, but in macroscale fractures and smaller cracks, formed during drying or during annealing, obstruct the electrical continuity.

Finally we demonstrated that the technique is suitable for ablation of other oxides; we ablated successfully the Titanium Dioxide, and we did a

short comparison of the products of AZO and Titanium Dioxide ablations.

Starting from PLAL technique, new possibilities are now feasible. Potential technical implementations can develop toward a system which allows the rotation of the target, in order to not ablate constantly in the same point, or toward a chamber with regulated atmosphere or some other expedients to avoid nitrogen dioxide contamination. Further, a flowing system where fresh water is injected and water with nanoparticles is extracted, could lead to a continuous production of nanoparticles in suspension. Also other types of analyses deserve to be performed, in order to completely characterize the nanostructures; for example X-Ray Diffraction to obtain the confirm of produced compounds or optical analyses. Another possibility is taking advantage of method of deposition of nanoparticles to obtain more complex films; also multilayer film can be deposited, simply performing two or more ablations with different targets.

From the applicative point of view, the nature itself of AZO target suggests electrical applications, in the field of new generation solar cells; however more efforts and studies must be performed in this direction. Additionally, other applications can be found, according to the properties of nanoparticles and of films. For example, due to shown tendency to adsorb nitrogen dioxide, our films could be optimal to act as catalyst in decomposition of nitrogen oxides and other harmful gases. Also an use as additive in polymeric material could be tested, for applications as conductive polymers or thermoelectrical materials. Lastly, more deep knowledge and comprehension of involved phenomena have to be reached.

List of Figures

List of Tables

Bibliography

[1] Ü Özgür, Ya I. Alivov, C. Liu, A. Teke, M. a. Reshchikov, S. Doan, V. Avrutin, S. J. Cho, and H. Morko. A comprehensive review of ZnO materials and devices. *Journal of Applied Physics*, 98(4):1–103, 2005.

[2] P Atkins, D Shriver, T Overton, J Rourke, F Armstrong, M Weller, and M Hagerman. *Inorganic Chemistry*. Oxford, 2009.

[3] Charles Kittel. *Introduction to Solid State Physics*. John Wiley & Sons, Inc., 2005.

[4] Subhash C. Singh and Ram Gopal. Drop shaped zinc oxide quantum dots and their self-assembly into dendritic nanostructures: Liquid assisted pulsed laser ablation and characterizations. *Applied Surface Science*, 258(7):2211–2218, January 2012.

[5] G. Zwicker and K. Jacobi. Experimental band structure of ZnO. *Solid State Communications*, 54(8):701–704, 1985.

[6] Dirk Vogel, Peter Krger, and Johannes Pollmann. Ab initio electronic-structure calculations for II-VI semiconductors using self-interaction-corrected pseudopotentials. *Physical Review B*, 52(20):316–319, 1995.

[7] John Jaffe, James Snyder, Zijing Lin, and Anthony Hess. LDA and GGA calculations for high-pressure phase transitions in ZnO and MgO. *Physical Review B*, 62(3):1660–1665, 2000.

[8] Chris G. Van De Walle. Hydrogen as a cause of doping in zinc oxide. *Physical Review Letters*, 85(5):1012–1015, 2000.

[9] V. Russo, M. Ghidelli, P. Gondoni, C. S. Casari, and A. Li Bassi. Multi-wavelength Raman scattering of nanostructured Al-doped zinc oxide. *Journal of Applied Physics*, 115(7):1–10, 2014.

[10] Jagdeep Singh, Anupama Mukherjee, Sandip K. Sengupta, Jisun Im, Gregory W. Peterson, and James E. Whitten. Sulfur dioxide and nitrogen dioxide adsorption on zinc oxide and zirconium hydroxide nanoparticles and the effect on photoluminescence. *Applied Surface Science*, 258(15):5778–5785, 2012.

[11] José a. Rodriguez, Tomas Jirsak, Sanjay Chaturvedi, and Joseph Dvorak. Chemistry of SO2 and NO2 on ZnO(0001)-Zn and ZnO powders: Changes in reactivity with surface structure and composition. *Journal of Molecular Catalysis A: Chemical*, 167(1-2):47–57, 2001.

[12] J a Rodriguez, T Jirsak, J Dvorak, S Sambasivan, and D Fischer. Reaction of NO2 with Zn and ZnO: Photoemission, XANES, and Density Functional Studies on the Formation of NO3. *Journal of Physical Chemistry B*, 104(2):319, 2000.

[13] Osamu Yamamoto. Influence of particle size on the antibacterial activity of zinc oxide. *International Journal of Inorganic Materials*, 3(7):643–646, 2001.

[14] Kalyani Ghule, Anil Vithal Ghule, Bo-Jung Chen, and Yong-Chien Ling. Preparation and characterization of ZnO nanoparticles coated paper and its antibacterial activity study. *Green Chemistry*, 8(12):1034, 2006.

[15] D. R. Sahu, Chuan Pu Liu, Ruey Chi Wang, Chien Lin Kuo, and Jow Lay Huang. Growth and application of ZnO nanostructures. *International Journal of Applied Ceramic Technology*, 10(5):814–838, 2013.

[16] Jorge L. Gomez and Onur Tigli. Zinc oxide nanostructures: From growth to application. *Journal of Materials Science*, 48(2):612–624, 2013.

[17] a. Goldenblum, A. Belu Marian, and V. Teodorescu. Optical properties of ZnO nanocrystallites embedded in a gold-oxide matrix. *Journal of Optoelectronics and Advanced Materials*, 8(6):2129–2132, 2006.

[18] Lukas Schmidt-Mende and Judith L. MacManus-Driscoll. ZnO - nanostructures, defects, and devices. *Materials Today*, 10(5):40–48, 2007.

[19] C. Agashe, O. Kluth, J. Hüpkes, U. Zastrow, B. Rech, and M. Wuttig. Efforts to improve carrier mobility in radio frequency sputtered

aluminum doped zinc oxide films. *Journal of Applied Physics*, 95(4):1911–1917, 2004.

[20] S. Venkatachalam, Y. Iida, and Yoshinori Kanno. Preparation and characterization of Al doped ZnO thin films by PLD. *Superlattices and Microstructures*, 44(1):127–135, 2008.

[21] B J Babu, S Velumani, and R Asomoza. An (ITO or AZO)/ZnO/Cu(In/Ga)Se2 superstrate thin film solar cell structure prepared by spray pyrolysis. *Photovoltaic Specialists Conference (PVSC), 2011 37th IEEE*, pages 1238–1243, 2011.

[22] P. Gondoni, M. Ghidelli, F. Di Fonzo, V. Russo, P. Bruno, J. Martí-Rujas, C. E. Bottani, A. Li Bassi, and C. S. Casari. Structural and functional properties of Al:ZnO thin films grown by Pulsed Laser Deposition at room temperature. *Thin Solid Films*, 520(14):4707–4711, May 2012.

[23] Peter P. Edwards, Adrian Porch, Martin O. Jones, David Vernon Morgan, and Richard Marc Perks. Basic materials physics of transparent conducting oxides. *Dalton Trans.*, pages 2995–3002, 2004.

[24] Gregory J. Exarhos and Xiao-Dong Zhou. Discovery-based design of transparent conducting oxide films. *Thin Solid Films*, 515(18):7025–7052, 2007.

[25] Anubha Jain, P. Sagar, and R. M. Mehra. Band gap widening and narrowing in moderately and heavily doped n-ZnO films. *Solid-State Electronics*, 50(7-8):1420–1424, 2006.

[26] Eiji Hosono, Shinobu Fujihara, Itaru Honma, and Haoshen Zhou. The fabrication of an upright-standing zinc oxide nanosheet for use in dye-sensitized solar cells. *Advanced Materials*, 17(17):2091–2094, 2005.

[27] Tadatsugu Minami. Substitution of transparent conducting oxide thin films for indium tin oxide transparent electrode applications. *Thin Solid Films*, 516(7):1314–1321, 2008.

[28] Tadatsugu Minami. Transparent conducting oxide semiconductors for transparent electrodes. *Semiconductor Science and Technology*, 20(4):S35–S44, 2005.

[29] M H Huang, S Mao, H Feick, H Yan, Y Wu, H Kind, E Weber, R Russo, and P Yang. Room-temperature ultraviolet nanowire nanolasers. *Science (New York, N.Y.)*, 292(5523):1897–1899, 2001.

[30] R. S. Ajimsha, G. Anoop, Arun Aravind, and M. K. Jayaraj. Luminescence from Surfactant-Free ZnO Quantum Dots Prepared by Laser Ablation in Liquid. *Electrochemical and Solid-State Letters*, 11(2):K14, 2008.

[31] Xilun Hu, Haibo Gong, Hongyan Xu, Haoming Wei, Bingqiang Cao, Guangqiang Liu, Haibo Zeng, and Weiping Cai. Influences of Target and Liquid Media on Morphologies and Optical Properties of ZnO Nanoparticles Prepared by Laser Ablation in Solution. *Journal of the American Ceramic Society*, 94(12):4305–4309, December 2011.

[32] Elmira Solati, Laya Dejam, and Davoud Dorranian. Effect of laser pulse energy and wavelength on the structure, morphology and optical properties of ZnO nanoparticles. *Optics & Laser Technology*, 58:26–32, June 2014.

[33] T. Jin, D. Sun, J. Y. Su, H. Zhang, and H. J. Sue. Antimicrobial efficacy of zinc oxide quantum dots against Listeria monocytogenes, Salmonella Enteritidis, and Escherichia coli O157:H7. *Journal of Food Science*, 74(1), 2009.

[34] a.I. Savchuk, A. Perrone, A. Lorusso, I.D. Stolyarchuk, O.a. Savchuk, and O.a. Shporta. ZnMnO diluted magnetic semiconductor nanoparticles: Synthesis by laser ablation in liquids, optical and magneto-optical properties. *Applied Surface Science*, 302:205–208, May 2014.

[35] Reza Zamiri, Azmi Zakaria, Hossein Abbastabar Ahangar, Majid Darroudi, Ali Khorsand Zak, and Gregor P C Drummen. Aqueous starch as a stabilizer in zinc oxide nanoparticle synthesis via laser ablation. *Journal of Alloys and Compounds*, 516:41–48, 2012.

[36] N. G. Semaltianos, S. Logothetidis, N. Hastas, W. Perrie, S. Romani, R. J. Potter, G. Dearden, K. G. Watkins, P. French, and M. Sharp. Modification of the electrical properties of PEDOT:PSS by the incorporation of ZnO nanoparticles synthesized by laser ablation. *Chemical Physics Letters*, 484(4-6):283–289, 2010.

[37] D. N. Patel, Ravi Pratap Singh, and Raj K. Thareja. Craters and nanostructures with laser ablation of metal/metal alloy in air and liquid. *Applied Surface Science*, 288:550–557, 2014.

[38] Yu S Tveryanovich, a a Manshina, and a S Tverjanovich. Production of nanodispersed materials and thin films by laser ablation techniques in liquid and in vacuum. *Russian Chemical Reviews*, 81(12):1091–1116, December 2012.

[39] Chenlin Zhao, Yi Huang, and Jeremiah T. Abiade. Ferromagnetic ZnO nanoparticles prepared by pulsed laser deposition in liquid. *Materials Letters*, 85:164–167, October 2012.

[40] Zijie Yan and Douglas B. Chrisey. Pulsed laser ablation in liquid for micro-/nanostructure generation. *Journal of Photochemistry and Photobiology C: Photochemistry Reviews*, 13(3):204–223, September 2012.

[41] Takeshi Tsuji, Yuuki Okazaki, Yasuyuki Tsuboi, and Masaharu Tsuji. Nanosecond time-resolved observations of laser ablation of silver in water. *Japanese Journal of Applied Physics, Part 1: Regular Papers and Short Notes and Review Papers*, 46(4 A):1533–1535, 2007.

[42] Takeshi Tsuji, Yasuyuki Tsuboi, Noboru Kitamura, and Masaharu Tsuji. Microsecond-resolved imaging of laser ablation at solid-liquid interface: Investigation of formation process of nano-size metal colloids. *Applied Surface Science*, 229(1-4):365–371, 2004.

[43] Koichi Sasaki and Noriharu Takada. Liquid-phase laser ablation. *Pure and Applied Chemistry*, 82(6):1317–1327, 2010.

[44] R. Fabbro, J. Fournier, P. Ballard, D. Devaux, and J. Virmont. Physical study of laser-produced plasma in confined geometry. *Journal of Applied Physics*, 68(2):775, 1990.

[45] Takeshi Sasaki, Yoshiki Shimizu, and Naoto Koshizaki. Preparation of metal oxide-based nanomaterials using nanosecond pulsed laser ablation in liquids. *Journal of Photochemistry and Photobiology A: Chemistry*, 182(3):335–341, September 2006.

[46] Haibo Zeng, Xi Wen Du, Subhash C. Singh, Sergei a. Kulinich, Shikuan Yang, Jianping He, and Weiping Cai. Nanomaterials via laser ablation/irradiation in liquid: A review. *Advanced Functional Materials*, 22(7):1333–1353, 2012.

[47] Tetsuya Shimogaki, Kota Okazaki, Kota Yamasaki, Koshi Fusazaki, Yasuaki Mizokami, Norihiro Tetsuyama, Mitsuhiro Higashihata, Hiroshi Ikenoue, Daisuke Nakamura, and Tatsuo Okada. Fabrication and characterization of spherical micro semiconductor crystals by laser ablation method. *Applied Physics A*, 117(1):269–273, May 2014.

[48] Marcus Lau and Stephan Barcikowski. Quantification of mass-specific laser energy input converted into particle properties during picosecond pulsed laser fragmentation of zinc oxide and boron carbide in liquids. *Applied Surface Science*, July 2014.

[49] Guo Bing Wang, Min Gong Fu, Bin Lu, Guo Ping Du, Li Li, Xiao Mei Qin, and Wang Zhou Shi. Growth of nanocrystalline TiO2 films by pulsed-laser-induced liquid-deposition method and preliminary applications for dye-sensitized solar cells. *Applied Physics A: Materials Science and Processing*, 100(4):1169–1176, 2010.

[50] Nadezhda M. Bulgakova, Alexei N. Panchenko, Alexei E. Tel'Minov, and Mikhail a. Shulepov. Formation of microtower structures on nanosecond laser ablation of liquid metals. *Applied Physics A: Materials Science and Processing*, 98(2):393–400, 2010.

[51] Csaba Làszlò Sajti, Ramin Sattari, Boris N Chichkov, and Stephan Barcikowski. Gram Scale Synthesis of Pure Ceramic Nanoparticles by Laser Ablation in Liquid. *J. Phys. Chem C*, 114:2421–2427, 2010.

[52] Xi Zhang, Haibo Zeng, and Weiping Cai. Laser power effect on morphology and photoluminescence of ZnO nanostructures by laser ablation in water. *Materials Letters*, 63(2):191–193, 2009.

[53] Xiu-xiu Huang and Wen-gong Zhang. Study on successively preparation of nano-TiO2 ethanol colloids by pulsed laser ablation and fluorescence property. *Applied Surface Science*, 254(11):3403–3407, March 2008.

[54] Shima Fardad and Reza Massudi. Environment effect on structure, size control and stability of Zn and ZnO nanoparticles. *2007 7th IEEE Conference on Nanotechnology (IEEE NANO)*, pages 647–650, August 2007.

[55] Hiroyuki Usui, Yoshiki Shimizu, Takeshi Sasaki, and Naoto Koshizaki. Photoluminescence of ZnO nanoparticles prepared by laser ablation in different surfactant solutions. *The journal of physical chemistry. B*, 109(1):120–4, January 2005.

[56] Zijie Yan, Ruqiang Bao, and Douglas B. Chrisey. Self-assembly of zinc hydroxide/dodecyl sulfate nanolayers into complex three-dimensional nanostructures by laser ablation in liquid. *Chemical Physics Letters*, 497(4-6):205–207, September 2010.

[57] Zijie Yan, Ruqiang Bao, Roger N. Wright, and Douglas B. Chrisey. Hollow nanoparticle generation on laser-induced cavitation bubbles via bubble interface pinning. *Applied Physics Letters*, 97(12):124106, 2010.

[58] a. Nath, S. S. Laha, and A. Khare. Effect of focusing conditions on synthesis of titanium oxide nanoparticles via laser ablation in titanium-water interface. *Applied Surface Science*, 257(7):3118–3122, 2011.

[59] Yoshie Ishikawa, Yoshiki Shimizu, Takeshi Sasaki, and Naoto Koshizaki. Preparation of zinc oxide nanorods using pulsed laser ablation in water media at high temperature. *Journal of colloid and interface science*, 300(2):612–5, August 2006.

[60] Haibo Zeng, Peisheng Liu, Weiping Cai, Xueli Cao, and Shikuan Yang. Aging-Induced Self-Assembly of Zn/ZnO Treelike Nanostructures from Nanoparticles and Enhanced Visible Emission. *Crystal Growth & Design*, 2007.

[61] Haibo Zeng, Weiping Cai, Yue Li, Jinlian Hu, and Peisheng Liu. Composition/structural evolution and optical properties of ZnO/Zn nanoparticles by laser ablation in liquid media. *The journal of physical chemistry. B*, 109(39):18260–6, October 2005.

[62] S. Zhu, Y. F. Lu, M. H. Hong, and X. Y. Chen. Laser ablation of solid substrates in water and ambient air. *Journal of Applied Physics*, 89(4):2400–2403, 2001.

[63] Wei Guo and Bing Liu. Liquid-phase pulsed laser ablation and electrophoretic deposition for chalcopyrite thin-film solar cell application. *ACS applied materials & interfaces*, 4(12):7036–42, 2012.

[64] Zijie Yan, Ruqiang Bao, Yong Huang, and Douglas B. Chrisey. Hollow particles formed on laser-induced bubbles by excimer laser ablation of Al in liquid. *Journal of Physical Chemistry C*, 114(26):11370–11374, 2010.

[65] K. Y. Niu, J. Yang, S. a. Kulinich, J. Sun, and X. W. Du. Hollow nanoparticles of metal oxides and sulfides: Fast preparation via laser ablation in liquid. *Langmuir*, 26(22):16652–16657, 2010.

[66] Carlos Vargas Hernández and Rubén Antonio Vargas. Preparation of Zinc Oxide and Poly-Ethylene Oxide Composite Membranes and Their Phase Relationship Composito De Oxido De Zinc Y Poly-Ethylene. *Dyna*, 174:79–85, 2012.

[67] Teppei Nishi, Noritomo Suzuki, Naoko Takahashi, and Kazuhisa Yano. Preparation of monodispersed Pd nanoparticles by laser ablation at air-suspension interface. *Journal of Nanoparticle Research*, 15(4), 2013.

[68] F. J. Manjón, B. Marí, J. Serrano, and a. H. Romero. Silent Raman modes in zinc oxide and related nitrides. *Journal of Applied Physics*, 97(5), 2005.

[69] H. J. Lee, S. Y. Yeo, and S. H. Jeong. Antibacterial effect of nanosized silver colloidal solution on textile fabrics. *Journal of Materials Science*, 38(10):2199–2204, 2003.

[70] U Balachandran and N G Eror. Raman spectra of titanium dioxide. *Journal of Solid State Chemistry*, 42(3):276–282, 1982.